

秋田県立大学大学院博士学位論文

**Preparation of Biocarbon Derived from Sugarcane Bagasse and Its Composites
for Application in Supercapacitors**

(サトウキビバガス由来のバイオカーボンとその複合材料の創製およびスーパーキャパシタへの応用)

陳 姣

2018年3月

Abstract

Supercapacitors, as one of the most promising energy storage devices, due to their good energy density, superior power density, fast charge/discharge rate, and long cycle life, which make it exhibit promising applications in portable devices, renewable energy and transportation. Based on the different charge storage mechanisms, supercapacitors can generally be divided into two types: the electrical double-layer capacitors (EDLC) and the pseudocapacitors. Carbon materials, such as active carbon, graphene and carbon nanotube are usually used in EDLC electrode, but their low energy density, limited their further application, as well as most of methods to prepare of the above carbon materials often requires complicated preparation conditions or special facilities, leading to the high cost. In the present work, first, low cost and uncomplicated method of allium-giganteum-like biocarbon (KWB) were derived from sugarcane bagasse, and then different kinds of carbon-based composite materials including manganese dioxide (MnO_2)/KWB, polyaniline (PANI)/KWB and iron oxide (Fe_3O_4)/KWB were obtained. All of the above materials were used as electrode material of supercapacitors, and morphology, chemical composition and electrochemical performance were investigated. Besides, due to the unique structure of KWB, all the composites show the superior performance in supercapacitors.

In Chapter 1, the research backgrounds, research significance, research purpose and the construction of this thesis are particularly described.

In Chapter 2, the properties of experimental materials used in this thesis are presented. The experimental methods and characterizations are also particularly described in this chapter.

In chapter 3, KWB were derived from sugarcane bagasse via one-step carbonization and activation method. The results show that, both the mass ratio of potassium hydroxide (KOH) to sugarcane bagasse and the temperature of carbonization could impact on the morphology and chemical composition of KWB, thereby further affect

the electrochemical performance of KWB. Under the optimum conditions, the SEM of KWB shows the excellent 3D hierarchical porous network structure with allium-giganteum-like, which also has the best specific surface area. Its promise the excellent electrochemical performance when used as electrode materials for supercapacitors. What's more, KWB also could be carbon-base to prepare other composites in the further research.

In chapter 4, MnO_2/KWB (KWBM) composites have been prepared by a simple method. The MnO_2 nanosheets anchored on the surface of biocarbon and obtained the KWBM, and KWB was used as both scaffolds and reducing agents for MnO_2 growth. The analysis results demonstrated that chemical composition and microstructure of KWBM were closely related to the mass ratio of KMnO_4/KWB , and which further impacted electrochemical performance of KWBM profoundly. Especially, the KWBM-4 exhibited a higher specific capacitance of 402 F g^{-1} at a current density of 1 A g^{-1} in three-electrode system. The asymmetric two-electrode system with outstanding energy density was assembled by employing the KWBM-4 as the positive electrode and the KWB as the negative electrode. The two-electrode system displays a high energy density of 25.9 Wh kg^{-1} at a power density of 750 W kg^{-1} within a potential range of 0-1.5 V. Furthermore, the system exhibited high cycle stability with only 5.8 % loss of its initial capacitance after 2000 cycles.

In chapter 5, a coral-like polyaniline/KWB (PANI/KWB) composites was prepared via in-site polymerization method. The PANI/KWB composites were obtained using KWB as the scaffolds for PANI growth and [CMMIm]Cl ionic liquid as dopant. The different mass ratio of aniline monomer (An) and KWB be researched. The results indicated that chemical composition and microstructure of PANI/KWB were closely related to the mass ratio of aniline monomer (An) and KWB, and which further impacted electrochemical performance of PANI/KWB profoundly. Especially, the PANI/KWB-4 exhibited a highest specific capacitance of 447 F g^{-1} at a current density of 0.5 A g^{-1} . Furthermore, the asymmetric two-electrode system based on PANI/KWB-4 as positive electrode and KWB as negative electrode is successfully assembled with a voltage window of 0~1.6 V, exhibiting high energy density (27.3 Wh kg^{-1}) and power

density (800 W kg^{-1}), and excellent cycling stability (87% capacitance retention after 2000 cycles).

In chapter 6, $\text{Fe}_3\text{O}_4/\text{KWB}$ nanocomposites (KBF_e) have been prepared via a chemical coprecipitation method under different mass ratio of Fe_3O_4 to KWB. As a result, the chemical composition and microstructure of the KBF_e were intimately related to the mass ratio of Fe_3O_4 and KWB, which impacted the electrochemical performance of the KBF_e profoundly. Especially, the KBF_e-4 displayed the highest specific capacitance of 342 F g^{-1} at a current density of 1 A g^{-1} . Furthermore, the asymmetric two-electrode system based on KWBM composite as positive electrode and KBF_e-4 as negative electrode was successfully assembled with a voltage window of 0~1.6 V, and exhibited high energy density (29.1 Wh kg^{-1}) and power density (800 W kg^{-1}), along with excellent cycling stability (89.5% capacitance retention after 1000 cycles).

In chapter 7, general conclusions of the study are made.

Content

Abstract.....	I
Content.....	IV
Chapter 1 Introduction.....	1
1.1 Background.....	1
1.2 Supercapacitors.....	2
1.2.1 The storage energy principle of EDLCs.....	2
1.2.2 The storage energy principle of pseudocapacitors.....	6
1.3 The electrode materials of supercapacitors.....	7
1.3.1 Carbon-based electrode materials.....	7
1.3.2 Transition metal oxides-based electrode materials.....	18
1.3.3 Conducting polymer-based electrode materials.....	14
1.4 Contribution from this dissertation.....	22
References.....	26
Chapter 2 Materials, experimental and characterizations.....	37
2.1 Materials.....	37
2.1.1 Chemical reagents.....	37
2.1.2 Materials of electrochemical test.....	40
2.2 Experimental methods.....	40
2.2.1 Preparation of KOH-activated biomass carbon (KWB) derived from sugarcane bagasse.....	40
2.2.2 Preparation of MnO ₂ /KWB composites (KWBM).....	41
2.2.3 Synthesis of 1-methyl-3-alkylcarboxylic acid imidazolium chloride.....	

([CMMIm]Cl) ionic liquid	41
2.2.4 Synthesis of pure PANI without IL	41
2.2.5 Preparation of polyaniline/biomass carbon composites (PANI/KWB)	42
2.2.6 Preparation of Fe ₃ O ₄ /KWB composites (KBF _e)	42
2.3 Characterization	43
2.3.1 Morphological, structure, thermal and component characterizations	43
2.3.2 Electrochemical performance characterization	44
References	46
Chapter 3 Biocarbon from sugarcane bagasse with superior performance in supercapacitors	48
3.1 Introduction.....	48
3.2 Experimental.....	50
3.2.1 Materials.....	50
3.2.2 Preparation of KOH-activated biocarbon (KWB) derived from sugarcane bagasse	50
3.2.3 Structure characterization.....	51
3.2.4 Electrochemical testing	51
3.3 Results and discussion	52
3.3.1 Microstructural characterization.....	52
3.3.2 Electrochemical performance of KWB samples	60
3.4 Conclusions.....	64
Reference.....	66
Chapter 4 Manganese dioxide/ biocarbon composites with superior performance in supercapacitors	72
4.1 Introduction.....	72
4.2 Experimental.....	74

4.2.1	Materials.....	74
4.2.2	Preparation of KOH-activated biocarbon (KWB) derived from sugarcane bagasse.....	74
4.2.3	Preparation of MnO ₂ /KWB composites (KWBM)	74
4.2.4	Structure characterization.....	75
4.2.5	Electrochemical test	75
4.3	Results and discussion	76
4.3.1	Microstructural characterization.....	76
4.3.2	Electrochemical performance of KWBM composites	84
4.4	Conclusions.....	92
	Reference.....	94

Chapter 5 Polyaniline/sugarcane bagasse derived biocarbon composites with superior performance in supercapacitors.....100

5.1	Introduction.....	100
5.2	Experimental.....	101
5.2.1	Materials.....	101
5.2.2	Synthesis of 1-methyl-3-alkylcarboxylic acid imidazolium chloride ([CMMIm]Cl) ionic liquid.....	102
5.2.3	Preparation of KOH-activated biocarbon (KWB) derived from sugarcane bagasse.....	102
5.2.4	Preparation of polyaniline/ activated biocarbon composites (PANI/KWB)	102
5.2.5	Synthesis of pure PANI without IL	103
5.2.6	Structure characterization.....	103
5.2.7	Electrochemical test	104
5.3	Results and discussion	105
5.3.1	Microstructural characterization.....	105

5.3.2 Electrochemical performance of PANI/KWB composites	113
5.4 Conclusions.....	120
Reference.....	121
Chapter 6 Fe₃O₄ / biocarbon composites with superior performance in supercapacitors	128
6.1 Introduction.....	128
6.2 Experimental.....	130
6.2.1 Materials	130
6.2.2 Preparation of KOH-activated biocarbon (KWB) derived from sugarcane bagasse	130
6.2.3 Preparation of Fe ₃ O ₄ /KWB composites (KBF _e)	130
6.2.4 Preparation of pure Fe ₃ O ₄	131
6.2.5 Preparation of MnO ₂ /KWB composites (KWBM)	131
6.2.6 Structure characterization.....	132
6.2.7 Electrochemical testing	132
6.3 Results and discussion	133
6.3.1 Microstructural characterization.....	133
6.3.2 Electrochemical performance of KBF _e composites.....	142
6.4 Conclusions.....	150
Reference.....	151
Chapter 7 Conclusions.....	157
Publication.....	160
Acknowledgements	162

Chapter 1 Introduction

1.1 Background

Since the beginning of the 21st century, the rapid development of the global economy and the explosive growth of the population have led to an increasing demand for energy. However, the non-renewable fossil fuels, which are the main energy sources, not only have the problem of insufficient stock supply, but also the greenhouse effect brought by the subsequent product carbon dioxide (CO₂) is threatening the human living environment, such as greenhouse gas emissions, air pollution and water pollution. For the future, health and sustainable development of our society's ecosystem, energy have become the most important issue affecting human survival and development. Therefore, all global organizations agree that energy is the main challenge of this century that our habitat must overcome.

Nowadays, developing clean energy sources and their associated technologies are considered a practical way to solve this problem. Therefore, many researchers focus on the renewable energies, for instance, wind [1], seawater [2], geothermal [3], solar [4] [5], biomass [6, 7], and so on. However, most renewable clean energy sources are highly dependent on the time of day and regional weather conditions. For example, the solar cell can produce sufficient and improved efficiency during the daytime, but energy also needs to be stored during daytime for using at night. Development of related energy conversion and energy storage devices is therefore required to effectively harvest these intermittent energy sources. About this matter, electrochemical supercapacitors (ESs) are recognized as one of the most promising electrochemical energy storage/conversion devices, and have been widely applied in consumer electronics, transport, telecommunications, medicine, back-up memory systems and other sectors [8].

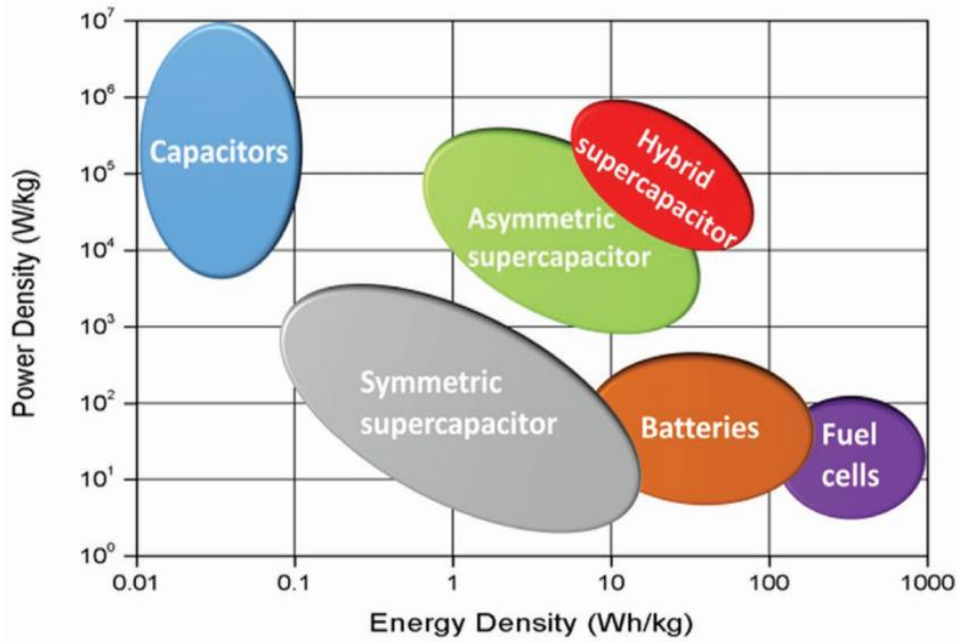


Fig. 1.1 Specific energy and power capabilities of capacitors (electrostatic), electrochemical capacitors (supercapacitors), batteries and fuel cells [9].

1.2 Supercapacitors

Supercapacitors, also are named as ultracapacitors or electrochemical capacitors. Supercapacitors with high power density ($> 10 \text{ kW kg}^{-1}$), super-long cycle life, rapid charge/discharge rate, simple principle and small environment impact hold a great promise in the field of electrical energy storage [10-13]. Generally, due to the different of energy storage principle mechanism, supercapacitors can be divided into two categories: one is based on electrostatic interactions, known as electrical double layers capacitors (EDLCs) and the other involves chemical reactions which named pseudocapacitor [12,14]. In order to distinguish, we explain the two energy storage mechanism will be described separately, though they usually function together in a supercapacitor. Especially in recent years, a new type supercapacitors have been developed, hybrid capacitors, which refer to ones employing both the electrical double-layer (EDL) and pseudocapacitive mechanisms to store charges. With the rapid developments of this area in decade, some new battery-type hybrid devices have been developed, for example lithium ion capacitor and carbon//PbO₂ [8]. These devices are

regarded as hybrid ESs ascribing they have one EDL or pseudocapacitive electrode combined with the other rechargeable battery-type electrode. Based on the difference between the electrode material and the electrode combination, the hybrid ESs reviewed include: (a) those based on composites electrodes made from both EDL capacitive materials and pseudocapacitive materials [15]; (b) those of asymmetric design with one EDL electrode and the other pseudocapacitive or battery-type electrode [16]; as well as, (c) those of the asymmetric structure with one pseudocapacitive electrode and the other rechargeable battery-type electrode [17]. These new hybrid capacitors have been demonstrated to be capable of delivering higher energy density and power density, as well as a broader range of applications [18, 19].

Table 1.1 Summary of the different types of supercapacitor devices [20].

Type of supercapacitor		Electrode material	Charge storage mechanism	Merits/shortcomings
Electrochemical double layer capacitor (EDLC)		Carbon	Electrochemical double layer (EDL), non-Faradaic process	Good cycling stability, good rate capability, low specific capacitance, low energy density
Pseudocapacitor		Redox metal oxide or redox polymer	Redox reaction, Faradaic process	High specific capacitance, relatively high energy density, relatively high power density, relatively low rate capability
Hybrid capacitor	Asymmetric hybrid	Anode: pseudocapacitance materials, cathode: carbon	Anode: redox reaction, cathode: EDL	High energy density, high power density and good cyclability
	Symmetric composite hybrid	Redox metal oxide/carbon or redox polymer/carbon	Redox reaction plus EDL	High energy density, moderate cost and moderate stability
	Battery-like hybrid	Anode: Li-insertion material, cathode: carbon	Anode: Lithiation/delithiation cathode: EDL	High energy density, high cost and requires electrode material capacity match

1.2.1 The storage energy principle of EDLCs

The main energy storage mechanism of EDLCs in supercapacitor arises from the reversible electrostatic accumulation of ions on the surface of the porous carbon. EDLCs have the ability to rapid storage and release of energy and storing much energy due to the large interfacial area and the atomic range of charge separation distances [13]. The construct of the double layer has been studied by Helmholtz whose first developed and modelled the double layer concept in investigations on colloidal suspensions in the 19th century [21]. As illustrated in Fig. 1.2a, the Helmholtz model give a description of the charge separation at the electrode/electrolyte interface when an electrode of surface

area is polarized [13, 22]. Because the Helmholtz model does not consider the diffusion of ions in the solution and the interaction between the dipole moment of the solvent and the electrode, for this, Gouy and Chapman put forward a diffuse model of the EDL in which the potential decreases exponentially from the electrode surface to the fluid bulk (Fig. 1.2b) [23, 24]. However, the Gouy-Chapman model is deficient for highly charged double-layers, and in 1924, Stern [25] combined the Helmholtz and Gouy-Chapman models by accounting for the hydrodynamic motion of the ionic species in the diffuse layer and the accumulation of ions close to the electrode surface (Fig. 1.2c). These two layers are equivalent to two capacitors in series, CH (Helmholtz layer) and CD (diffuse layer), and the total capacitance of the electrode (CDL) is given by Equation (1.1):

$$\frac{1}{C_{DL}} = \frac{1}{C_H} + \frac{1}{C_D} \quad (\text{Eq. 1.1})$$

where CH and CD are the capacitance of compact double layer and diffusion region, respectively.

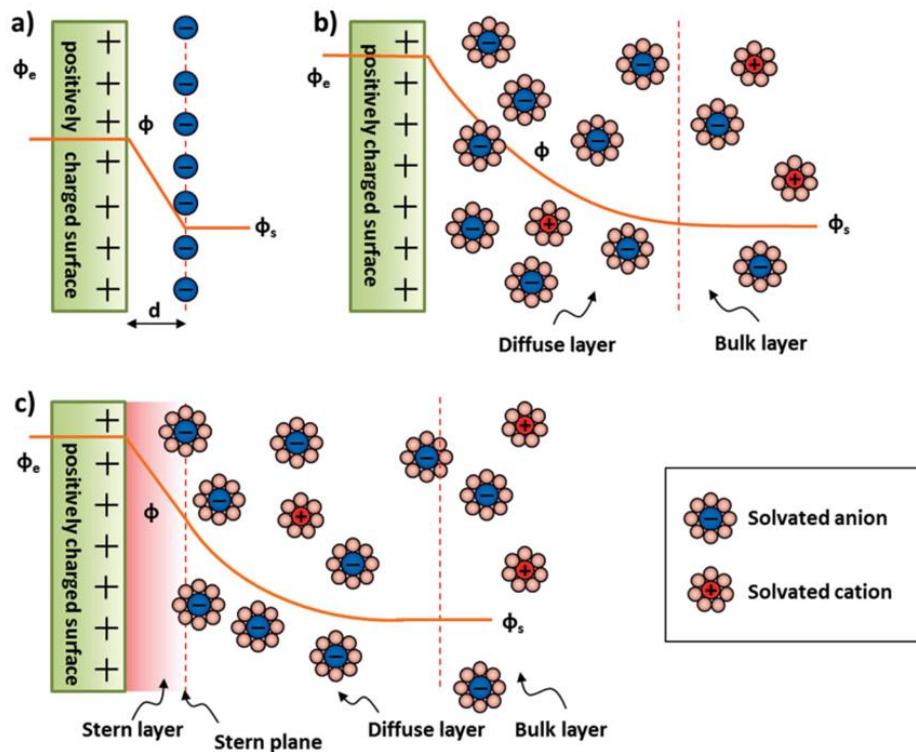


Fig. 1.2 (a) Helmholtz model, (b) the Gouy-Chapman model, and (c) the Stern model of the electrical double-layer formed at a positively charged electrode in an aqueous

electrolyte [22].

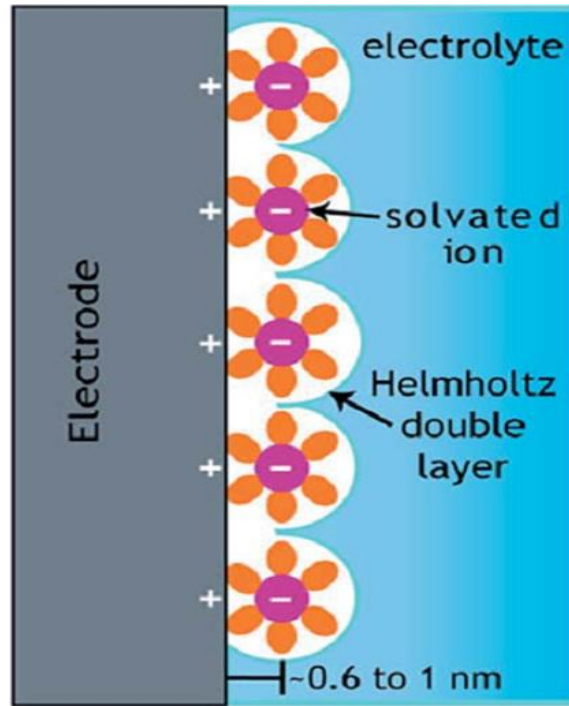


Fig. 1.3 Representation of EDLC in its charged state [28].

An EDLCs consists of two electrodes, generally, the material of the electrode is active carbon (AC). The material of the electrode is direct contact with the current collector, and the electrode separated by a porous film impregnated with an electrolyte solution (as shown in Fig. 1.3). When an electric potential difference is applied between the electrodes, the negative charge carriers, electrons, in the negatively polarized electrode are balanced by an equal number of positive cations at the electrode/electrolyte interface, while at the positively polarized electrode are electrically balanced by anions [22, 26, 27]. Therefore, the total capacitance can be controlled by the electrode with the smallest value according to the equation Eq. 1.2:

$$\frac{1}{C} = \frac{1}{C_1} + \frac{1}{C_2} \quad (\text{Eq. 1.2})$$

where C , C^+ and C^- are the capacitance of the whole supercapacitors, the positive electrode and the negative electrode, respectively. In case of a symmetric system, both electrodes employ by the equal in materials, mass and size, the Eq. 1.3 can be simplified to Eq. 1.3 [18]:

$$C_{sp} = 4 \cdot \frac{C}{m_{AM}} \quad (\text{Eq. 1.3})$$

where C_E and m_{AM} are the capacitance of electrode and the total mass of active materials.

1.2.2 The storage energy principle of pseudocapacitors

Pseudocapacitors, also be named faradaic supercapacitor due to the energy storage formed via faradaic charge-storage phenomenon. Different from the purely electrostatic phenomena of EDLCs, pseudocapacitors have a chemically reactive environment between the electrode material, and the electrolyte, charge transfers are involved between them at the interface, that is, faradaic interactions take place. These charge transfers provoke chemical changes (oxidation-state change) in the electrode materials, and thus, charges are stored chemically at some oxidation states.

During discharge, this chemical reaction takes place in reverse, and the electrode materials are restored to the previous oxidation states and the stored charges are released [14, 20, 29] (as shown in Fig. 1.4). The chemical reactions are not completely reversible ever for the best effort reversible combination of electrode and electrolyte. Hence, even after complete discharge, pseudocapacitors are always had some residual electrode materials cannot take part in the reversible chemical reaction process [14]. This phenomenon issue in the loss of active materials, which further reduces the value of the maximum specific capacitance with increasing the cycle numbers, thus the cycle stability of the pseudocapacitors also reduces.

Furthermore, pseudocapacitors have the highest charge-transfer rate at a special potential. But sometime pseudocapacitors have instantaneous electrostatic responses on account of the delayed response of pseudocapacitors relative to EDLCs, which need a delay to overcome this potential barrier [14, 29]. Although, pseudocapacitors have the dispute of cycle stability and response-time, they are still aroused researcher's interesting owing to their high ability of storage energy based on the chemical reaction. Hence, overcome the above mentioned problems have been the topic of scientific investigation in recent years.

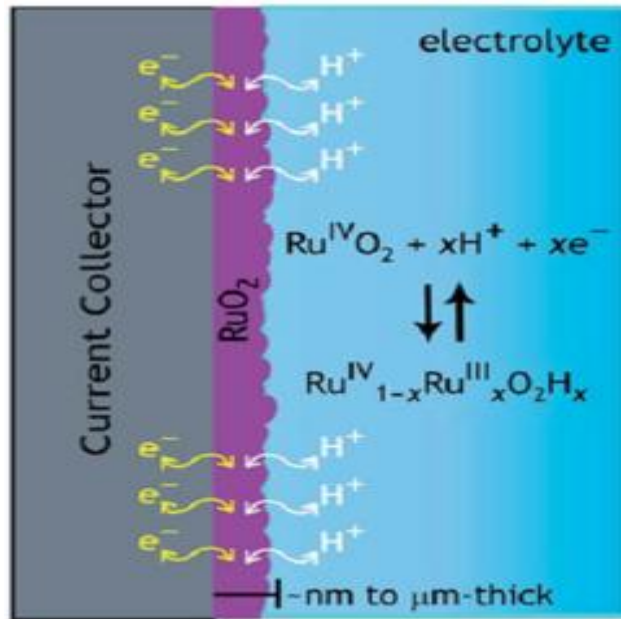


Fig. 1.4 Redox reaction based pseudocapacitance [28].

1.3 The electrode materials of supercapacitors

A typical supercapacitor contains four components: current collector, separators, electrolyte, and electrode. Electrode material is one of the core components, which directly determines the capacitance, delivery rate and efficiency of a supercapacitor.

1.3.1 Carbon-based electrode materials

The 21st century has predominantly become the carbon age, as carbon (graphite, hard carbon, glassy carbon, carbon black, as shown in Fig. 1.5) have previously been utilized in almost all new energy devices, including supercapacitors, Li-ion batteries, ultracapacitors, and hydrogen-storage devices [9]. Due to the sp^2 -hybridized solid carbon and the enormous adaptability to different interface processes of carbon element, carbon-based materials are the most prospective candidates for the supercapacitor negative electrode material arises from the unique chemical and physical properties, such as low cost, abundance, nontoxicity, and environmentally friendly nature, processability and compatibility in composite materials, as well as high electronic conductivity and outstanding temperature stability [27, 30]. Carbon materials generally

work as EDLCs, wherefore the high surface area range (1 to $> 2000 \text{ m}^2\text{g}^{-1}$) and conductivity are critical factors for them as the supercapacitors electrodes. Furthermore, the surface area of carbon materials will be deeply impacted by the porous structures. Thus, a tunable porous structure and carbon surface chemistry, as well as large surface area and high electrical conductivity are desired attributes in tailoring electrode properties to achieve optimum performance.

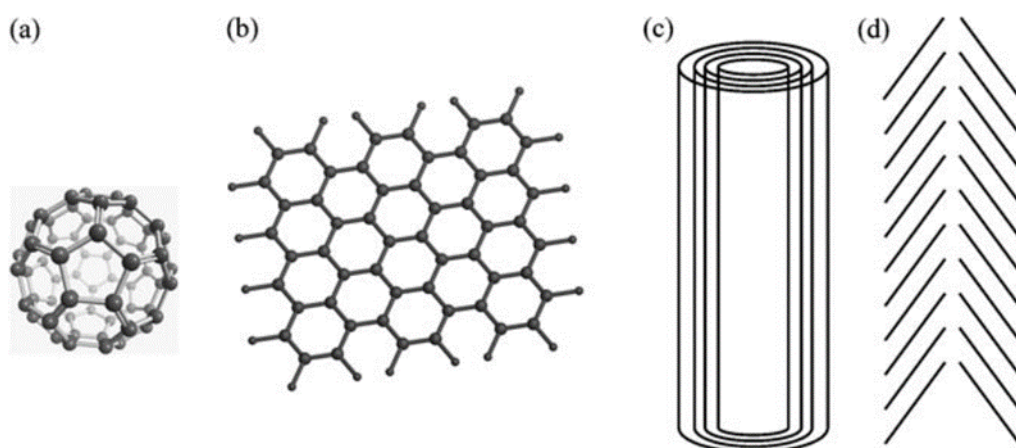


Fig. 1.5 Schematic illustrations of several important carbon nanostructures, (a) fullerene, (b) graphene, (c) carbon nanotube, and (d) carbon nanofiber [30].

1) Activated carbon (AC)

Among the various carbon-based materials, activated carbon (AC) has been the first choice from research and commercial perspectives over the last 40 years due to their merits of low cost, large theoretical surface area ($\approx 3000 \text{ m}^2 \text{ g}^{-1}$) and a broad pore-size tenability [9, 13, 31]. In general, AC is produced from physical (thermal) and/or chemical activation of various types of carbonaceous source materials, such as polymer (dopamine [32], polypyrrole [33], protein [34]), chemical reagent (zeolitic imidazolate [35]), biomass (sugarcane bagasse [36], pine cones [37], bamboo [38], waste coffee [31]), and etc. Depending on the activation methods as well as the carbon precursors used, AC possessing various physicochemical properties with well-developed surface areas as high as $3000 \text{ m}^2\text{g}^{-1}$ have been produced, good electrochemical properties have

been studied, as well as the porous structure could be designed [39-41]. The International Union of Pure and Applied Chemistry (IUPAC) defines porous according to their size as follows [42]:

- Macropores: larger than 50 nm
- Mesopores: between 2 and 50 nm
- Micropores: smaller than 2 nm

On account of the capacitive mechanism for AC is mainly physical adsorption/desorption. Therefore, the very important factor is the porous structure (as shown in Fig. 1.6). In other words, the capacity of AC depends on several mutually interlinked parameters, that is, total specific surface area, normally referred to as the Brunauer–Emmet–Teller (BET) surface area; the nature of the porosity of the electrode; the pore size distribution; and the conductivity of the electrode material [14, 43]. The porous structure of AC can be controlled through different experimental conditions, such as the carbonization temperature in physical activation, and the dosage of activating agents in chemical activation, while to obtain the perfect porous structure for electrode [27]. Someone successful prepared the AC with the specific surface area reach up to $3000 \text{ m}^2\text{g}^{-1}$, but the corresponding specific capacitance $< 10 \text{ } \mu\text{F cm}^{-2}$, much smaller than the theoretical value ($15\text{-}25 \text{ } \mu\text{F cm}^{-2}$), that means not all pores are benefited for charge accumulation [13]. Actually, a large portion of the micropores remains inaccessible to the electrolyte because of the incompatible pore size with electrolyte ions, which significantly drops the usable surface area and the specific capacitance [44].

In recent year, some researches show that a maximum EDLC could be observed in AC with pores of the size similar to that of electrolyte ions, while pores whose size is largely deviated from ion size can result in significant loss of the capacitance [45, 46]. Hence, it is imperative to control the pore-size distribution in ACs to maximize the energy/power density. Hierarchically porous AC with 3D network framework has been developed for high rate electrochemical capacitive energy storage [47-49]. This kind of 3D AC is characterized by porous of all different dimensions, including micropores, mesopores and macropores. What's more, through research people have found that pores with different pore sizes have different effect. Micropores contribute mostly to

the specific surface area and accessible to hydrated ions [50, 51]; mesopores can allow the rapid transport of ions from the electrolyte to the entire surface of the electrodes and make them quickly available for electric charge exchange [30]; macropores and localized graphitic structure can serve as ion-buffering reservoirs and enhances the electrical conductivity, respectively [30]. Especially, the macro and mesopores are a prerequisite for the transport of the electrolyte to the micropores in many ACs (as shown in Fig. 1.7) [30, 52, 53].

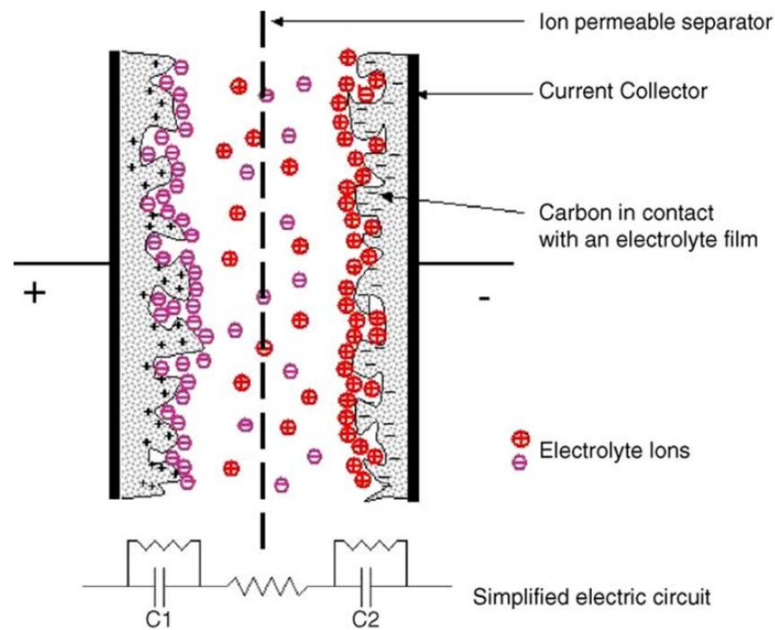


Fig. 1.6 Representation of charged state of a symmetric EDLCs using porous material and of the corresponding equivalent circuit [27].

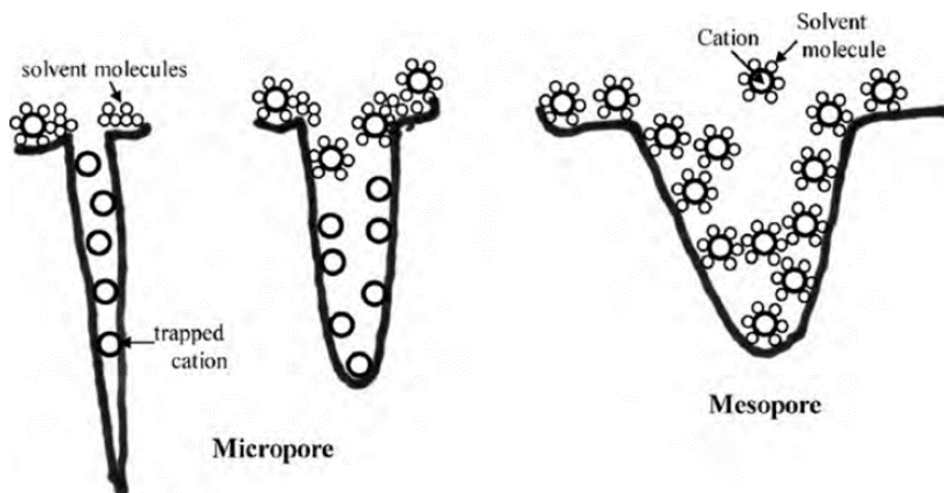


Fig. 1.7 Schema for adsorption of electrolyte ions with or without solvation to the surface of pores with different sizes [53].

However, it remains limited to obtain the maximum capacitance of EDLCs through control the surface area and pore size of the AC, as well as high energy density supercapacitors, require more excellent electrochemical performance of AC electrode materials. An effective means of improving electrochemical performance of AC material has been proved, that is introduced pseudocapacitive phenomena at the electrode and electrolyte interface via substituting some atoms in AC by heteroatoms (such as N [49], O [54], P [55], B [56]). Nevertheless, we note that the electronic properties of AC depend strongly on size and chirality, so the properties cannot be easily tailored [57, 58]. B or N usually be choice to doping in AC, due to B and N are the nearest neighbors of the C in the periodic table and atomic radius of B and N are similar to C [59, 60]. Also, Co-doped with two heteroatoms are also used, and this is a benefit for their application in electronic devices [56, 57, 61].

2) Carbon nanotubes (CNTs)

Despite the great use of AC materials as supercapacitors electrodes, but the inaccessibility of the electrolyte ions into their micropores and/or interior atoms at higher scan rates, as well as the poor electrical conductivity leads to a higher internal resistance still remains the central issue that limits their being used in high-power-density supercapacitors [9]. Carbon nanotubes (CNTs), its discovery has significantly advanced the science and engineering of carbon materials, and have been considered suitable as a supercapacitor electrode material [62]. In the past decade, CNTs have been widely researched for supercapacitors attribute to the high conductivity, unique mechanical properties, high chemical stability, high aspect ratios and high activated surface areas [63, 64]. As technology advances, various forms of CNTs have been generating in assorted conformations and crystalline order by control manipulation of various parameters in preparation process [65]. At the molecular level, CNTs can be viewed as a graphene sheet rolled up into a nanoscale tube form to produce a single-walled carbon nanotube (SWCNT) (as shown in Fig. 1.8). There may be additional graphene coaxial tubes around the SWCNT core to form a multiwalled carbon nanotube

(MWCNT) [66, 67].

However, CNTs even have moderately small theoretical surface areas ($\approx 50\text{-}1315\text{ m}^2\text{ g}^{-1}$), but they performed higher capacitances over other AC. Because of their unique tubular structures and the high density of mesopores allow fast charge transport and large accessibility of electrolyte ions [9, 68]. As a supercapacitors electrode, the initial work on CNTs was mainly carried out with randomly oriented of MWCNTs, performing a specific capacitor in the $80\text{-}130\text{ F g}^{-1}$ [62, 65]. Compared to MWCNTs, SWCNTs exhibited better electrochemical performances attributed to their large specific surface area ($\approx 1600\text{ m}^2\text{ g}^{-1}$), high aspect ratio, and better accessibility to the electrolyte ions [67, 69]. Aligned CNTs are present unbundled structures, providing more mesopores and accessible surfaces. Moreover, they provide lower contact resistance during the charging–discharging process, bring about large energy and power densities [9, 70].

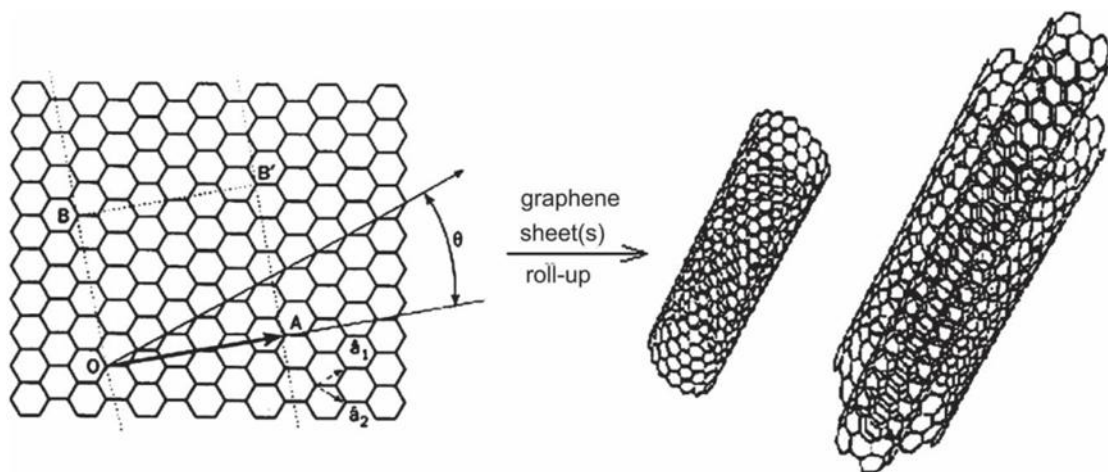


Fig. 1.8 Schematic representation of the CNTs formation by rolling up a 2D graphene sheet of lattice vectors a_1 and a_2 , the roll-up chiral vector $C_h = na_1 + ma_2$, and the chiral angle θ between C_h and a_1 . When the graphene sheet is rolled up to form the cylindrical part of the nanotube, the chiral vector forms the circumference of nanotube's circular cross section with its ends meeting each other. The chiral vector (n, m) defines the tube helicity. If $n - m \neq 3q$ (n, m , and q are integers), the SWCNT is semiconducting; if $n - m = 3q$, the SWCNT is metallic. Reproduced with

permission [67].

3) Graphene

Graphene, the one-atom-thick 2D sheet of sp²-bonded carbon that is densely packed in a honeycomb crystal lattice, is a rising star in carbon material and nanoscience [71]. The unique structure of graphene is endowed its various superior properties such as high electrical and thermal conductivities, good transparency, great mechanical strength, inherent flexibility and huge specific surface area [72, 73]. Thence, during the past decade graphene has attracted a great deal of attention in the fields of microelectronic and optoelectronic devices, energy storage materials, electrocatalysts, polymer composites, and ultrastrong paper-like materials [74-76]. The first piece of graphene was obtained by Andre Geim and Konstantin Novoselov via manual mechanical cleavage of graphite with Scotch tape in 2004 [67, 71]. However, this production method is not applicable on a large scale. Currently, the most common method is reduced graphite oxide method, which exfoliation GO followed by reduction to give the final product (as shown in Fig. 1.9) [14, 71, 77, 78]. Moreover, the other methods are assembling graphene sheets into graphene-based materials with ordered 2D or 3D microstructures and separating graphene sheets with other nanomaterials [73, 79].

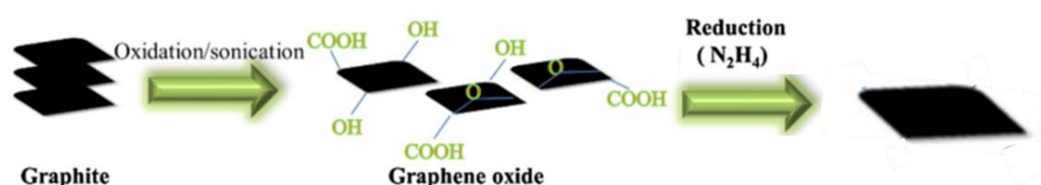


Fig. 1.9 Preparation of reduced graphene oxide by Hummer method [71].

Unlike the current electrochemical capacitors fabricated with AC and CNT, the high specific surface area of graphene does not depend on the distribution of pores. Single or few layered structure of graphene irreversibly aggregate due to the π - π interactions and van der Waals forces, which have a lower degree of agglomeration [80]. What's

more, the excellent electric conductivity and mechanical flexibility of graphene enable its electrodes to undergo fast electron transfer without any significant volume expansion/shrinking during charging-discharging [81]. Hence, many of reports directly utilize the 2D structure of graphene for supercapacitors. A. Yu et al. prepared an ultrathin film (e.g., 25 nm) with a moderate specific capacitor at 111 F g^{-1} , and this value was further decreased by increasing its thickness [82]. In addition, Q. Du reported a method through thermal reduction of graphene oxide powder at a high temperature ($1050 \text{ }^\circ\text{C}$) rapidly generated a large number of gaseous species and exfoliated r-GO sheets into a porous structure with the high specific surface area, while the porous functionalized graphene with the specific capacitor of 233 F g^{-1} [83].

1.3.2 Transition metal oxides-based electrode materials

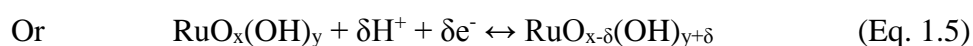
Although carbon-based materials hold great potential as negative electrodes, their intrinsically low specific capacitor and low energy density are major drawbacks. Transition metal oxides, exhibit higher energy density for supercapacitors than that of carbon materials due to the intrinsically fast and reversible redox reactions [73]. As we all know, the pseudocapacitance of transition metal oxides arises from both faradic redox reactions and the electrochemical adsorption/desorption of ions at the electrode/electrolyte interface [84]. The normal conditions for transition metal oxides in supercapacitors application are [85]:

- the metal can exist in two or more oxidation states that coexist over a continuous range with no phase changes involving irreversible modifications of a 3D structure;
- the protons can freely intercalate into the oxide lattice on reduction and out of the lattice on oxidation, allowing facile interconversion of $\text{O}^{2-} \leftrightarrow \text{OH}^-$;
- the oxide should be electronically conductive.

In current, the common transition metal oxides are ruthenium oxide, manganese oxide, cobalt oxide, iron oxide and nickel oxide.

1) Ruthenium dioxide (RuO₂)

RuO₂ is a promising electrode material, and first studied as charge storage material by Conway et al. in 1975, then the concept of a supercapacitor was introduced [86]. RuO₂ has been widely investigated due to its highly reversible redox reactions, three distinct oxidation states (Ru²⁺, Ru³⁺, Ru⁴⁺), high proton conductivity, remarkably high specific capacitance and high rate capability. The pseudocapacitive behaviours of RuO₂ in acid and alkali electrolyte exhibit different reactions. In acid electrolyte, the mechanism was suggested to be as follow (Eq. 1.4 and 1.5):

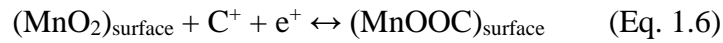


Four steps were proposed to determine the capacitive performance of RuO_x nH₂O: (i) electron hopping within RuO_x nH₂O particles; (ii) electron hopping between particles; (iii) electron hopping between electrode materials and current collectors; and (iv) the proton diffusion within RuO_x nH₂O particles [87]. It is worth noting, the crystallinity of RuO₂ is the key parameter in determining the value of specific capacitance. Although crystallization of RuO₂ can reduce the intraparticle electron hopping resistance of RuO_x nH₂O particles, while it results in an increase in the diffusion barrier of proton within crystalline RuO₂ and a loss of active sites [88]. Accordingly, nanocrystalline RuO_x nH₂O annealed at temperatures close to its crystalline temperatures usually exhibits the highest specific capacitor value [89]. Although amorphous RuO₂ can provide excellent capacitive performance, its drawbacks, such as the high cost and environment impact, hinder it from being used in the commercialization of supercapacitors [85].

2) Manganese dioxide (MnO₂)

Manganese oxides have been regarded a potential electrode material for pseudocapacitor applications owing to its low cost, low toxicity, environment safety and high theoretical capacities, and also have acted as the promising alternative class of materials for RuO₂ [85]. Lee and Goodenough first reported the amorphous MnO₂

could be used as an excellent electrode material for the faradaic electrochemical capacitor in 1999 [90]. After that, aiming the development and application of manganese oxides have attracted major attention. Manganese oxides also have pluralism valence states, including Mn(0), Mn(II), Mn(III), Mn(IV), Mn(V), Mn(VI), and Mn(VII). The capacitance of manganese oxides originates mainly from pseudocapacitive energy storage mechanism, which is attributed to reversible redox transitions involving the exchange of protons and/or cations on the surface and in the bulk of the electrode with the electrolyte, as well as the transitions between Mn(III)/Mn(II), Mn(IV)/Mn(III), and Mn(VI)/Mn(IV) [85, 91]. The surface Faradaic reaction involves the surface adsorption of electrolyte cations ($C^+ = H^+, Li^+, Na^+$ and K^+) on the manganese oxide [92, 93]:



The bulk Faradaic reaction relies on the intercalation or deintercalation of electrolyte cations in the bulk of the manganese oxide [92, 93]:



It is noted that, in both charge storage mechanisms, a redox reaction between the III and IV oxidation states of Mn ions occurs.

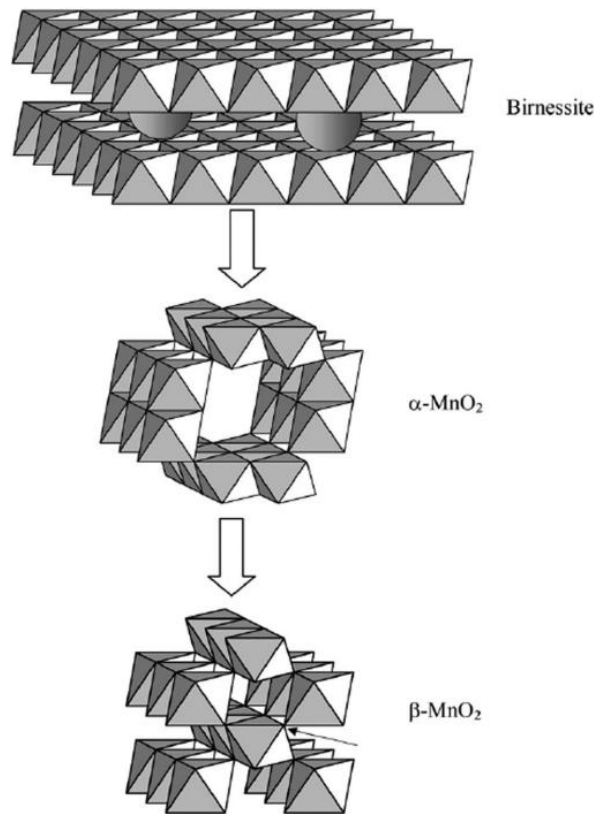


Fig. 1.10 MnO₂ structural transitions induced during material synthesis [85].

Different from RuO₂, the pseudocapacitive behavior of manganese oxides is affected both by physical and chemical factors. Cycling stability is mostly controlled by the microstructure, however, the specific capacitance is controlled mostly by the chemical hydrated state [91]. Similar to RuO₂, manganese oxides also exist in a variety of crystalline structures, including α -, β -, γ -, δ - and λ -MnO₂. Among them, α -, β -, and δ -MnO₂ have a tunnel structure (2×2 octahedral units for α -MnO₂, the relatively large 1D tunnel structured phase; 1×1 octahedral units for β -MnO₂, the more compact and dense 1D tunnel structured phase), and δ -MnO₂ has a relatively open 2D layered structure (as shown in Fig. 11 by birnessite) [85, 94].

Among of them, the 2D layered structure of δ -MnO₂ exhibited outstanding capacitive performance, because the interlayer separation of δ -MnO₂ is about 7 Å, this size can allow a amount of water and stabilizing cations such as Na⁺ or K⁺ between the sheets [95]. Due to this reason, several methods for synthesizing δ -MnO₂ have been developed, such as hydrothermal synthesis, redox reaction synthesis, sol-gel method, template method and so on [28] [96, 97]. However, the partial dissolution of MnO₂ causes the

capacitance degradation during cycling, as well as the low specific surface area and poor electronic conductivity also limit the application of MnO₂ in supercapacitors [85, 98].

3) Iron oxide (Fe₃O₄)

As one of transition-metal oxides, magnetite (Fe₃O₄) have two valence states (Fe²⁺, Fe³⁺) which make a promise to be applied as supercapacitor material. Furthermore, this material has advantages of low cost and environmentally affinity [99]. However, the intrinsic problem of Fe₃O₄ supercapacitor electrode is lack of electrical conductivity (the specific capacitance of pure Fe₃O₄ is 60-80 F g⁻¹) [100]. In particular, the capacitance of the Fe₃O₄ was found to be sensitive to the anion species but not to either alkaline cations or electrolyte pH<11. These behaviors suggest a capacitance mechanism is different from that of either RuO₂ or MnO₂ [87].

In addition, some experimental results indicate that, in Na₂SO₃, the capacitive current of magnetite electrode originates from the combination of electric double layer capacitance (EDLC) and the pseudocapacitance that involves successive reduction of the specifically adsorbed sulfite anions, from SO₃²⁻ through S²⁻, and vice versa. In Na₂SO₄, the current is due entirely to EDLC. The lowest capacitance of magnetite observed in KOH is attributed to the formation of an insulating layer on the magnetite surface. To solve this problem, the common countermeasure is the preparation of hybrid nanostructured material by integrating Fe₃O₄ with a carbon host, where the carbon host acts as the conductive network [101, 102].

1.3.3 Conducting polymer-based electrode materials

Since 1977, American scientists Heeger, MacDiarmid and their Japanese colleague Shirakawa discovered that a synthetic polymer (polyacetylene) could be conductive under certain conditions, conducting polymer materials have attracted more and more

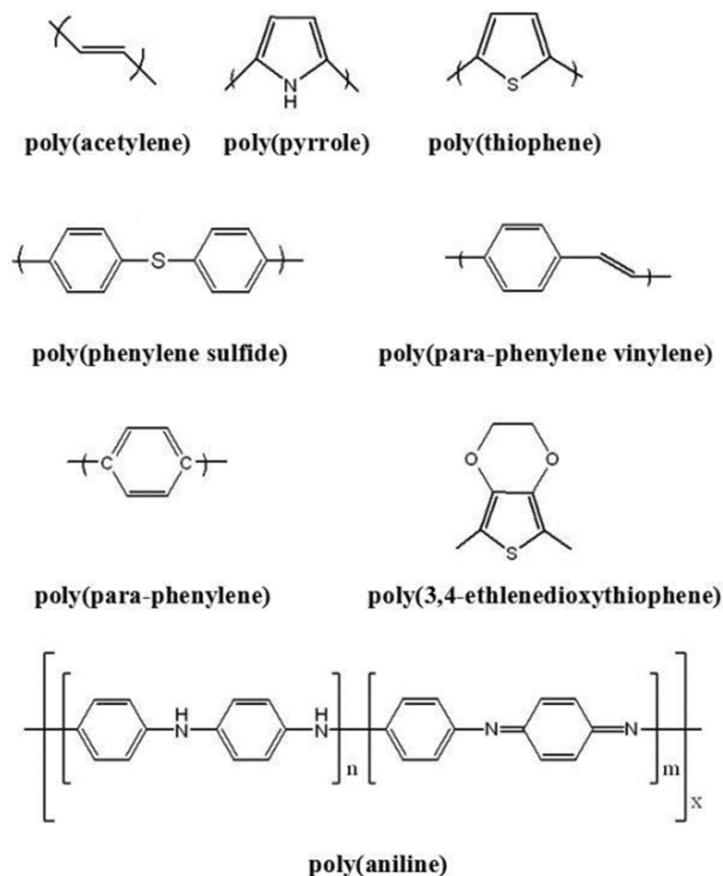
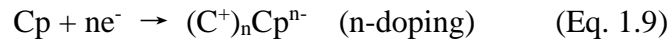
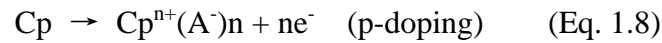


Fig. 1.11 Molecular structures of some conjugated polymers in their neutral form.

attention by scholars [103, 104]. For the revolutionized discovery and development of conducting polymers, the Nobel Prize in Chemistry for 2000 was rewarded to the above scientists [105-107]. Conducting polymers, alternate single-double bonds along the backbone of the polymer is a key property for conjugated conducting polymers, which differentiates them from other polymers. The “sigma” (σ) electrons that form strong covalent bonds between the carbon atoms are localized, whereas the “pi” (π) electrons can be delocalized upon certain operation [108]. For this reason, they can render conductive through the conjugated bond system along the polymer backbone [109]. The molecular structures of some typical conjugated conducting polymers in their neutral form are given in Fig. 1.11.

Most of the conducting polymers show poorly conductive and unstable in the neutral state. However, their conductivity can improve by the formation of charge carriers upon oxidizing (p-doping) or reducing (n-doping) their conjugated backbone [110]. The

simplified reaction (Eq. 1.8 and 1.9) for these two charging processes are as follows [109]:



The typical n-doping conducting polymer are PA and poly(paraphenylene), and these polymers have high impedances. Polypyrrole (PPy) and polyaniline (PANI), they are the typical p-doping conducting polymers [111]. Depending upon the oxidation state, PANI has three basic structures (Fig. 1.12): (a) a fully reduced leucoemeraldine base (LEB); (b) a fully oxidized pernigraniline base (PNB); and (c) a half oxidized/half reduced emeraldine base (EB) state. The protonated or doped EB form is highly conducting, while LEB and PNB are mainly insulating in nature. When EB (Fig. 1.12a) is doped with different acids a polaron is formed through the successive formation of bi-positive species (Fig. 1.12b), bipolaron structure (Fig. 1.12c) and more stable polaron structure (Fig. 1.12d). This polaron structure is responsible for electrical conduction through the hopping mechanism in the crystalline region and hopping may be intra-chain or inter-chain [112]. This process leads to an internal redox reaction converting the semiconducting form of PANI (emeraldine base) to a metallic form (emeraldine salt). The reaction between the different forms of PANI is shown in the Fig. 1.13 [113].

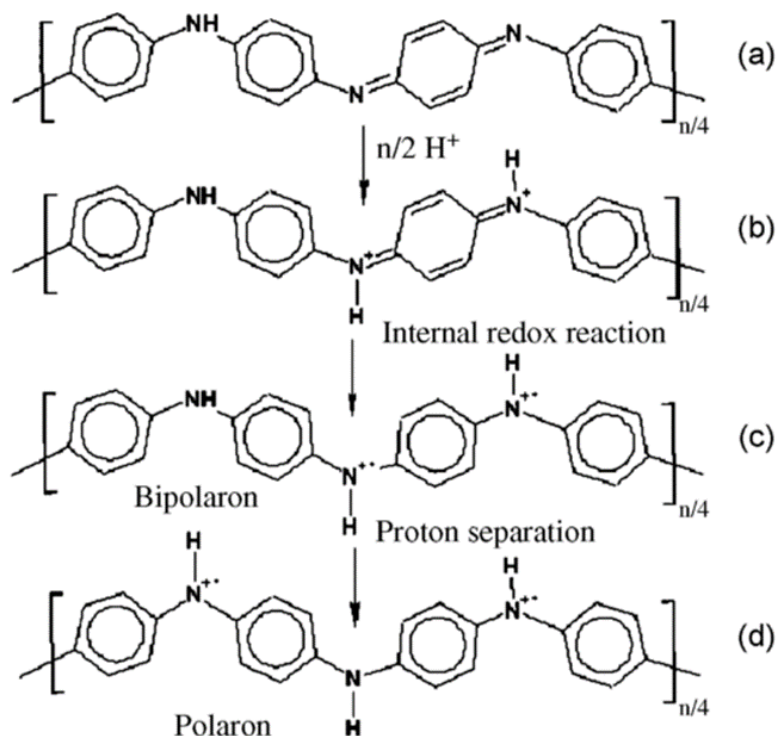


Fig. 1.12 Sketch of EB of polyaniline before protonation (a), after 50% protonation (b) and formation of bipolaron (c) and polaron (d) [112]

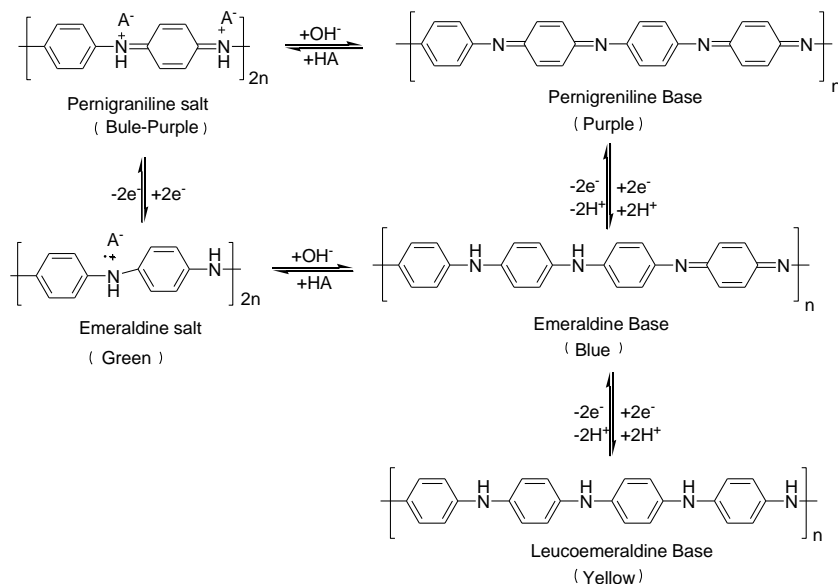


Fig. 1.13 Transformation of relationship between structure of polyaniline and the corresponding colour changes [113]

Conducting polymers are suitable materials for supercapacitors, due to the advantage of high conductivity in a doped state, high storage capacity/reversibility, adjustable redox activity through chemical modification, and low cost/environment impact [114,

115]. The common conducting polymer in supercapacitor applications is PANI [116], PPy [117], polythiophene [118] and their derivatives. PANI and PPy often use as cathode materials due to they can only be p-doped.

There are many reports on applying the above conducting polymer to supercapacitors. For examples, Y. Shi et al. have reported a polypyrrole hydrogels exhibited a high specific capacitance and which reach up to 380 F g^{-1} [119]. A kind of 3D polyaniline has prepared by Y. Gawli et al. by inorganic and organic acid co-doping, and it possesses a nearly constant high specific capacitance of 350 F g^{-1} at the current density rage of $1\sim 40 \text{ A g}^{-1}$ [106]. Even, Y. Huang et al. have prepared a kind of polypyrrole from the molecular ordering, and this kind of polypyrrole exhibited the excellent cycle stability (the capacitance retentions of over 97, 91 and 86 % after 15000, 50000 and 100000 charging/discharging cycles, respectively), and can sustain over 230000 charging/discharging cycles with still about half of initial capacitance retained [120].

Unfortunately, swelling and shrinking of conducting polymer unavoidable occur during the charging/discharging process (due to the intercalating/deintercalating function). This problem will further lead to mechanical degradation of the electrode and fading electrochemical performance during cycling, and then limit the conducting polymer applied to supercapacitors.

1.4 Contribution from this dissertation

Supercapacitors, as one of the most promising energy storage devices, due to their good energy density, superior power density, fast charge/discharge rate, and long cycle life, which make it exhibit promising applications in portable devices, renewable energy and transportation. Based on the different charge storage mechanisms, supercapacitors can generally be divided into two types: the electrical double-layer capacitors (EDLC) and the pseudocapacitors. Carbon materials, such as active carbon, graphene and carbon nanotube are usually used in EDLC electrode, but their low energy density, limited their further application, as well as most of methods to prepare of the above carbon materials often requires complicated preparation conditions or special facilities, leading to the

high cost. In the present work, first, low cost and uncomplicated method of allium-giganteum-like biocarbon (KWB) were derived from sugarcane bagasse, and then different kinds of carbon-based composite materials including manganese dioxide (MnO_2)/KWB, polyaniline (PANI)/KWB and iron oxide (Fe_3O_4)/KWB were obtained. All of the above materials were used as electrode material of supercapacitors, and morphology, chemical composition and electrochemical performance were investigated. Besides, due to the unique structure of KWB, all the composites show the superior performance in supercapacitors.

In Chapter 1, the research backgrounds, research significance, research purpose and the construction of this thesis are particularly described.

In Chapter 2, the properties of experimental materials used in this thesis are presented. The experimental methods and characterizations are also particularly described in this chapter.

In chapter 3, KWB were derived from sugarcane bagasse via one-step carbonization and activation method. The results show that, both the mass ratio of potassium hydroxide (KOH) to sugarcane bagasse and the temperature of carbonization could impact on the morphology and chemical composition of KWB, thereby further affect the electrochemical performance of KWB. Under the optimum conditions, the SEM of KWB shows the excellent 3D hierarchical porous network structure with allium-giganteum-like, which also has the best specific surface area. Its promise the excellent electrochemical performance when used as electrode materials for supercapacitors. What's more, KWB also could be carbon-base to prepare other composites for the further research.

In chapter 4, MnO_2 /KWB (KWBM) composites have been prepared by a simple method. The MnO_2 nanosheets anchored on the surface of biocarbon and obtained the KWBM, and KWB was used as both scaffolds and reducing agents for MnO_2 growth. The analysis results demonstrated that chemical composition and microstructure of KWBM were closely related to the mass ratio of KMnO_4 /KWB, and which further impacted electrochemical performance of KWBM profoundly. Especially, the KWBM-4 exhibited a higher specific capacitance of 402 F g^{-1} at a current density of 1 A g^{-1} in

three-electrode system. The asymmetric two-electrode system with outstanding energy density was assembled by employing the KWBM-4 as the positive electrode and the KWB as the negative electrode. The two-electrode system displays a high energy density of 25.9 Wh kg^{-1} at a power density of 750 W kg^{-1} within a potential range of 0-1.5 V. Furthermore, the system exhibited high cycle stability with only 5.8 % loss of its initial capacitance after 2000 cycles.

In chapter 5, a coral-like polyaniline/KWB (PANI/KWB) composites were prepared via in-site polymerization method. The PANI/KWB composites were obtained using KWB as the scaffolds for PANI growth and [CMMIm]Cl ionic liquid as the dopant. The different mass ratio of aniline monomer (An) and KWB be researched. The results indicated that chemical composition and microstructure of PANI/KWB were closely related to the mass ratio of aniline monomer (An) and KWB, and which further impacted electrochemical performance of PANI/KWB profoundly. Especially, the PANI/KWB-4 exhibited a highest specific capacitance of 447 F g^{-1} at a current density of 0.5 A g^{-1} . Furthermore, the asymmetric two-electrode system based on PANI/KWB-4 as positive electrode and KWB as negative electrode is successfully assembled with a voltage window of 0~1.6 V, exhibiting high energy density (27.3 Wh kg^{-1}) and power density (800 W kg^{-1}), and excellent cycling stability (87% capacitance retention after 2000 cycles).

In chapter 6, $\text{Fe}_3\text{O}_4/\text{KWB}$ nanocomposites (KBF_e) have been prepared via a chemical coprecipitation method under different mass ratio of Fe_3O_4 to KWB. As a result, the chemical composition and microstructure of the KBF_e were intimately related to the mass ratio of Fe_3O_4 and KWB, which impacted the electrochemical performance of the KBF_e profoundly. Especially, the KBF_e-4 displayed the highest specific capacitance of 342 F g^{-1} at a current density of 1 A g^{-1} . Furthermore, the asymmetric two-electrode system based on KWBM composite as positive electrode and KBF_e-4 as negative electrode was successfully assembled with a voltage window of 0~1.6 V, and exhibited high energy density (29.1 Wh kg^{-1}) and power density (800 W kg^{-1}), along with excellent cycling stability (89.5% capacitance retention after 1000 cycles).

In chapter 7, general conclusions of the study are made.

References

- [1] M.R. Islam, S. Mekhilef, R. Saidur, Progress and recent trends of wind energy technology, *Renew. Sustain. Energy Rev.* 21 (2013) 456–468.
- [2] R.S. El-Emam, I. Dincer, Thermodynamic and thermoeconomic analyses of seawater reverse osmosis desalination plant with energy recovery, *Energy*. 64 (2014) 154–163.
- [3] S. Hähnlein, P. Bayer, G. Ferguson, P. Blum, Sustainability and policy for the thermal use of shallow geothermal energy, *Energy Policy*. 59 (2013) 914–925.
- [4] F. Khalid, I. Dincer, M.A. Rosen, Energy and exergy analyses of a solar-biomass integrated cycle for multigeneration, *Sol. Energy*. 112 (2015) 290–299.
- [5] A. Pospischil, M.M. Furchi, T. Mueller, Solar-energy conversion and light emission in an atomic monolayer p–n diode, *Nat. Nanotechnol.* 9 (2014) 257–261.
- [6] Y. Shi, Y. Ge, J. Chang, H. Shao, Y. Tang, Garden waste biomass for renewable and sustainable energy production in China: Potential, challenges and development, *Renew. Sustain. Energy Rev.* 22 (2013) 432–437.
- [7] H. Li, Y. Gong, C. Fu, H. Zhou, W. Yang, M. Guo, M. Li, Y. Kuang, A novel method to prepare a nanotubes@mesoporous carbon composite material based on waste biomass and its electrochemical performance, *J. Mater. Chem. A*. 5 (2017) 3875–3887.
- [8] C. Zhong, Y. Deng, W. Hu, J. Qiao, L. Zhang, J. Zhang, A review of electrolyte materials and compositions for electrochemical supercapacitors, *Chem. Soc. Rev.* 44 (2015) 7484–7539.
- [9] N. Choudhary, C. Li, J. Moore, N. Nagaiah, L. Zhai, Y. Jung, J. Thomas, Asymmetric Supercapacitor Electrodes and Devices, *Adv. Mater.* 29 (2017) 1605336.
- [10] S. Li, C. Yu, J. Yang, C. Zhao, M. Zhang, H. Huang, Z. Liu, W. Guo, J. Qiu, A superhydrophilic “nanoglue” for stabilizing metal hydroxides onto carbon materials for high-energy and ultralong-life asymmetric supercapacitors, *Energy Environ. Sci.* 10 (2017) 1958–1965.

- [11] J. Chmiola, P.L.T. Celine Largeot, P. Simon, Y. Gogotsi, Monolithic carbide-derived carbon films for micro-supercapacitors, *Science*. 328 (2010) 480–483.
- [12] Y. Huang, J. Liang, Y. Chen, An overview of the applications of graphene-based materials in supercapacitors, *Small*. 8 (2012) 1805–1834.
- [13] L.L. Zhang, X.S. Zhao, Carbon-based materials as supercapacitor electrodes, *Chem. Soc. Rev.* 38 (2009) 2520–2531.
- [14] A. Ghosh, Y.H. Lee, Carbon-based electrochemical capacitors, *ChemSusChem*. 5 (2012) 480–499.
- [15] C. Choi, J.A. Lee, A.Y. Choi, Y.T. Kim, X. Leprõ, M.D. Lima, R.H. Baughman, S.J. Kim, Flexible supercapacitor made of carbon nanotube yarn with internal pores, *Adv. Mater.* 26 (2014) 2059–2065.
- [16] Z. Fan, J. Yan, T. Wei, L. Zhi, G. Ning, T. Li, F. Wei, Asymmetric supercapacitors based on graphene/MnO₂ and activated carbon nanofiber electrodes with high power and energy density, *Adv. Funct. Mater.* 21 (2011) 2366–2375.
- [17] J. Ding, H. Wang, Z. Li, K. Cui, D. Karpuzov, X. Tan, A. Kohandehghan, D. Mitlin, Peanut shell hybrid sodium ion capacitor with extreme energy–power rivals lithium ion capacitors, *Energy Environ. Sci.* 8 (2015) 941–955.
- [18] L.F. Chen, Z.H. Huang, H.W. Liang, Q.F. Guan, S.H. Yu, Bacterial-cellulose-derived carbon nanofiber@MnO₂ and nitrogen-doped carbon nanofiber electrode materials: An asymmetric supercapacitor with high energy and power density, *Adv. Mater.* 25 (2013) 4746–4752.
- [19] L. Wu, L. Hao, B. Pang, G. Wang, Y. Zhang, X. Li, MnO₂ nanoflowers and polyaniline nanoribbons grown on hybrid graphene/Ni 3D scaffolds by in situ electrochemical techniques for high-performance asymmetric supercapacitors, *J. Mater. Chem. A*. 5 (2017) 4629–4637.
- [20] M. Zhi, C. Xiang, J. Li, M. Li, N. Wu, Nanostructured carbon–metal oxide composite electrodes for supercapacitors: a review, *Nanoscale*. 5 (2013) 72–88.
- [21] Helmholtz, Ueber einige Gesetze, *Ann. Phys.* 165 (1853) 211–233.
- [22] F. Béguin, V. Presser, A. Balducci, E. Frackowiak, Carbons and electrolytes for advanced supercapacitors, *Adv. Mater.* 26 (2014) 2219–2251.

- [23] M. Gouy, Sur la constitution de la charge électrique à la surface d'un électrolyte, *J. Phys. Théorique Appliquée*. 9 (1910) 457–468.
- [24] D.L. Chapman, A contribution to the theory of electrocapillarity, *Philos. Mag. Ser.* 6. 25 (1913) 475–481.
- [25] H. Wang, L. Pilon, Accurate simulations of electric double layer capacitance of ultramicroelectrodes, *J. Phys. Chem. C*. 115 (2011) 16711–16719.
- [26] M. Winter, R.J. Brodd, What are batteries, fuel cells, and supercapacitors? *Chem. Rev.* 104 (2004) 4245–4269.
- [27] A.G. Pandolfo, A.F. Hollenkamp, Carbon properties and their role in supercapacitors, *J. Power Sources*. 157 (2006) 11–27.
- [28] M. Huang, F. Li, F. Dong, Y.X. Zhang, L.L. Zhang, MnO₂-based nanostructures for high-performance supercapacitors, *J. Mater. Chem. A*. 3 (2015) 21380–21423.
- [29] J. Cao, X. Li, Y. Wang, F.C. Walsh, J.H. Ouyang, D. Jia, Y. Zhou, Materials and fabrication of electrode scaffolds for deposition of MnO₂ and their true performance in supercapacitors, *J. Power Sources*. 293 (2015) 657–674.
- [30] D.S. Su, R. Schlögl, Nanostructured carbon and carbon nanocomposites for electrochemical energy storage applications, *ChemSusChem*. 3 (2010) 136–168.
- [31] E. Raymundo-Piñero, K. Kierzek, J. Machnikowski, F. Béguin, Relationship between the nanoporous texture of activated carbons and their capacitance properties in different electrolytes, *Carbon N. Y.* 44 (2006) 2498–2507.
- [32] R. Liu, S.M. Mahurin, C. Li, R.R. Unocic, J.C. Idrobo, H. Gao, S.J. Pennycook, S. Dai, Dopamine as a carbon source: The controlled synthesis of hollow carbon spheres and yolk-structured carbon nanocomposites, *Angew. Chemie - Int. Ed.* 50 (2011) 6799–6802.
- [33] L. Qie, W. Chen, H. Xu, X. Xiong, Y. Jiang, F. Zou, X. Hu, Y. Xin, Z. Zhang, Y. Huang, Synthesis of functionalized 3D hierarchical porous carbon for high-performance supercapacitors, *Energy Environ. Sci.* 6 (2013) 2497–2504.
- [34] Z. Li, Z. Xu, X. Tan, H. Wang, C.M.B. Holt, T. Stephenson, B.C. Olsen, D. Mitlin, Mesoporous nitrogen-rich carbons derived from protein for ultra-high capacity battery anodes and supercapacitors, *Energy Environ. Sci.* 6 (2013) 871–878.

- [35]F. Zheng, Y. Yang, Q. Chen, High lithium anodic performance of highly nitrogen-doped porous carbon prepared from a metal-organic framework, *Nat. Commun.* 5 (2014) 1–10.
- [36]J. Chen, J. Qiu, B. Wang, H. Feng, Y. Yu, E. Sakai, Manganese dioxide / biocarbon composites with superior performance in supercapacitors, *J. Electroanal. Chem.* 791 (2017) 159–166.
- [37]N. Manyala, A. Bello, F. Barzegar, A.A. Khaleed, D.Y. Momodu, J.K. Dangbegnon, Coniferous pine biomass : A novel insight into sustainable carbon materials for supercapacitors electrode, *Mater. Chem. Phys.* (2016) 1–9.
- [38]W. Chen, H. Yang, Y. Chen, X. Chen, Y. Fang, H. Chen, Biomass pyrolysis for nitrogen-containing liquid chemicals and nitrogen-doped carbon materials, *J. Anal. Appl. Pyrolysis.* 120 (2016) 186–193.
- [39]A.H. Basta, V. Fierro, H. El-Saied, A. Celzard, 2-Steps KOH activation of rice straw: An efficient method for preparing high-performance activated carbons, *Bioresour. Technol.* 100 (2009) 3941–3947.
- [40]B. Xu, Y. Chen, G. Wei, G. Cao, H. Zhang, Y. Yang, Activated carbon with high capacitance prepared by NaOH activation for supercapacitors, *Mater. Chem. Phys.* 124 (2010) 504–509.
- [41]T.E. Rufford, D. Hulicova-Jurcakova, K. Khosla, Z. Zhu, G.Q. Lu, Microstructure and electrochemical double-layer capacitance of carbon electrodes prepared by zinc chloride activation of sugar cane bagasse, *J. Power Sources.* 195 (2010) 912–918.
- [42]K.S.W. Sing, Reporting physisorption data for gas/solid systems with special reference to the determination of surface area and porosity (Recommendations 1984), *Pure Appl. Chem.* 57 (1985) 603-619.
- [43]Y. Zhai, Y. Dou, D. Zhao, P.F. Fulvio, R.T. Mayes, S. Dai, Carbon materials for chemical capacitive energy storage, *Adv. Mater.* 23 (2011) 4828–4850.
- [44]K. Kierzek, E. Frackowiak, G. Lota, G. Gryglewicz, J. Machnikowski, Electrochemical capacitors based on highly porous carbons prepared by KOH activation, *Electrochim. Acta.* 49 (2004) 515–523.
- [45]C. Largeot, C. Portet, J. Chmiola, P.L. Taberna, Y. Gogotsi, P. Simon, Relation

- between the ion size and pore size for an electric double-layer capacitor, *J. Am. Chem. Soc.* 130 (2008) 2730–2731.
- [46] P. Simon, Y. Gogotsi, Capacitive Energy Storage in Nanostructured Carbon–Electrolyte Systems, *Acc. Chem. Res.* 46 (2013) 1094–1103.
- [47] M. Graglia, J. Pampel, T. Hantke, T.P. Feller, D. Esposito, Nitro Lignin-Derived Nitrogen-Doped Carbon as an Efficient and Sustainable Electrocatalyst for Oxygen Reduction, *ACS Nano.* 10 (2016) 4364–4371.
- [48] W. Sun, T. Peng, Y. Liu, S. Xu, J. Yuan, S. Guo, X.-Z. Zhao, Hierarchically porous hybrids of polyaniline nanoparticles anchored on reduced graphene oxide sheets as counter electrodes for dye-sensitized solar cells, *J. Mater. Chem. A.* 1 (2013) 2762–2768.
- [49] H. Chen, D. Liu, Z. Shen, B. Bao, S. Zhao, L. Wu, Functional Biomass Carbons with Hierarchical Porous Structure for Supercapacitor Electrode Materials, *Electrochim. Acta.* 180 (2015) 241–251.
- [50] R.Q. Wang, Studies and Characterisations of Activated Carbons Used for Carbon / Carbon Supercapacitors, *J. Power Sources.* 5 (2011) 866–868.
- [51] D. Qu, Studies of the activated carbons used in double-layer supercapacitors, *J. Power Sources.* 109 (2002) 403–411.
- [52] L. Liu, Z. Niu, J. Chen, Unconventional supercapacitors from nanocarbon-based electrode materials to device configurations, *Chem. Soc. Rev.* 45 (2016) 4340–4363.
- [53] M. Inagaki, H. Konno, O. Tanaike, Carbon materials for electrochemical capacitors, *J. Power Sources.* 195 (2010) 7880–7903.
- [54] F. Hu, J. Wang, S. Hu, L. Li, G. Wang, J. Qiu, X. Jian, Inherent N,O-containing carbon frameworks as electrode materials for high-performance supercapacitors, *Nanoscale.* 8 (2016) 16323–16331.
- [55] C. Wang, L. Sun, Y. Zhou, P. Wan, X. Zhang, J. Qiu, P/N co-doped microporous carbons from H₃PO₄-doped polyaniline by in situ activation for supercapacitors, *Carbon N. Y.* 59 (2013) 537–546.
- [56] Y. Chang, C. Yuan, Y. li, L. Cheng, T. Wu, B. Zeng, Y. Xu, L. Dai, Controllable Fabrication of N and B Co-Doped Carbon Shell on the Surface of TiO₂ as a Support

- for Boosting the Electrochemical Performances, *J. Mater. Chem. A.* 5 (2017) 1672-1678.
- [57]D. Jana, C.-L. Sun, L.-C. Chen, K.-H. Chen, Effect of chemical doping of boron and nitrogen on the electronic, optical, and electrochemical properties of carbon nanotubes, *Prog. Mater. Sci.* 58 (2013) 565–635.
- [58]E. Frackowiak, Carbon materials for supercapacitor application, *Phys. Chem. Chem. Phys.* 9 (2007) 1774.
- [59]S. Gao, Y. Chen, H. Fan, X. Wei, C. Hu, H. Luo, L. Qu, Large scale production of biomass-derived N-doped porous carbon spheres for oxygen reduction and supercapacitors, *J. Mater. Chem. A.* 2 (2014) 3317.
- [60]W.H. Li, K. Ding, H.R. Tian, M.S. Yao, B. Nath, W.H. Deng, Y. Wang, G. Xu, Conductive Metal–Organic Framework Nanowire Array Electrodes for High-Performance Solid-State Supercapacitors, *Adv. Funct. Mater.* 27 (2017) 1–7.
- [61]Z. Ling, Z. Wang, M. Zhang, C. Yu, G. Wang, Y. Dong, S. Liu, Y. Wang, J. Qiu, Sustainable Synthesis and Assembly of Biomass-Derived B/N Co-Doped Carbon Nanosheets with Ultrahigh Aspect Ratio for High-Performance Supercapacitors, *Adv. Funct. Mater.* 26 (2016) 111–119.
- [62]C. Niu, E.K. Sichel, R. Hoch, D. Moy, H. Tennent, High power electrochemical capacitors based on carbon nanotube electrodes, *Appl. Phys. Lett.* 70 (1997) 1480-1482.
- [63]P.J. Hall, M. Mirzaeian, S.I. Fletcher, F.B. Sillars, A.J.R. Rennie, G.O. Shitta-Bey, G. Wilson, A. Cruden, R. Carter, Energy storage in electrochemical capacitors: designing functional materials to improve performance, *Energy Environ. Sci.* 3 (2010) 1238-1251.
- [64]S. Iijima, Helical microtubules of graphitic carbon, *Nature.* 354 (1991) 56–58.
- [65]E. Frackowiak, K. Jurewicz, K. Szostak, S. Delpeux, F. Béguin, Nanotubular materials as electrodes for supercapacitors, *Fuel Process. Technol.* 77–78 (2002) 213–219.
- [66]P.J.F.H. (Department of Chemistry), Carbon Nanotubes and Related Structures: New materials for the Twenty-first Century, *Carbon N. Y.* 38 (2000) 787–788.

- [67]L. Dai, D.W. Chang, J.-B. Baek, W. Lu, Carbon Nanomaterials for Advanced Energy Conversion and Storage, *Small*. 8 (2012) 1130–1166.
- [68]H. Pan, J. Li, Y.P. Feng, Carbon nanotubes for supercapacitor, *Nanoscale Res. Lett.* 5 (2010) 654–668.
- [69]R.H. Baughman, A.A. Zakhidov, W.A. De Heer, Carbon nanotubes - The route toward applications, *Science*. 297 (2002) 787–792.
- [70]M. Saghafi, F. Mahboubi, S. Mohajezadeh, R. Holze, Preparation of vertically aligned carbon nanotubes and their electrochemical performance in supercapacitors, *Synth. Met.* 195 (2014) 252–259.
- [71]K.S. Novoselov, A.K. Geim, S.V. Morozov, D. Jiang, Y. Zhang, S.V. Dubonos, I.V. Grigorieva, A.A. Firsov, Electric field effect in atomically thin carbon films., *Science* (80-.). 306 (2004) 666–669.
- [72]K.S. Novoselov, V.I. Fal'ko, L. Colombo, P.R. Gellert, M.G. Schwab, K. Kim, A roadmap for graphene, *Nature*. 490 (2012) 192-200.
- [73]Y. Sun, Q. Wu, G. Shi, Graphene based new energy materials, *Energy Environ. Sci.* 4 (2011) 1113-1132.
- [74]D. Chen, L. Tang, J. Li, Graphene-based materials in electrochemistry, *Chem. Soc. Rev.* 39 (2010) 3157-3180.
- [75]F. Bonaccorso, Z. Sun, T. Hasan, A.C. Ferrari, Graphene photonics and optoelectronics, *Nat. Photonics*. 4 (2010) 611–622.
- [76]J. Xia, F. Chen, J. Li, N. Tao, Measurement of the quantum capacitance of graphene, *Nat. Nanotechnol.* 4 (2009) 505–509.
- [77]S. Stankovich, D.A. Dikin, G.H.B. Dommett, K.M. Kohlhaas, E.J. Zimney, E.A. Stach, R.D. Piner, S.B.T. Nguyen, R.S. Ruoff, Graphene-based composite materials, *Nature*. 442 (2006) 282–286.
- [78]Y. He, W. Chen, X. Li, Z. Zhang, J. Fu, C. Zhao, E. Xie, Freestanding three-dimensional graphene/MnO₂ composite networks as ultralight and flexible supercapacitor electrodes, *ACS Nano*. 7 (2013) 174–182.
- [79]S. Bose, T. Kuila, A.K. Mishra, R. Rajasekar, N.H. Kim, J.H. Lee, Carbon-based nanostructured materials and their composites as supercapacitor electrodes, *J. Mater.*

Chem. 22 (2012) 767–784.

- [80] G. Eda, M. Chhowalla, Chemically derived graphene oxide: Towards large-area thin-film electronics and optoelectronics, *Adv. Mater.* 22 (2010) 2392–2415.
- [81] S. Chen, W. Xing, J. Duan, X. Hu, S.Z. Qiao, Nanostructured morphology control for efficient supercapacitor electrodes, *J. Mater. Chem. A.* 1 (2013) 2941–2954.
- [82] A. Yu, I. Roes, A. Davies, Z. Chen, Ultrathin, transparent, and flexible graphene films for supercapacitor application, *Appl. Phys. Lett.* 96 (2010) 1–4.
- [83] Q. Du, M. Zheng, L. Zhang, Y. Wang, J. Chen, L. Xue, W. Dai, G. Ji, J. Cao, Preparation of functionalized graphene sheets by a low-temperature thermal exfoliation approach and their electrochemical supercapacitive behaviors, *Electrochim. Acta.* 55 (2010) 3897–3903.
- [84] Y. Wang, Y. Song, Y. Xia, Electrochemical capacitors: mechanism, materials, systems, characterization and applications, *Chem. Soc. Rev.* 45 (2016) 5925–5950.
- [85] G. Wang, L. Zhang, J. Zhang, A review of electrode materials for electrochemical supercapacitors, *Chem. Soc. Rev.* 41 (2012) 797–828.
- [86] B.E. Conway, Transition from “Supercapacitor” to “Battery” Behavior in Electrochemical Energy Storage, 138 (1991) 1539-1548.
- [87] P.-C. Chen, G. Shen, Y. Shi, H. Chen, C. Zhou, Preparation and Characterization of Flexible Asymmetric Supercapacitors Based on Transition-Metal-Oxide Nanowire/Single-Walled Carbon Nanotube Hybrid Thin-Film Electrodes, *ACS Nano.* 4 (2010) 4403–4411.
- [88] M.Y. Ho, P.S. Khiew, D. Isa, T.K. Tan, W.S. Chiu, C.H. Chia, A Review of Metal Oxide Composite Electrode Materials for Electrochemical Capacitors, *Nano.* 9 (2014) 1430002.
- [89] J.P. Zheng, Hydrous Ruthenium Oxide as an Electrode Material for Electrochemical Capacitors, *J. Electrochem. Soc.* 142 (1995) 2699-2703.
- [90] H.Y. Lee, J.B. Goodenough, Supercapacitor Behavior with KCl Electrolyte, *J. Solid State Chem.* 144 (1999) 220–223.
- [91] A. González, E. Goikolea, J. Andoni, R. Mysyk, Review on supercapacitors : Technologies and materials, 58 (2016) 1189–1206.

- [92] M. Toupin, T. Brousse, D. Be, Charge Storage Mechanism of MnO₂ Electrode Used in Aqueous Electrochemical Capacitor, (2004) 3184–3190.
- [93] J. Yan, Q. Wang, T. Wei, Z. Fan, Recent advances in design and fabrication of electrochemical supercapacitors with high energy densities, *Adv. Energy Mater.* 4 (2014) 1300816.
- [94] S.W. Donne, A.F. Hollenkamp, B.C. Jones, Structure, morphology and electrochemical behaviour of manganese oxides prepared by controlled decomposition of permanganate, *J. Power Sources.* 195 (2010) 367–373.
- [95] S. Devaraj, N. Munichandraiah, Effect of Crystallographic Structure of MnO₂ on Its Electrochemical Capacitance Properties, *J. Phys. Chem. C.* 112 (2008) 4406–4417.
- [96] W. Chen, R.B. Rakhi, Q. Wang, M.N. Hedhili, H.N. Alshareef, Morphological and electrochemical cycling effects in MnO₂ nanostructures by 3D electron tomography, *Adv. Funct. Mater.* 24 (2014) 3130–3143.
- [97] N. Li, X. Zhu, C. Zhang, L. Lai, R. Jiang, J. Zhu, Controllable synthesis of different microstructured MnO₂ by a facile hydrothermal method for supercapacitors, *J. Alloys Compd.* 692 (2017) 26–33.
- [98] H. Zheng, F. Tang, M. Lim, A. Mukherji, X. Yan, L. Wang, G.Q. (Max) Lu, Multilayered films of cobalt oxyhydroxide nanowires/manganese oxide nanosheets for electrochemical capacitor, *J. Power Sources.* 195 (2010) 680–683.
- [99] Q. Wang, L. Jiao, H. Du, Y. Wang, H. Yuan, Fe₃O₄ nanoparticles grown on graphene as advanced electrode materials for supercapacitors, *J. Power Sources.* 245 (2014) 101–106.
- [100] T. Cottineau, M. Toupin, T. Delahaye, T. Brousse, D. Bédanger, Nanostructured transition metal oxides for aqueous hybrid electrochemical supercapacitors, *Appl. Phys. A Mater. Sci. Process.* 82 (2006) 599–606.
- [101] D. Xuan, W. Chengyang, C. Mingming, J. Yang, W. Jin, Electrochemical performances of nanoparticle Fe₃O₄/activated carbon supercapacitor using KOH electrolyte solution, *J. Phys. Chem. C.* 113 (2009) 2643–2646.
- [102] J. Pu, L. Shen, S. Zhu, J. Wang, W. Zhang, Z. Wang, Fe₃O₄@C core-shell

- microspheres: Synthesis, characterization, and application as supercapacitor electrodes, *J. Solid State Electrochem.* 18 (2014) 1067–1076.
- [103] Y.W. Park, A. Denenstien, C.K. Chiang, A.J. Heeger, A.G. MacDiarmid, Semiconductor-metal transition in doped (CH)_x: Thermoelectric power, *Solid State Commun.* 29 (1979) 747–751.
- [104] S. Hideki, E.J. Louis, A.G. MacDiarmid, C.K. Chiang, A.J. Heeger, Synthesis of Electrically-Conducting organic Polymers: Halogen Derivatives of Polyacetylene, (CH)_x, *J.C.S.*, *Chem. Commun.* (1977) 1–5.
- [105] A.G. Macdiarmid, J.C. Chiang, A.F. Richter, A.J. Epstein, Polyaniline: a new concept in conducting polymers, *Synth. Met.* 18 (1987) 285–290.
- [106] Y. Gawli, A. Banerjee, D. Dhakras, M. Deo, D. Bulani, 3D Polyaniline Architecture by Concurrent Inorganic and Organic Acid Doping for Superior and Robust High Rate Supercapacitor Performance, *Nat. Publ. Gr.* (2016) 1–10.
- [107] R. Gangopadhyay, A. De, Conducting polymer nanocomposites: A brief overview, *Chem. Mater.* 12 (2000) 608–622.
- [108] L. Ghasemi-Mobarakeh, M.P. Prabhakaran, M. Morshed, M.H. Nasr-Esfahani, H. Baharvand, S. Kiani, S.S. Al-Deyab, S. Ramakrishna, Application of conductive polymers, scaffolds and electrical stimulation for nerve tissue engineering, *J. Tissue Eng. Regen. Med.* 5 (2011) e17–e35.
- [109] G.A. Snook, P. Kao, A.S. Best, Conducting-polymer-based supercapacitor devices and electrodes, *J. Power Sources.* 196 (2011) 1–12.
- [110] D. Kumar, R.C. Sharma, Advances in conductive polymers, *Eur. Polym. J.* 34 (1998) 1053–1060.
- [111] K. Naoi, S. Suematsu, A. Manago, Electrochemistry of poly(1,5-diaminoanthraquinone) and its application in electrochemical capacitor materials, *J. Electrochem. Soc.* 147 (2000) 420–426.
- [112] S. Bhadra, D. Khastgir, N.K. Singha, J.H. Lee, Progress in preparation, processing and applications of polyaniline, *Prog. Polym. Sci.* 34 (2009) 783–810.
- [113] U. Lange, N. V. Roznyatovskaya, V.M. Mirsky, Conducting polymers in chemical sensors and arrays, *Anal. Chim. Acta.* 614 (2008) 1–26.

- [114] R. Ramya, R. Sivasubramanian, M. V Sangaranarayanan, *Electrochimica Acta* Conducting polymers-based electrochemical supercapacitors Progress and prospects, *Electrochim. Acta.* 101 (2013) 109–129.
- [115] L.Z. Fan, J. Maier, High-performance polypyrrole electrode materials for redox supercapacitors, *Electrochem. Commun.* 8 (2006) 937–940.
- [116] Y.E. Miao, W. Fan, D. Chen, T.X. Liu, High-Performance Supercapacitors Based on Hollow Polyaniline Nanofibers by Electrospinning, *ACS Appl. Mater. Interfaces.* 5 (2013) 4423–4428.
- [117] Y. Huang, H. Li, Z. Wang, M. Zhu, Z. Pei, Q. Xue, Y. Huang, C. Zhi, Nano Energy Nanostructured Polypyrrole as a flexible electrode material of supercapacitor, *Nano Energy.* (2016) 1–17.
- [118] A. Alabadi, S. Razzaque, Z. Dong, W. Wang, B. Tan, Graphene oxide-polythiophene derivative hybrid nanosheet for enhancing performance of supercapacitor, *J. Power Sources.* 306 (2016) 241–247.
- [119] Y. Shi, L. Pan, B. Liu, Y. Wang, Y. Cui, Z. Bao, G. Yu, Nanostructured conductive polypyrrole hydrogels as high-performance, flexible supercapacitor electrodes, *J. Mater. Chem. A.* 2 (2014) 6086–6091.
- [120] Y. Huang, M. Zhu, Z. Pei, Y. Huang, H. Geng, C. Zhi, Extremely Stable Polypyrrole Achieved via Molecular Ordering for Highly Flexible Supercapacitors, *ACS Appl. Mater. Interfaces.* 8 (2016) 2435–2440.

Chapter 2 Materials, experimental and characterizations

2.1 Materials

2.1.1 Chemical reagents

1) Sugarcane bagasse

Sugarcane bagasse is the remaining biomass waster after the sugarcane has been squeezed. Due to the amount of fiber inside is about 50%, sugarcane bagasse mainly used for paper and other industries [1]. However, in this thesis, sugarcane bagasse as a biomass waster is chosen to use as a carbon source for preparing the biomass activated carbon. Before used as the material, the sugarcane bagasse was cut into small pieces (opening size approximately 2 mm) by family-use grinder and washed with distilled water for 8 h at 90 oC, and then dried at 80 oC for 24 h. The sugarcane bagasse was bought from Nanning (Guangxi, China).

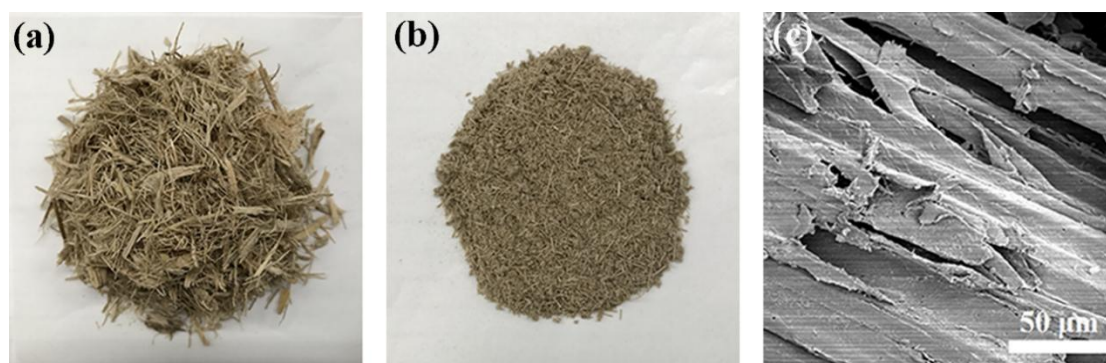


Fig. 2.1 Digital photograph of sugarcane bagasse (a), after crushing treatment (b) and SEM image of sugarcane bagasse after crushing treatment (c).

2) Aniline

Aniline is a six-membered heterocyclic aromatic organic compound with the formula

C₆H₇N. It is a colorless liquid and the color will become darker when it is exposed to air. Usually, it is purified by distillation immediately prior to use. In this thesis, aniline was used as a monomer to prepare polyaniline by the oxidation of aniline. Aniline (analytical grade reagent) was purchased from Nacalai Tesque, Inc. (Kyoto, Japan) and freshly distilled under pressure before use.

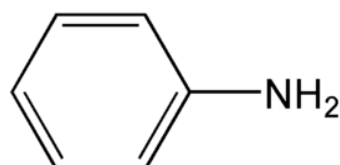


Fig. 2.2 Structure of aniline.

3) 1-methyl-3-alkylcarboxylic acid imidazolium chloride ([CMMIm]Cl) ionic liquid

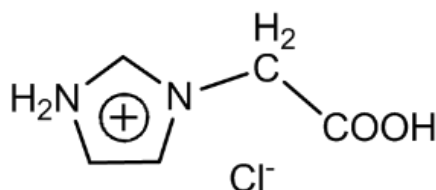


Fig. 2.3 Structure of [CMMIm]Cl IL

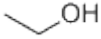
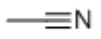
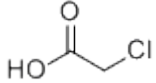
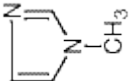
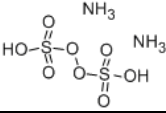
Ionic liquids (ILs) also named room temperature molten salt, are a special class of salts that have melting points at or close to ambient temperature, which molecular structures were synthesized to compose bounded anions and usually organic cations with long chain [2]. Due to the advantages of good thermal stability, low flammability, high electrochemical stability, high ionic and thermal conductivity, ILs have been extensive applied as solvents, separation media, electrolytes, and lubricants in many fields.

In this thesis, we used [CMMIm]Cl IL to prepared PANI/KWB composites, and the [CMMIm]Cl IL was synthesis in lab. [CMMIm]Cl is a brønsted acidic ILs, which has acidic groups to provide a proton acid environmental for doped state PANI. The cation

of [CMMIm]Cl IL is ([CMMIm]⁺, has imidazole ring) will enter the main chain by charge balance, which is benefit for the regularity of the PANI chain, and further has a beneficial effect on the electrochemical performance of PANI. In addition, the [CMMIm]Cl IL is also a surfactant, and its addition can promote the dispersion of An monomer on the surface of KWB.

4) Other materials

Table 2.1 Other materials used in this thesis work

Name	Molecular formula	Structure formula	Molecular weight	Density (g cm ⁻³)	Purity
Potassium hydroxide	KOH	--	56.10	2.044	85%
Hydrochloric Acid	HCl	--	36.47	1.18	35-37%
Potassium permanganate	KMnO ₄	--	158.03	1.01	99%
ferrous chloride	FeCl ₂ 4H ₂ O	--	198.75	3.16	99%
ferric chloride	FeCl ₃ 6H ₂ O	--	270.20	2.90	99%
Ethanol	C ₂ H ₆ O		46.07	789	99.5%
Acetonitrile	C ₂ H ₃ N		41.05	0.79	99.5%
Chloroacetic acid	C ₂ H ₃ ClO ₂		94.49	1.58	97%
1-Methylimidazole	C ₄ H ₆ N ₂		82.10	1.03	99%
Ammonium persulphate (APS)	(NH ₄) ₂ S ₂ O ₈		228.20	1.98	98%

All the reagents were purchased from Nacalai Tesque, Inc. (Kyoto, Japan) and used without further purification. And all solutions were prepared with distilled water.

2.1.2 Materials of electrochemical test

For electrochemical testing, stainless mesh (300 mesh) and nickel foam are chosen as the current collector. Before use, stainless mesh or nickel foam was trimmed to rectangular strips with 3×1 cm, after that the strips were immersed in ethanol with sonication for 1 h. Finally, the strips were dried under vacuum at 60 °C for 12 h. The polytetrafluoroethylene (PTFE) were used as the binder between active materials and current collector, and the acetylene black were chosen as the conductive agent for preparing the testing samples [3, 4].

2.2 Experimental methods

2.2.1 Preparation of KOH-activated biomass carbon (KWB) derived from sugarcane bagasse

KWB was obtained by KOH activation method and the typical process as follows: first, sugarcane bagasse was cut into small pieces (opening size approximately 2 mm) and washed with distilled water for 8 h at 90 °C, and then dried at 80 °C for 24 h. Second, 1 g cleanly sugarcane bagasse and 0.6 KOH were poured into 12 ml absolute ethanol with stirring and heated at 60 °C until all of the ethanol was evaporated, and then dried at 70 °C for 12 h. Third, the remnant mixture was pyrolyzed in a tubular furnace in N₂ atmosphere at 800 °C (heating rate is 10 °C min⁻¹) for 2 h. Finally, the obtained carbon material was washed by 1 M HCl solution and deionized water till the filtrate became neutral and collected after vacuum dry.

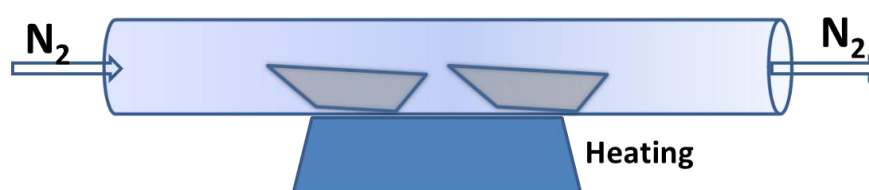


Fig. 2.4 The process of high temperature carbonization.

2.2.2 Preparation of MnO₂/KWB composites (KWBM)

The KWBM composites were prepared by directly reacting KMnO₄ with KWB. In a typical process, 0.05 g KMnO₄ dissolved in 100 ml deionized water, and then 0.1 g KWB (the mass ratio of KMnO₄/KWB is 0.5:1) added the above solution. Subsequently, the mixture was stirred under water bath at 70 °C until the color of solution changed from modena to tawny. The products removed from solution and washed with deionized water for several times, and dried in vacuum at 80 °C for 12 h to obtain of the KWBM-1 composite. The other products were denoted as KWBM-2, KWBM-3 and KWBM-4 for the mass ratio of KMnO₄/KWB is 1:1, 1.5:1 and 2:1, respectively.

2.2.3 Synthesis of 1-methyl-3-alkylcarboxylic acid imidazolium chloride ([CMMIm]Cl) ionic liquid

The [CMMIm]Cl was prepared as Fei reported [5]. In a typical fabrication of [CMMIm]Cl, 0.17 mol chloroacetic acid solid was added spoonful to 0.15 mol N-methylimidazole liquid with stirring in 1 h at 15-20 °C. When the mixed solution uniform, put it into the water bath kettle to heat up to 70 °C and run the reaction for 3-5 h. After that, the solution was used for suction filtration and washed the material with 30 ml of methyl cyanide for twice. Finally, the product was dried in vacuum at 40 °C for 12 h to obtain the white solid of [CMMIm]Cl.

2.2.4 Synthesis of pure PANI without IL

For composite with the PANI via [CMMIm]Cl brønsted acidic IL as dopant, the pure were prepared by the same method while using sulfamic acid (SA) as the dopant. Typically, 5 g SA dissolved in 100 ml deionized water, then 1 ml An monomer added the above solution. Subsequently, the mixture was ultrasonication for 0.5 h, and the APS solution (1.5 g APS dissolved in 10 ml of hydrochloric acid solution (1 M)) was by drop to the mixture to start the polymerization. The reaction was performed with stirring at room temperature for 2 h. Finally, the product was removed from solution,

washed with distilled water until pH=6-7, and dried in vacuum at 80 °C for 12 h to obtain the pure PANI as black green powder.

2.2.5 Preparation of polyaniline/biomass carbon composites (PANI/KWB)

The PANI/KWB composites were prepared by in-site polymerization method. 5 g [CMMIm]Cl IL dissolved in 100 ml deionized water. Then add 1 ml An monomer and 0.1 g KWB (the mass ratio of An/KWB is 10:1) to the above solution. Subsequently, the mixture was sonicated for 0.5 h, and the APS solution (1.5 g APS dissolved in 10 ml of hydrochloric acid solution (1 M)) was added drop by drop to the mixture to start the polymerization. The reaction was performed with stirring at room temperature for 2 h. Finally, the product was removed from solution, washed with distilled water until pH=6-7, and dried in vacuum at 80 °C for 12 h to obtain the PANI/KWB-1 as black green powder. The other products were denoted as PANI/KWB-2, PANI/KWB-3, PANI/KWB-4 and PANI/KWB-5 for the mass ratios of An/KWB was 20:1, 30:1, 40:1 and 50:1 (the mass ratio of An monomer to IL and APS was kept at 1:5:1.5), respectively. In addition, we also prepared pure PANI as control.

2.2.6 Preparation of Fe₃O₄/KWB composites (KBF_e)

KBF_e composites were prepared via a coprecipitation method. In a typical process, 0.24 g FeCl₃ · 6H₂O and 0.10 g FeCl₂ · 4H₂O (the molar ratio of Fe³⁺/Fe²⁺ is 1.8:1) were dissolved in 100 ml deionized water, and then 0.2 g KWB was added with a vigorous stirring for 10 min. Subsequently, the NaOH solution (1 M) was added drop by drop to the mixture until the pH value of mixture reached to 11. Then the mixture was heated at 90 °C for 1 h with a vigorous stirring. Finally, the product was removed from the mixture solution by suction and washed several times with deionized water. The black solid product was dried in vacuum at 80 °C for 12 h to obtain the KBF_e-1 composite (the theoretical value of mass ratio of Fe₃O₄ to KWB is 0.25:1). The other products were denoted as KBF_e-2, KBF_e-3, KBF_e-4 and KBF_e-5 for the theoretical value of mass ratio of Fe₃O₄ to KWB is 0.5:1, 0.75:1, 1:1 and 1.5:1, respectively.

2.3 Characterization

2.3.1 Morphological, structure, thermal and component characterizations

1) Scanning electron microscope (SEM)

The morphology and microstructure of samples were observed by scanning electron microscope (SEM, S-4300, Hitachi Co., Ltd., Tokyo, Japan). The sample was sputter-coated by gold with Ion sputter (E-1030, Hitachi Co., Ltd., Tokyo, Japan) for 2 min to provide enhanced conductivity. The test voltage was 5 KV or 15 KV, and an electric current was 10 μ A.

2) Transmission electron microscopy (TEM)

The morphologies of the samples were also observed using a transmission electron microscope (TEM, TF20, FEI, Co., Ltd., USA). For TEM observations, samples were dispersed in ethanol and then a small drop of the suspension was spread onto a 400 mesh copper grid. The chemical composition was investigated by energy-dispersive X-ray spectroscopy (EDX).

3) Fourier transforms infrared spectroscopy (FTIR)

The chemical structures of the samples were confirmed by Fourier transform infrared spectroscopy (FTIR, IRT-7000, JASCO, Japan) with the KBr pellet method. The wavelength range was between 4000 and 600 cm^{-1} , and the resolution was 4 cm^{-1} . Fifty scans were averaged for each sample.

4) X-ray diffraction (XRD)

The crystallographic structure of samples was tested by X-ray diffraction system (XRD, XRD-6000, Shimadzu Co., Ltd., Kyoto, Japan) in range of $2\theta = 5\sim 90^\circ$ by step scanning with a diffract meter. Nickel-filter Cu $K\alpha$ radiation ($\lambda=0.15417$ nm) was used

with a generator voltage of 40 kV and a current of 30 mA.

5) Nitrogen adsorption-desorption isotherms

The specific surface area and porosity of samples were proved using nitrogen adsorption-desorption isotherms which were performed by Brunauer-Emmett-Teller (BET) method of nitrogen sorption at 77 K using ASAP 2020 analyzer (Micromeritics, USA). All samples were outgassed under vacuum at 80 °C overnight prior to measurement. The specific surface area was calculated according to the Brunauer-Emmett-Teller (BET) equation, and the pore size distribution was derived from the adsorption branches of the isotherms.

6) X-ray photoelectron spectroscopy (XPS)

The chemical composition of samples was identified by X-ray photoelectron spectroscopy (PHI-5000, Perkin-Elmer Corp., USA) in a range of 0~1000 eV.

2.3.2 Electrochemical performance characterization

1) Preparation of working electrode

The fabrication of working electrodes was carried out as follows. For KWB materials, the sample, polytetrafluoroethylene (PTFE, the mass ratio of the sample and PTFE is 95:5), and ethanol, and grinding adequately to obtain a paste [6]. For KWBM, PANI/KWB, and KBF_e composites, the sample, acetylene black, PTFE (the mass ratio of the sample, acetylene black and PTFE is 80:15:5) and ethanol, and grinding adequately to obtain a paste [7, 8]. Then the paste was coated onto the stainless mesh or nickel foam, which was followed by drying under vacuum at 80 °C for 24 h and then compressed at 10 MPa for 5 min. The mass loading of active material in an electrode is about 8 mg.

2) Electrochemical tests

The electrochemical tests were measured with an electrochemical workstation (CHI 660D, Shanghai Chenhua, China; and Models 1287, Solartron Analytical, UK) in the three or two-electrode system in electrolyte. In three-electrode system, the sample test electrodes were used as working electrode, a saturated calomel electrolyte as the reference electrolyte, and a platinum-wire electrodes as counter electrolyte. Cyclic voltammetry (CV) and galvanostatic charge/discharge (GCD) were conducted in a potential window. Electrochemical impedance spectroscopy (EIS) was accomplished at open circuit potential with perturbation of 5 mV in the frequency range from 10^5 - 10^{-2} Hz. For asymmetric two-electrode system, the system was assembled with two test electrodes as working electrodes. The CV and GCD tests were tested at different voltage windows.

The standard calomel reference electrode (SCE) based on GCD curves was evaluated according to the following equation [9, 10] (Eq. 1):

$$C_m = \frac{I \cdot t}{\Delta V \cdot m} \quad (\text{Eq. 2.1})$$

where C_m (F g^{-1}) is the specific capacitance (SC), I (A) is discharge current, t (s) is the discharge time, ΔV (V) is the voltage window, and m (g) is the total mass of active material on working electrode in a two-electrode system or three-electrode system.

The energy density (E , Wh kg^{-1}) and power density (P , W kg^{-1}) of the asymmetric supercapacitors were calculated from the discharge curves according to the following equations [11, 12]:

$$E = \frac{1}{2} C_m (\Delta V)^2 \quad (\text{Eq. 2.2})$$

$$P = \frac{E}{t} \quad (\text{Eq. 2.3})$$

where C_m (F g^{-1}) is SC, t (h) is the discharge time, and ΔV (V) is the potential window from GCD curves of two-electrode system, respectively.

References

- [1] A. Pandey, C.R. Soccol, P. Nigam, V.T. Soccol, Biotechnological potential of agro-industrial residues. I: Sugarcane bagasse, *Bioresour. Technol.* 74 (2000) 69–80.
- [2] T. Welton, Room-Temperature Ionic Liquids. Solvents for Synthesis and Catalysis, *Chem. Rev.* 99 (1999) 2071–2083.
- [3] P. Yu, Z. Zhang, L. Zheng, F. Teng, L. Hu, X. Fang, A Novel Sustainable Flour Derived Hierarchical Nitrogen-Doped Porous Carbon/Polyaniline Electrode for Advanced Asymmetric Supercapacitors, *Adv. Energy Mater.* 6 (2016) 1–10.
- [4] X. Li, J. Shen, W. Sun, R.R.R. Wang, X. Hong, X. Zhao, X. Yan, R.R.R. Wang, X. Zhao, X. Yan, An asymmetric supercapacitor with super-high energy density based on 3D core-shell structured NiCo-layered double hydroxide@carbon nanotube and activated polyaniline-derived carbon electrodes with commercial level mass loading, *J. Mater. Chem. A.* 3 (2015) 13244–13253.
- [5] Z. Fei, D. Zhao, T.J. Geldbach, R. Scopelliti, P.J. Dyson, Brønsted acidic ionic liquids and their zwitterions: Synthesis, characterization and pKa determination, *Chem. - A Eur. J.* 10 (2004) 4886–4893.
- [6] J. Yan, T. Wei, B. Shao, F. Ma, Z. Fan, M. Zhang, C. Zheng, Y. Shang, W. Qian, F. Wei, Electrochemical properties of graphene nanosheet/carbon black composites as electrodes for supercapacitors, *Carbon N. Y.* 48 (2010) 1731–1737.
- [7] A. Elmouwahidi, Z. Zapata-Benabithé, F. Carrasco-Marín, C. Moreno-Castilla, Activated carbons from KOH-activation of argan (*Argania spinosa*) seed shells as supercapacitor electrodes, *Bioresour. Technol.* 111 (2012) 185–190.
- [8] T. Tsubota, K. Takenaka, N. Murakami, T. Ohno, Performance of nitrogen- and sulfur-containing carbon material derived from thiourea and formaldehyde as electrochemical capacitor, *J. Power Sources.* 196 (2011) 10455–10460.
- [9] W. Fan, C. Zhang, W.W. Tjiu, K.P. Pramoda, C. He, T. Liu, Graphene-Wrapped Polyaniline Hollow Spheres As Novel Hybrid Electrode Materials for Supercapacitor Applications, *ACS Appl. Mater. Interfaces.* 5 (2013) 3382–3391.
- [10] P. C. Chen, G. Shen, Y. Shi, H. Chen, C. Zhou, Preparation and Characterization of

Flexible Asymmetric Supercapacitors Based on Transition-Metal-Oxide Nanowire/Single-Walled Carbon Nanotube Hybrid Thin-Film Electrodes, *ACS Nano*. 4 (2010) 4403–4411.

[11]L. Wu, L. Hao, B. Pang, G. Wang, Y. Zhang, X. Li, MnO₂ nanoflowers and polyaniline nanoribbons grown on hybrid graphene/Ni 3D scaffolds by in situ electrochemical techniques for high-performance asymmetric supercapacitors, *J. Mater. Chem. A*. 5 (2017) 4629–4637.

[12]H. Gao, F. Xiao, C.B. Ching, H. Duan, High-Performance Asymmetric Supercapacitor Based on Graphene Hydrogel and Nanostructured MnO₂, *ACS Appl. Mater. Interfaces*. 4 (2012) 2801–2810.

Chapter 3 Biocarbon from sugarcane bagasse with superior performance in supercapacitors

3.1 Introduction

Since entering the 21st century, because of the exhausted fossil resource and population growth, energy shortage and environmental crisis become increasingly serious. This phenomenon propels people to find novel energy materials that can be commercialized in the near future, as well as the produce of materials are facile, environmentally friendly, low-cost, and nontoxic routes [1, 2]. Amongst various materials, carbon materials, especially structural carbon materials have attracted more and more attention of scholars, due to its potential applications in catalyst supports, adsorbents, carbon fixation, electrode, carbon fuel cells, cell biology, and gas storage [3-7]. Recently, with the rapid growth of nanotechnology, nanostructured carbon materials, such as carbon nanotubes (CNTs), graphene and porous carbons have been developed, all of them have the advantage of high surface area, electrical conductivity, chemical stability, fast energy storage-releasing, which are suitable as electrode materials to apply in supercapacitors and battery [8-10].

Supercapacitors is a new energy storage devices with considerable promise for a wide range of applications, including uninterruptable power sources, portable electronics, braking systems and hybrid electric vehicles [11-13]. According to the distinguishing energy storage mechanism, supercapacitors can be classified to electrical double-layer capacitors (EDLC) and pseudocapacitors. The EDLC is based on charge separation at the electrode/electrolyte interface, whereas the latter is based on redox reaction occurring within the active materials [14-17]. Currently, carbon-based EDLC materials are the most employed electrode material for commercially available supercapacitors due to their good cycle lifetime and high maximum [3, 18, 19].

At present, some important carbon materials also achieved high specific capacitance (Cs) and energy density, such as templated carbon [20], graphene [21] and carbon nanotube [22]. However, most of methods to prepare of the above carbon materials often require complicated preparation conditions or special facilities, leading to the high cost [23]. Therefore, a new research hotspot for preparation of high performance carbon materials are using cheap raw materials and simple method [24]. Recently, more and more scholars concentrate on the method of direct pyrolysis, as well as used the biomass or biowaste as carbon precursors [25, 26]. By virtue of low cost, renewability, availability, and environmental friendliness, make biomass become ideal candidates for producing structure carbon material with good capacitive performance [27, 28]. Many biocarbon have been prepared, such as pine cones [29], bamboo [30], waste coffee [31], oil palm [32] and so on. Sugarcane bagasse is a kind of typical biomass waste, which sometimes being processed by incineration or direct disposal. Obviously, this way not only wasted its use value, but also brought secondary pollution [32]. The discarded sugarcane bagasse waste residue is rich in lignin and cellulose, it can be used as the carbon source to make structure carbon. This is an efficient way to utilize sugarcane bagasse resources.

Hence, in this work, we report a simple method for preparation biocarbon (KWB) as the electrode materials for supercapacitors. KWB was obtained by direct pyrolysis of sugarcane bagasse after pretreatment by potassium hydroxide (KOH). The carbonization temperature and the mass ratio of KOH to sugarcane bagasse were researched as the influencing factors. We found that the two factors had a profound effect on the specific surface area of KWB, and further affect their electrochemical performance. The highest specific capacitance of KWB-3-800 reached 196.3 F g^{-1} at a current density of 1 A g^{-1} , and this ensures KWB-3-800 can be used as high performance supercapacitors electrodes.

3.2 Experimental

3.2.1 Materials

Sugarcane bagasse was crushed by family-use grinder before use. The other reagents, such as ethanol, potassium hydroxide (KOH), and hydrochloric acid (HCl), all were purchased from Nacalai Tesque, Inc. (Kyoto, Japan) and of analytical grade, were used without further purification.

3.2.2 Preparation of KOH-activated biocarbon (KWB) derived from sugarcane bagasse

KWB was obtained by the KOH activation method and the typical process as follows: first, sugarcane bagasse was cut into small pieces (opening size approximately 2 mm) and washed with distilled water for 8 h at 90 °C, after that rinsed 2-3 times with deionized water and filtered, and then dried at the 80 °C for 24 h. Second, 1 g cleanly sugarcane bagasse and 0.5 g KOH were poured into 12 ml absolute ethanol with stirring and heated at 60 °C until all of the ethanol was evaporated, and then dried at 70 °C for 12 h. Third, the remnant mixture was pyrolyzed in a tubular furnace in N₂ atmosphere at 600 °C (heating rate is 10 °C min⁻¹) for 2 h. Finally, the obtained carbon material was washed by 1 M HCl solution for 2h, after that rinsed several times with deionized water till the filtrate became neutral and filtered, as well as collected after vacuum dry at the 40 °C for 12 h.

The carbonization temperature and the mass ratio of KOH to sugarcane bagasse were researched as the influencing factors. Firstly, the products with different mass ratio of KOH to sugarcane bagasse were prepared at 800 °C, and denoted as KWB-1, KWB-2, KWB-3, KWB-4, and KWB-5 for the mass ratio of KOH to sugarcane bagasse is 0.2:1.0, 0.4:1, 0.6:1, 0.8:1, and 1:1, respectively. For comparison, the biocarbon without KOH activated was also prepared, which was denoted KWB-0. After that, on the basis of the best mass ratio of KOH to sugarcane bagasse, the different carbonation temperature was researched. The products was denoted as KWB-3-600, KWB-3-700,

KWB-3-800, and KWB-3-900 for the carbonization temperature is 600, 700, 800, and 900 °C, respectively.

Table 3.1 the preparation condition of KWB

Samples	Mass ratio of KOH to bagasse	Carbonization temperature (°C)
KWB-0	0:1	800
KWB-1	0.2:1	800
KWB-2	0.4:1	800
KWB-3	0.6:1	800
KWB-4	0.8:1	800
KWB-5	1:1	800
KWB-3-600	0.6:1	600
KWB-3-700	0.6:1	700
KWB-3-800	0.6:1	800
KWB-3-900	0.6:1	900

3.2.3 Structure characterization

The morphology and microstructure of samples were observed by scanning electron microscopy (SEM) at S-4300 SEM instrument (Hitachi, Japan). The specific surface areas of the samples were determined by Brunauer-Emmett-Teller (BET) method of nitrogen sorption at 77 K using ASAP 2020 analyzer (Micromeritics, USA). The crystallographic structure was carried out via X-ray diffraction (XRD) measurements at XRD-6000 instrument (Shimadzu, Japan) with Cu-K α radiation ($\lambda=0.154$ nm) at a speed of 5° min⁻¹ from $2\theta = 5^\circ$ to 90°. The surface states of samples were analyzed via X-ray photoelectron spectroscopy (XPS) using a PHI Quantum 5000 instrument (ULVAC-PHI, Japan) equipped with Al K α radiation source.

3.2.4 Electrochemical testing

Conventional three-electrolyte system and asymmetric two-electrode system were used in supercapacitors to measure the electrochemical characterization of KWB using Models 1287 electrochemical workstations (Solartron Analytical, UK). The test

electrodes were first prepared by mixing the KWB with Polytetrafluoroethylene (PTFE) at a mass ratio of 95:5, and ethanol, then the mixing were adequately ground to obtain a homogeneous paste for coating onto the stainless mesh to forming a current collector. After that, the test electrodes were dried in vacuum at 80 °C for 24 h, then compressed at 10 MPa for 5 min. In three-electrode system, the KWB test electrodes was used as working electrode, a saturated calomel electrolyte as the reference electrolyte, and a platinum-wire electrodes as counter electrolyte. Cyclic voltammetry (CV) and galvanostatic charge/discharge (GCD) were conducted in a potential window from -0.4 to 0 V for KWB. Electrochemical impedance spectroscopy (EIS) was accomplished at open circuit potential with perturbation of 5 mV in the frequency range from 10^5 - 10^2 Hz. A 1M H₂SO₄ solution was used as an electrolyte for all electrochemical measurements.

The standard calomel reference electrode (SCE) based on GCD curves was evaluated according to the following equation [33, 34] (Eq. 1):

$$C_m = (I \cdot t) / (\Delta V \cdot m) \quad (\text{Eq. 1})$$

where C_m (F g⁻¹) is the specific capacitance (SC), I (A) is discharge current, t (s) is the discharge time, ΔV (V) is the voltage window, and m (g) is the total mass of active material on working electrode in three-electrode system.

3.3 Results and discussion

3.3.1 Microstructural characterization

Fig. 3.1 illustrates the preparation process of KWB frameworks. At first, the KWB was obtained by carbonized and activated sugarcane bagasse at one step (as shown in Fig. 4.1a) [35]. As shown in Fig. 4.1b, the sugarcane bagasse exhibited a typical bundle-microtube-like structure of the biological tissue. While after carbonization and activation, the special structure was destroyed and an allium-giganteum-like structure with high interconnected frameworks which is favorable for the ion diffusion and suitable for preparation of carbon-based composites, can be clearly found in the as-

resulted KWB (as shown in Fig. 4.1e and f) [36]. The process of KOH activating carbon at high temperature be researched by some scholars [37, 38].

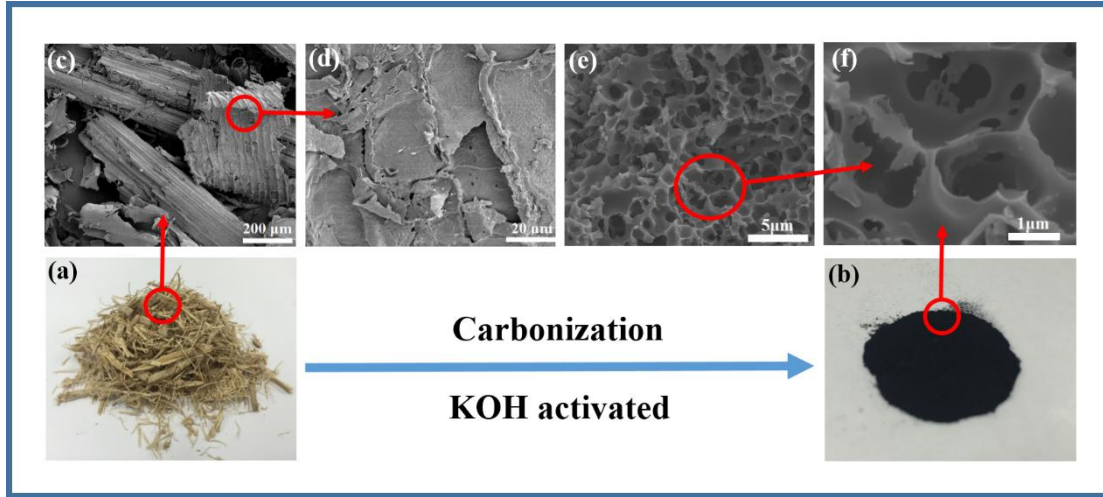
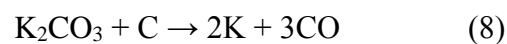
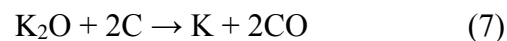
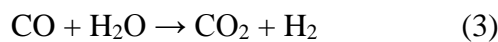
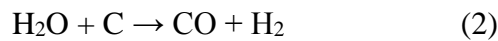
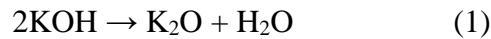


Fig. 3.1 Schematic illustration of the preparation process of KWB samples. Digital photographs of sugarcane bagasse (a), KWB (b); SEM images with different magnification of the sugarcane bagasse (c and d), and KWB (e and f).

In short, this process through three aspects: firstly, the formation of H_2O and CO_2 can contribute to porosity development by carbon gasification; then, the formation of K_2O and K_2CO_3 can etch the carbon framework by redox reactions, which is beneficial to form the pore structure; finally, the formation of metallic K is an important factor for developing the pore structure by inserting into the graphitic layers. What's more, the reaction occurring between KOH and the carbon materials are as follows [39]:



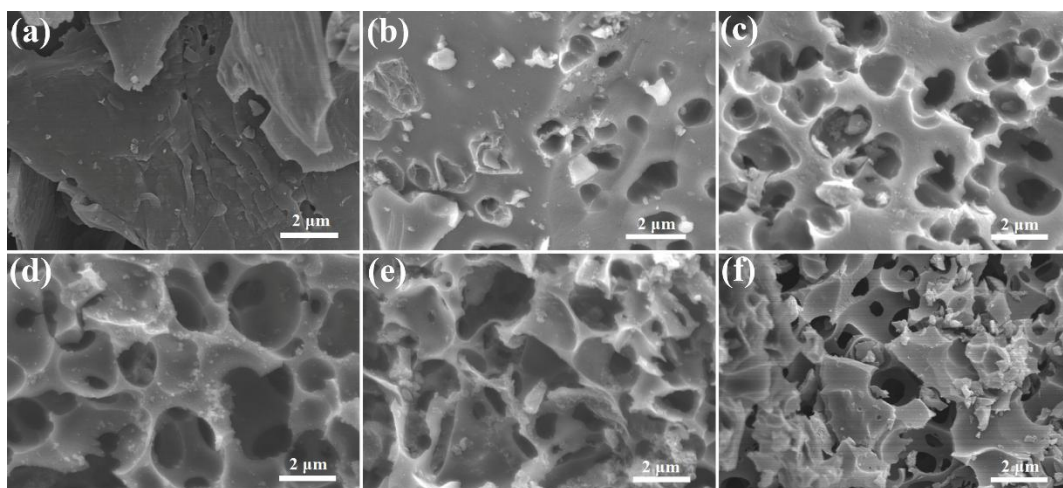


Fig. 3.2 SEM images of KWB-0 (a), KWB-1 (b), KWB-2 (c), KWB-3 (d), KWB-4 (e) and KWB-5 (f) samples.

The morphology and microstructure of the prepared KWB samples were investigated by SEM, and Fig. 3.2 shows the samples with different mass ratios of KOH/bagasse at 800 °C. The KWB-0 is the sample without KOH activating, and it can be clearly seen that the surface of KWB-0 is smooth without porous (as shown in Fig. 3a). However, the other KWB samples including from KWB-1 to KWB-5, all of them with a lot of porous on the surface can be clearly observed. Moreover, it is noteworthy that the mass ratio of KOH/bagasse has an important increasing the porous' morphology and number is very different. When the mass ratio of KOH/bagasse less than 0.6:1, the number and diameter of the surface porous increase with the increase of the mass ratio. For KWB-1 (Fig.3.2 (b)), there are only a little of porous with the diameter at 1 μ m on the surface, while KWB-2 (Fig.3.2 (c)) can be directly observed the more porous with larger diameter than the porous structure of KWB-1. Furthermore, a large number of secondary porous with a diameter of about 0.5 μ m are present on the inner wall of the primary porous having a diameter of 2 mm, it means that KOH pretreatment makes KWB forming hierarchically porous structure biocarbon material with interconnected frameworks. When the mass ratio of KOH/bagasse more than 0.6:1, the excessive activation of KOH destroyed the interconnected frameworks structure of biocarbon material. For KWB-5 (Fig.3.2 (f)) the mass ratio of KOH/bagasse is 1:1, the surface of the primary porous of carbon skeleton has been completely collapsed, and only could

see a lot of debris and secondary porous with the diameter at 0.5 secondary hole. In summary, the SEM image of KWB samples shows the important influence of the mass ratio of KOH/bagasse for KWB samples, and KWB-3 (Fig.3.2 (d)) shows the perfect interconnected frameworks structure with multi-stage porous, which means the best activated degree of KOH activation agent is the mass ratio of KOH/bagasse at 0.6:1. In addition, the structure of carbon material may profoundly impact electrochemical performance of KWB samples.

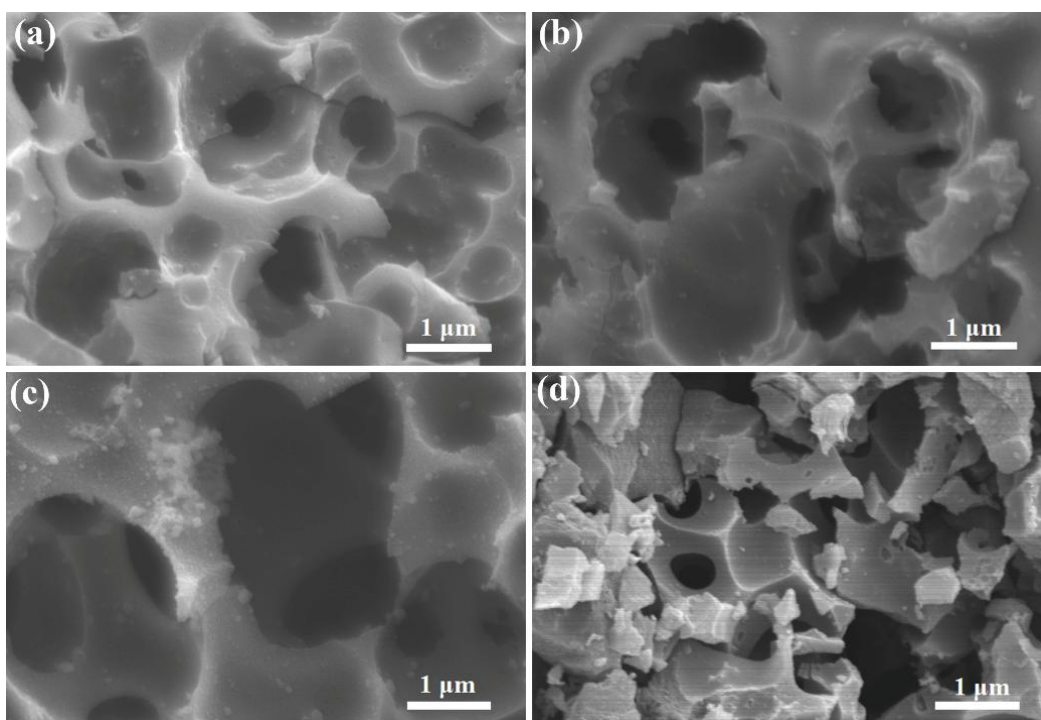


Fig. 3.3 SEM images of KWB-3-600 (a), KWB-3-700 (b), KWB-3-800 (c), KWB-3-900 (d), samples.

The morphology of KWB samples with different carbonization temperature were also investigated by SEM. All the KWB samples have a lot of porous on the surface of samples, while the porous structures have a little different. It can be clearly observed that follow the increasing of carbonization temperature the diameter and number of porous were increasing, and KWB-3-800 shown the excellent interconnected frameworks structure with multi-stage porous at the 800 °C of carbonization temperature. In addition, the interconnected frameworks structure of KWB-3-900

shown more serious damaged, that may be due to the too high temperature to preserve the multi-stage porous. Hence, the best carbonization temperature of sugarcane bagasse is 800 °C, and the above phenomena may impact electrochemical performance of KWB samples profoundly.

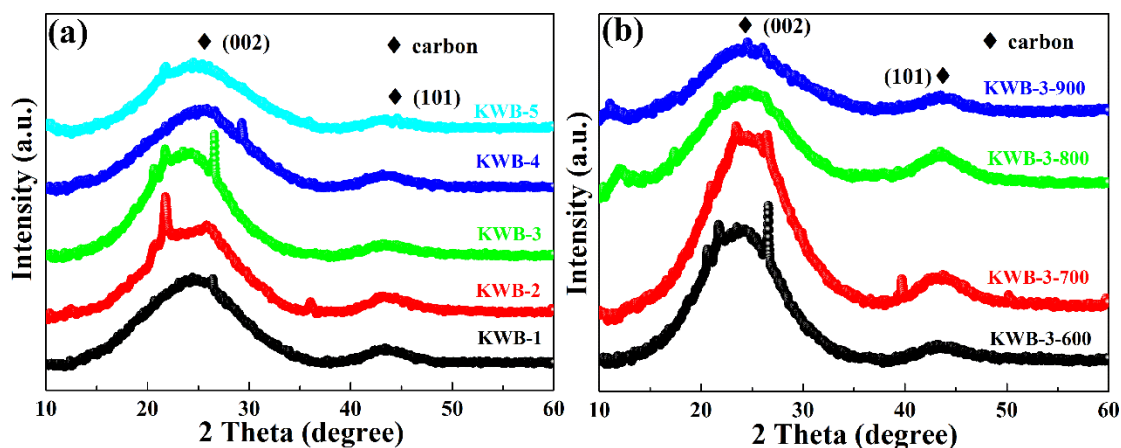


Fig. 3.4 X-ray diffraction patterns of the prepared KWB-1, KWB-2, KWB-3, KWB-4 and KWB-5 samples (a), and KWB-3-600, KWB-3-700, KWB-3-800, and KWB-3-900 samples.

The crystallinity of the samples was examined by X-ray diffraction analysis. Fig. 3.4 shows the XRD patterns of KWB samples. All of KWB samples can be observed two diffraction peaks. A broad diffraction peak centered at 25° correspond to the (002) plane of graphite, indicating the amorphous nature [36]. Additionally, a weak diffraction peak centered at 43.4° can be attributed to the (101) plane of graphite, which means of the complete transformation of sugarcane bagasse to another kind of activated carbon [40]. However, every patterns have a little different. In Fig. 3.4(a), the intensity of board peak at 25° decreased following the increasing of mass ratio of KOH/bagasse, and same effect also appeared with the increasing of carbonization temperature. This phenomenon may be due to the reducing concentration of nonparallel single layers carbon when more activation agent or higher carbonization temperature roles in the raw materials [38].

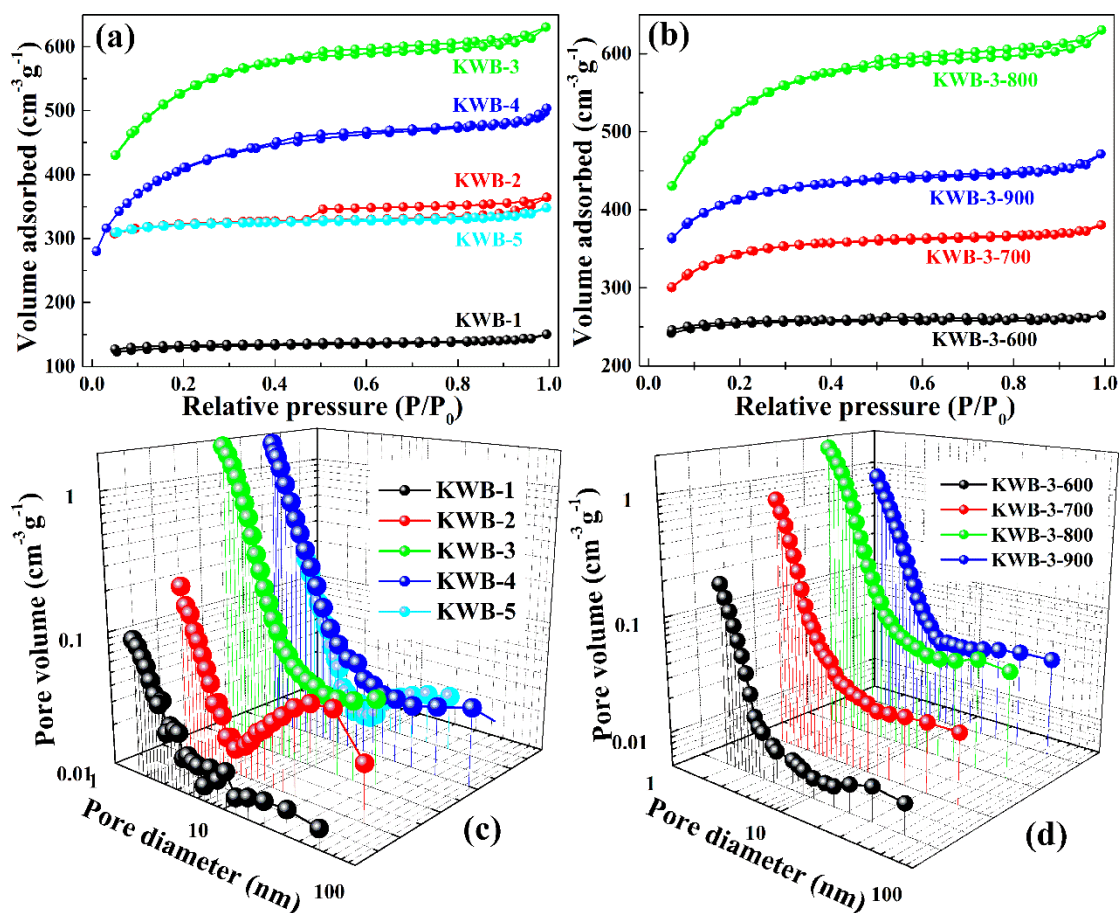


Fig. 3.5 N_2 adsorption-desorption isotherms (a, and b) and pore size distribution by BJH method (c, and d) of the prepared KWB-1, KWB-2, KWB-3, KWB-4, KWB-5, KWB-3-600, KWB-3-700, KWB-3-800, and KWB-3-900 samples.

As we all know that the surface area and the pore-size distribution are the two key factors for the electrochemical performance of electrode materials. The specific surface area and pore-size distribution of KWB samples were characterized by nitrogen adsorption/desorption measurements (as shown in Fig. 4.6a, b, c, and d). It is clear that the all KWB shows the typical combined I/IV type sorption isotherms, indicating the polyporous structure [41]. However, the KWB-3-800 shows the best volume absorbed and pore volume, due to the presence of more nanoscale porous than other KWB samples (Fig. 3.5d). As given in Table 2, the S_{BET} of KWB-3-800 is up to $1717.91 \text{ m}^2 \text{ g}^{-1}$, which results in KWB-3-800 provides more reaction sites for efficient electrochemical interactions/reactions. What's more, it also can be used as carbon-based material for preparing composite materials.

Table 3.2 Specific surface area, pore size of KWB samples. (S_{BET} - the specific surface area; P - the average pore size; V_t - the total pore volume)

Sample	S_{BET} (m ² g ⁻¹)	V_t (cm ³ g ⁻¹)	P (nm)
KWB-1	396.62	0.232	4.67
KWB-2	997.27	0.564	4.23
KWB-3	1717.91	0.975	2.58
KWB-4	1433.06	0.755	3.03
KWB-5	991.90	0.539	4.22
KWB-3-600	784.55	0.409	2.71
KWB-3-700	1079.07	0.588	2.63
KWB-3-800	1717.91	0.975	2.58
KWB-3-900	1303.74	0.729	2.85

Moreover, the specific surface area and pore distribution of KWB samples can be controlled by adjust the mass ratio of KOH/bagasse and carbonization temperature. As shown in Table 3.2, the specific surface area and pore volume of KWB was significantly increased firstly and then decreased with the mass ratio of KOH/bagasse increased, and during the change of carbonization shown the similar trend. On the contrary, the average pore size of KWB was significantly decreased firstly and then increased with the mass ratio of KOH/bagasse and carbonization temperature increased. This result further confirms that excessive activation of KOH may further react with graphite crystallite structure around the pore, leading to excessive burn-off of carbon surface, which will result in breakage in porous carbon structure, and thereby both surface area and pore volume decrease substantially [42]. On the other hand, the carbonization temperature also plays a vital role in determining the BET surface area, but excess higher temperature may destroy the already formed interconnected frameworks structure and reduce the specific surface area of the material, which would reduce the relative area that can actually participate in the electrochemical reaction and has an effect on the electrochemical performance of this material as electrode material in applied. Overall, at optimum mass ratio of KOH/bagasse and carbonization temperature, the BET surface area is of maximum, which is achieved at 0.6:1 and carbonization at 800 °C. What's

more, this result is also confirmed with SEM.

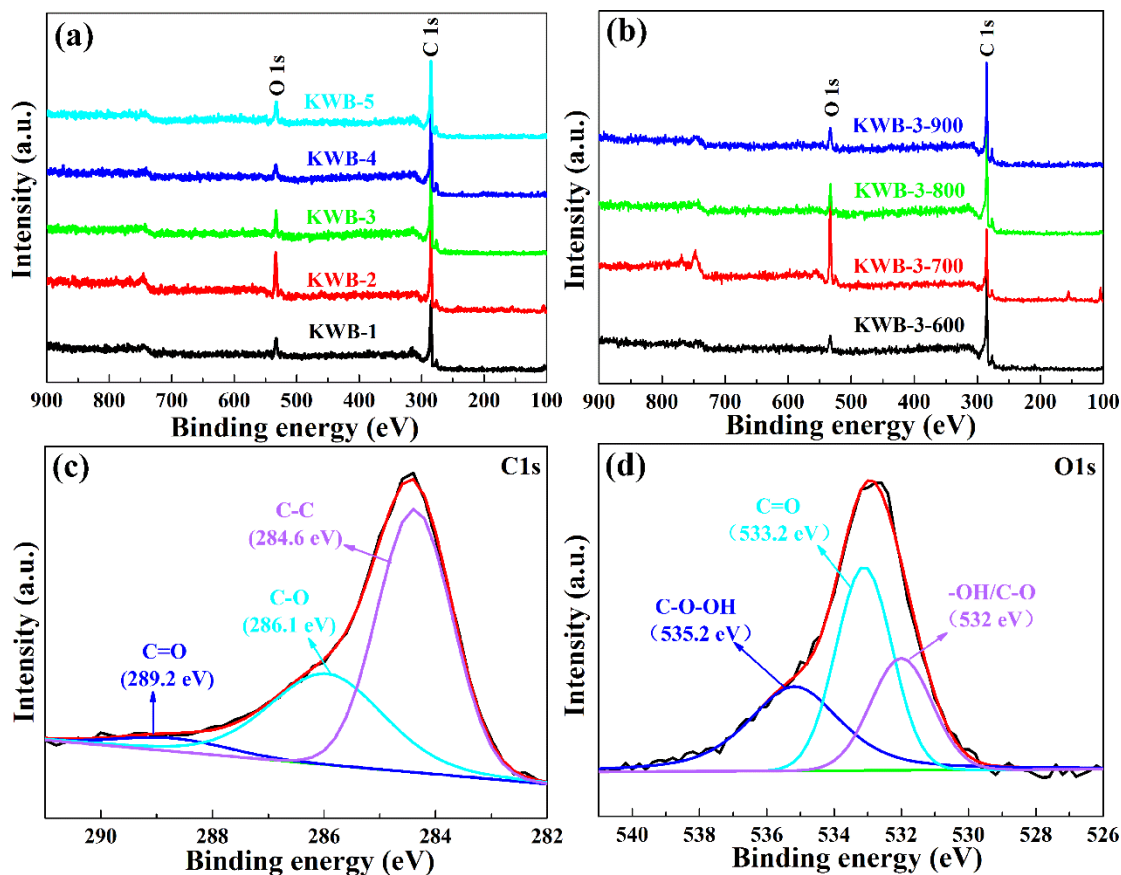


Fig. 3.6 XPS survey spectra of KWB-1, KWB-2, KWB-3, KWB-4 and KWB-5 samples (a), KWB-3-600, KWB-3-700, KWB-3-800, and KWB-3-900 samples (b); high resolution C1s (c) and O1s (e) XPS spectra of KWB-3-800 sample.

The information of the surface chemical composition of samples was obtained from XPS spectra. The full scan spectra of samples are shown in Fig. 4.6a and b. All of the KWB have the signal of C and O element at the around of 535 and 284 eV. More information about the change of surface chemistry has been obtained by the deconvoluted high-resolution XPS spectra of three regions (C, and O as shown in Fig. 4.6c and d). The C1s spectra of KWB-3-800 could be deconvoluted into three peaks (as shown in Fig. 5.8c) with binding energies of 531.5, 533.2 and 534.8 eV. These peaks could be assigned to aromatic or other sp²-hybridised carbon atoms bound to neighboring carbon atoms (C-C, 284.4 eV), carbon in C-O (285.8 eV) and C=O (288.8 eV), respectively [43]. The O1s spectra of KWB-3-800 in Fig. 4.6d can be deconvoluted

into three components. The peaks of 531.5, 533.2 and 534.8 eV can be assigned to –OH/C-O, C=O and C-O-OH groups, respectively [44].

Table 3.3 XPS spectrum analysis of samples

Sample	C at. %	O at. %
KWB-1	89.63	10.37
KWB-2	89.88	10.02
KWB-3	90.95	9.05
KWB-4	91.89	8.11
KWB-5	88.87	11.13
KWB-3-600	92.33	7.67
KWB-3-700	89.59	10.41
KWB-3-800	90.95	9.05
KWB-3-900	88.95	11.05

The content of elements of every KWB samples are listed in Table 3.3. It is easy to find that all the KWB samples have approximately 10% of oxygen elements. These oxygen elements are mainly derived from cellulose, hemicellulose and lignin in bagasse, which are not involved in the activation reaction under high temperature, and formed C-O or C=O band with adjacent carbon elements. Many of published literatures have demonstrate that the addition of heteroatoms can significantly reduce the resistance of charge transfer. On the other hand, carbonaceous materials are evidenced to reduce the pathway for the electron transfer from active electrode materials to the electrolyte and facilitate fast diffusion of electrolyte ions [27, 45, 46]. The above phenomena may impact electrochemical performance of KWB samples profoundly.

3.3.2 Electrochemical performance of KWB samples

In order to evaluate the electrochemical characteristics of KWB samples, CV, GCD, and EIS measurements were employed to characterize the capacitive properties in 1 M H₂SO₄ aqueous solution in a three-electrode configuration. Fig. 3.7 shows the CV curves of KWB samples for different mass ratio of KOH/bagasse (Fig. 3.7a) and

different carbonization temperature (Fig. 3.7b) at a scan rate of 0.01 V s^{-1} . The CV curve of all KWB samples shows nearly symmetric rectangular shape, indicating an ideal double-layer [47]. The offset from the standard rectangle is attributed to the reaction of a small amount of oxygen-containing groups in the material [45]. Obviously, the area enclosed by the CV curve, which is proportional to the capacitance, increases firstly and then decreased with the increase of the mass ratio of KOH/bagasse and carbonization temperature. However, KWB-3-800 shows the larger area enclosed by the CV curve than that of the KWB samples, revealing the highest SC.

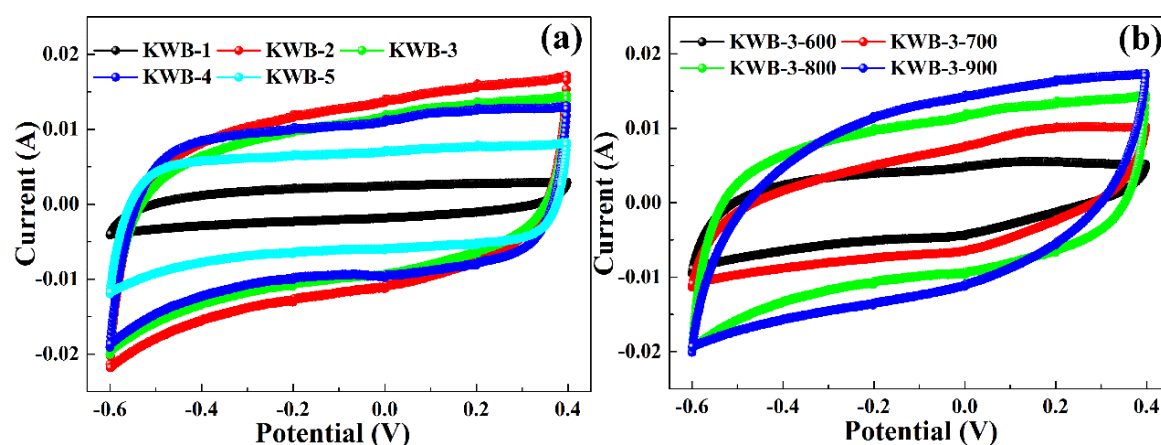


Fig. 3.7 CV curves of KWB-1, KWB-2, KWB-3, KWB-4 and KWB-5 samples (a), KWB-3-600, KWB-3-700, KWB-3-800, and KWB-3-900 samples (b).

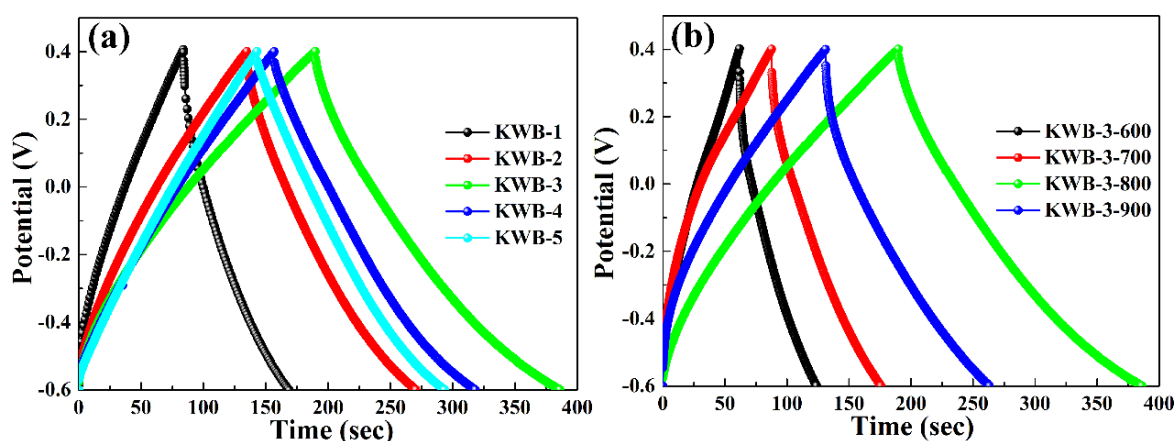


Fig. 3.8 CV curves of KWB-1, KWB-2, KWB-3, KWB-4 and KWB-5 samples (a), KWB-3-600, KWB-3-700, KWB-3-800, and KWB-3-900 samples (b).

The electrochemical performance of as-prepared samples was further analyzed by the GCD method and the results are shown in Fig. 3.8. The discharge time of KWB-3-800 is markedly longer than those of other samples, suggesting that the KWB-3-800 possesses further more excellent electrochemical capacitive performance than the other samples. We can get the specific capacitance by these curves [48]. From Eq. 3.1, the specific capacitances of KWB-1, KWB-2, KWB-3, KWB-4, KWB-5, KWB-3-600, KWB-3-700, KWB-3-800, and KWB-3-900 are 85, 135.6, 196.3, 161.4, 150.4, 62.2, 88.1, 196.3 and 132.1 F g^{-1} , respectively, at a current density is 1 A g^{-1} .

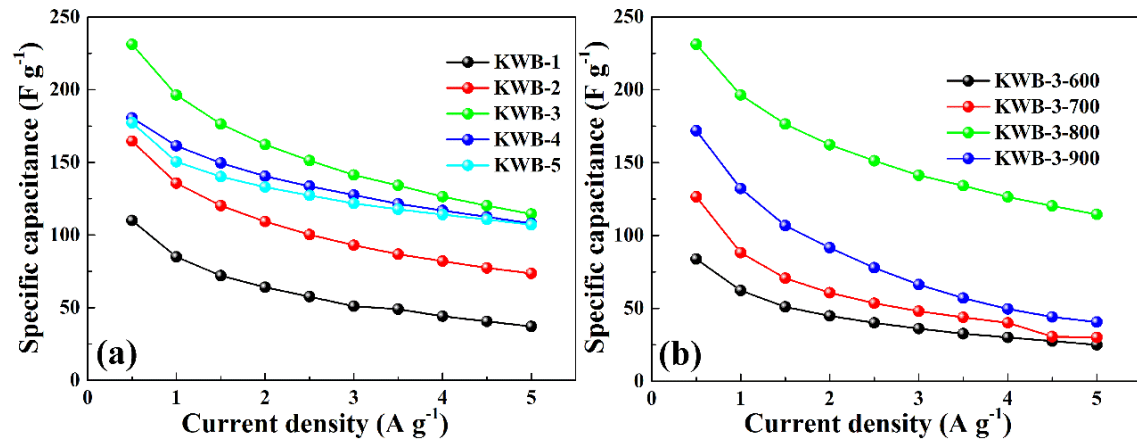


Fig. 3.9 Specific capacitance versus current density of KWB-1, KWB-2, KWB-3, KWB-4 and KWB-5 samples (a), KWB-3-600, KWB-3-700, KWB-3-800, and KWB-3-900 samples (b).

Furthermore, the SC of KWB (as shown in Fig. 3.9) increases first and then decreases with the increase of the mass ratio of KOH/bagasse and carbonization temperature. These results are in accordance with those deduced from CV curves. Furthermore, more interesting is that in the KWB samples, it appears a sudden potential drop (IR drop), and the IR drop increases with the increase of KOH/bagasse mass ratio. This can be attributed to the resistance of electrolyte and the inner resistance of ion diffusion in hierarchically porous carbon [49, 50].

To further study the capacitive behavior samples, EIS was used to measure the charge transport and ion diffusion. The Nyquist plots of KWB samples are showed in Fig. 3.9.

In EIS curve, the internal resistance (R_s , including the intrinsic resistance of the sample, the contact resistance between the sample and current collector, and the resistance of bulk electrolyte) can be obtained from the point intersecting with the real axis in the region of high frequency. The semicircle is due to the charge transfer and which will affect capacitive behavior at high current loading [51]. The inset shows that R_s of KWB-1, KWB-2, KWB-3, KWB-4, KWB-5, KWB-3-600, KWB-3-700, KWB-3-800, and KWB-3-900 are 1.30, 1.12, 0.70, 1.35, 1.60, 1.67, 1.19, 0.70 and 1.34 Ω , respectively. It is worth noting that R_s of KWB-3-800 is lower than those of KWB samples. The semicircle radius of KWB-3-800 is lower than the other samples, means that the KWB-3-800 possesses the lowest charge resistance among KWB samples. Moreover, the nearly vertical line at lower frequency of KWB-3-800 indicates the pure capacitor behavior as an ideal capacitor [46, 47]. In short, the analyses of EIS reveal that KWB-3-800 sample possesses an excellent capacitive performance, and this result agrees with the analyses of GCD and CV.

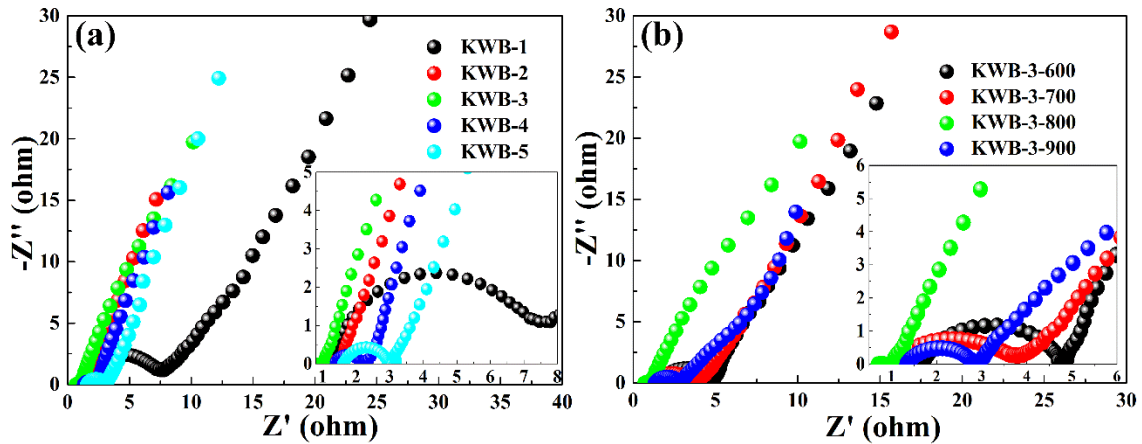


Fig. 3.10 EIS curves of KWB-1, KWB-2, KWB-3, KWB-4 and KWB-5 samples (a), KWB-3-600, KWB-3-700, KWB-3-800, and KWB-3-900 samples (b).

Fig. 3.11a shows the CV curves of KWB-3-800 samples at different scan rates ranging from 10 to 50 mV s^{-1} . Generally, the response current of KWB-3-800 gradually increases when increasing the scan rate. The CV curve has maintained the rectangular shape, and a rapid current response on voltage reversal at each end potential at the scan

rates ranging from 10 to 50 mV s⁻¹. These reveal its good electrochemical capacitive performance at high scan rates. Also note that, the pair of weak peaks were also clearly observe at the scan rate of 50 mV s⁻¹, which may be because oxygen-groups still participate in the reaction under high current, indicating that the material has good stability. Fig. 3.11b shows the specific capacitances of KWB-3-800 at different current densities from 0.5 to 10 A g⁻¹. Clearly, the downward trend of specific capacitance of KWB-3-800 is nonlinear, which suggests that the pseudocapacitive behavior happens at the electrode-electrolyte interface [52]. From Eq. 3.1, the specific capacitances reach 196.3 and 123 F g⁻¹ at the current density of 1 and 15 A g⁻¹, respectively, and the capacitance retention of KWB-3-800 is 62.7 %. These results indicate that the KWB-3-800 possesses the fast charge-discharge properties, which is very important for supercapacitors application.

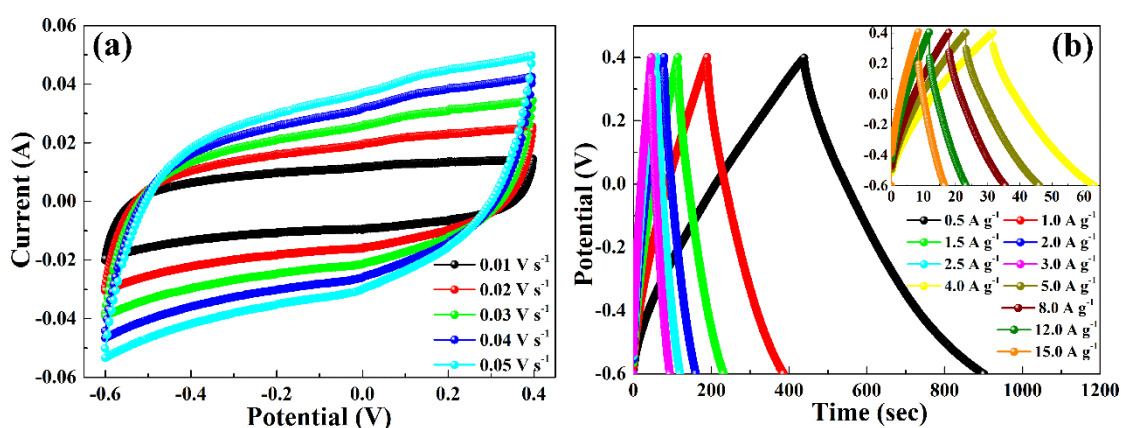


Fig. 3.11 CV curves of KWB-3-800 at different scan rates from 10 to 50 mVs⁻¹ (a); GCD curves of KWB-3-800 at different current density from 0.5 to 10 A g⁻¹(b)

3.4 Conclusions

In summary, a simple method for preparation KWB as the electrode materials for supercapacitors. KWB was obtained by direct pyrolysis of sugarcane bagasse after pretreatment by potassium hydroxide (KOH). The electrochemical performance of KWB was closely related to the mass ratio of KOH/bagasse and carbonization temperature. KWB-3-800 showed the best electrochemical performance when the mass

ratio of KOH/bagasse was 0.6 and the carbonization temperature is 800 °C in three-electrode system. In addition, the specific capacitances reach 196.3 and 123 F g⁻¹ at the current density of 1 and 15 A g⁻¹, respectively, and the capacitance retention of KWB-3-800 is 62.7 %. The preparation of KWB samples with a facile and low-cost method shows an excellent electrochemical performance, marking it a promising candidate in energy storage devices.

Reference

- [1] H. Li, Y. Gong, C. Fu, H. Zhou, W. Yang, M. Guo, M. Li, Y. Kuang, A novel method to prepare a nanotubes@mesoporous carbon composite material based on waste biomass and its electrochemical performance, *J. Mater. Chem. A*. 5 (2017) 3875–3887.
- [2] B. Hu, K. Wang, L. Wu, S.H. Yu, M. Antonietti, M.M. Titirici, Engineering carbon materials from the hydrothermal carbonization process of biomass, *Adv. Mater.* 22 (2010) 813–828.
- [3] Y. Zhai, Y. Dou, D. Zhao, P.F. Fulvio, R.T. Mayes, S. Dai, Carbon materials for chemical capacitive energy storage, *Adv. Mater.* 23 (2011) 4828–4850.
- [4] S.H. Ahn, X. Yu, A. Manthiram, “Wiring” Fe-N_x-Embedded Porous Carbon Framework onto 1D Nanotubes for Efficient Oxygen Reduction Reaction in Alkaline and Acidic Media, *Adv. Mater.* 29 (2017) 1606534.
- [5] X. Wu, W. Jia, Biomass-derived multifunctional magnetite carbon aerogel nanocomposites for recyclable sequestration of ionizable aromatic organic pollutants, *Chem. Eng. J.* 245 (2014) 210–216.
- [6] A. Cappetto, W.J. Cao, J.F. Luo, M. Hagen, D. Adams, A. Shelikeri, K. Xu, J.P. Zheng, Performance of wide temperature range electrolytes for Li-Ion capacitor pouch cells, *J. Power Sources*. 359 (2017) 205–214.
- [7] C. W. Huang, C. H. Hsu, P. L. Kuo, C. T. Hsieh, H. Teng, Mesoporous carbon spheres grafted with carbon nanofibers for high-rate electric double layer capacitors, *Carbon N. Y.* 49 (2011) 895–903.
- [8] Q. Cheng, J. Tang, N. Shinya, L. C. Qin, Polyaniline modified graphene and carbon nanotube composite electrode for asymmetric supercapacitors of high energy density, *J. Power Sources*. 241 (2013) 423–428.
- [9] S.R.S. Prabaharan, R. Vimala, Z. Zainal, Nanostructured mesoporous carbon as electrodes for supercapacitors, *J. Power Sources*. 161 (2006) 730–736.
- [10] Y. Liu, J. Liu, M. Hou, L. Fan, Y. Wang, Y. Xia, Carbon-coated Li₄Ti₅O₁₂ nanoparticles with high electrochemical performance as anode material in sodium-

- ion batteries, *J. Mater. Chem. A*. 5 (2017) 10902–10908.
- [11] M.B. Sassin, C.N. Chervin, D.R. Rolison, J.W. Long, Redox deposition of nanoscale metal oxides on carbon for next-generation electrochemical capacitors, *Acc. Chem. Res.* 46 (2013) 1062–1074.
- [12] G. Nagaraju, S.M. Cha, J.S. Yu, Ultrathin nickel hydroxide nanosheet arrays grafted like porous carbon with improved electrochemical performance as a supercapacitive material, *Nat. Publ. Gr.* (2017) 1–11.
- [13] G. Yu, L. Hu, M. Vosgueritchian, H. Wang, X. Xie, J.R. McDonough, X. Cui, Y. Cui, Z. Bao, Solution-Processed Graphene/MnO₂ Nanostructured Textiles for High-Performance Electrochemical Capacitors, *Nano Lett.* 11 (2011) 2905–2911.
- [14] M.Y. HO, P.S. KHIEW, D. ISA, T.K. TAN, W.S. CHIU, C.H. CHIA, a Review of Metal Oxide Composite Electrode Materials for Electrochemical Capacitors, *Nano.* 9 (2014) 1430002.
- [15] A. Vu, X. Li, J. Phillips, A. Han, W.H. Smyrl, P. Bühlmann, A. Stein, Three-dimensionally ordered mesoporous (3DOM) carbon materials as electrodes for electrochemical double-layer capacitors with ionic liquid electrolytes, *Chem. Mater.* 25 (2013) 4137–4148.
- [16] V. Kumar, P.S. Lee, Redox Active Polyaniline-h-MoO₃ Hollow Nanorods for Improved Pseudocapacitive Performance, *J. Phys. Chem. C*. 119 (2015) 9041–9049.
- [17] S. Dhibar, P. Bhattacharya, G. Hatui, S. Sahoo, C.K. Das, Transition Metal-Doped Polyaniline/Single-Walled Carbon Nanotubes Nanocomposites: Efficient Electrode Material for High Performance Supercapacitors, *ACS Sustain. Chem. Eng.* 2 (2014) 1114–1127.
- [18] A. Ghosh, Y.H. Lee, Carbon-based electrochemical capacitors, *ChemSusChem*. 5 (2012) 480–499.
- [19] M. Inagaki, H. Konno, O. Tanaike, Carbon materials for electrochemical capacitors, *J. Power Sources*. 195 (2010) 7880–7903.
- [20] H. Nishihara, T. Kyotani, Templated nanocarbons for energy storage, *Adv. Mater.* 24 (2012) 4473–4498.
- [21] M. Liu, Y.-E. Miao, C. Zhang, W.W. Tjiu, Z. Yang, H. Peng, T. Liu, Hierarchical

- composites of polyaniline–graphene nanoribbons–carbon nanotubes as electrode materials in all-solid-state supercapacitors, *Nanoscale*. 5 (2013) 7312.
- [22] H. Liu, Y. Zhang, R. Li, X. Sun, S. D é silets, H. Abou-Rachid, M. Jaidann, L.S. Lussier, Structural and morphological control of aligned nitrogen-doped carbon nanotubes, *Carbon N. Y.* 48 (2010) 1498–1507.
- [23] H. Chen, D. Liu, Z. Shen, B. Bao, S. Zhao, L. Wu, Functional Biomass Carbons with Hierarchical Porous Structure for Supercapacitor Electrode Materials, *Electrochim. Acta*. 180 (2015) 241–251.
- [24] L.L. Zhang, X.S. Zhao, Carbon-based materials as supercapacitor electrodes, *Chem. Soc. Rev.* 38 (2009) 2520-2531.
- [25] S. Dutta, A. Bhaumik, K.C.-W. Wu, Hierarchically porous carbon derived from polymers and biomass: effect of interconnected pores on energy applications, *Energy Environ. Sci.* 7 (2014) 3574–3592.
- [26] J.M. Valente Nabais, J.G. Teixeira, I. Almeida, Development of easy made low cost bindless monolithic electrodes from biomass with controlled properties to be used as electrochemical capacitors, *Bioresour. Technol.* 102 (2011) 2781–2787.
- [27] T. Wei, X. Wei, Y. Gao, H. Li, Large scale production of biomass-derived nitrogen-doped porous carbon materials for supercapacitors, *Electrochim. Acta*. 169 (2015) 186–194.
- [28] Y. Qu, Z. Zhang, X. Zhang, G. Ren, Y. Lai, Y. Liu, J. Li, Highly ordered nitrogen-rich mesoporous carbon derived from biomass waste for high-performance lithium-sulfur batteries, *Carbon N. Y.* 84 (2015) 399–408.
- [29] N. Manyala, A. Bello, F. Barzegar, A.A. Khaleed, D.Y. Momodu, J.K. Dangbegnon, Coniferous pine biomass : A novel insight into sustainable carbon materials for supercapacitors electrode, *Mater. Chem. Phys.* (2016) 1–9.
- [30] W. Chen, H. Yang, Y. Chen, X. Chen, Y. Fang, H. Chen, Biomass pyrolysis for nitrogen-containing liquid chemicals and nitrogen-doped carbon materials, *J. Anal. Appl. Pyrolysis*. 120 (2016) 186–193.
- [31] H. Jang, J.D. Ocon, S. Lee, J.K. Lee, J. Lee, Direct power generation from waste coffee grounds in a biomass fuel cell, *J. Power Sources*. 296 (2015) 433–439.

- [32]N.H. Basri, M. Deraman, S. Kanwal, I.A. Talib, J.G. Manjunatha, A.A. Aziz, R. Farma, Supercapacitors using binderless composite monolith electrodes from carbon nanotubes and pre-carbonized biomass residues, *Biomass and Bioenergy*. 59 (2013) 370–379.
- [33]N.I.T. Ramli, S. Abdul Rashid, Y. Sulaiman, M.S. Mamat, S.A. Mohd Zobir, S. Krishnan, Physicochemical and electrochemical properties of carbon nanotube/graphite nanofiber hybrid nanocomposites for supercapacitor, *J. Power Sources*. 328 (2016) 195–202.
- [34]J.E. Zuliani, J.N. Caguiat, D.W. Kirk, C.Q. Jia, Considerations for consistent characterization of electrochemical double-layer capacitor performance, *J. Power Sources*. 290 (2015) 136–143.
- [35]Z. Zheng, Q. Gao, Hierarchical porous carbons prepared by an easy one-step carbonization and activation of phenol-formaldehyde resins with high performance for supercapacitors, *J. Power Sources*. 196 (2011) 1615–1619.
- [36]H. Feng, H. Hu, H. Dong, Y. Xiao, Y. Cai, B. Lei, Y. Liu, M. Zheng, Hierarchical structured carbon derived from bagasse wastes: A simple and efficient synthesis route and its improved electrochemical properties for high-performance supercapacitors, *J. Power Sources*. 302 (2016) 164–173.
- [37]J. Wang, S. Kaskel, KOH activation of carbon-based materials for energy storage, *J. Mater. Chem*. 22 (2012) 23710-23725.
- [38]H. Wang, Q. Gao, J. Hu, High Hydrogen Storage Capacity of Porous Carbons Prepared by Using Activated Carbon, (2009) 7016–7022.
- [39]B. Wang, J. Qiu, H. Feng, E. Sakai, T. Komiyama, KOH-activated nitrogen doped porous carbon nanowires with superior performance in supercapacitors, *Electrochim. Acta*. 190 (2016) 229–239.
- [40]B. Wang, J. Qiu, H. Feng, E. Sakai, T. Komiyama, Nitrogen doped carbon nanowires prepared from polypyrrole nanowires for potential application in supercapacitors, *J. Electroanal. Chem*. 775 (2016) 219–227.
- [41]K.S.W. Sing, Reporting physisorption data for gas/solid systems with special reference to the determination of surface area and porosity (Recommendations

- 1984), *Pure Appl. Chem.* 57 (1985).
- [42] J. Pu, C. Li, L. Tang, T. Li, L. Ling, K. Zhang, Y. Xu, Q. Li, Y. Yao, Impregnation assisted synthesis of 3D nitrogen-doped porous carbon with high capacitance, *Carbon N. Y.* 94 (2015) 650–660.
- [43] W. Liu, K. Tian, Y. He, H. Jiang, H. Yu, High-Yield Harvest of Nano fibers/Mesoporous Carbon Composite by Pyrolysis of Waste Biomass and Its Application for High Durability Electrochemical Energy Storage, *Environ. Sci. Technol.* 48 (2014) 13951–13959.
- [44] X. Tang, R. Jia, T. Zhai, H. Xia, Hierarchical Fe₃O₄@Fe₂O₃ Core–Shell Nanorod Arrays as High-Performance Anodes for Asymmetric Supercapacitors, *ACS Appl. Mater. Interfaces.* 7 (2015) 27518–27525.
- [45] Z. Zapata-Benabithé, F. Carrasco-Marín, C. Moreno-Castilla, Preparation, surface characteristics, and electrochemical double-layer capacitance of KOH-activated carbon aerogels and their O- and N-doped derivatives, *J. Power Sources.* 219 (2012) 80–88.
- [46] X. Zhang, L. Ma, M. Gan, G. Fu, M. Jin, Y. Lei, P. Yang, M. Yan, Fabrication of 3D lawn-shaped N-doped porous carbon matrix/polyaniline nanocomposite as the electrode material for supercapacitors, *J. Power Sources.* 340 (2017) 22–31.
- [47] A.E. Ismanto, S. Wang, F.E. Soetaredjo, S. Ismadji, Preparation of capacitor's electrode from cassava peel waste, *Bioresour. Technol.* 101 (2010) 3534–3540.
- [48] W. Yu, H. Wang, S. Liu, N. Mao, X. Liu, J. Shi, W. Liu, S. Chen, X. Wang, N, O-codoped hierarchical porous carbons derived from algae for high-capacity supercapacitors and battery anodes, *J. Mater. Chem. A.* 4 (2016) 5973–5983.
- [49] D. Liu, C. Fu, N. Zhang, H. Zhou, Y. Kuang, Three-Dimensional Porous Nitrogen doped Graphene Hydrogel for High Energy Density supercapacitors, *Electrochim. Acta.* 213 (2016) 291–297.
- [50] W. Li, D. Chen, Z. Li, Y. Shi, Y. Wan, G. Wang, Z. Jiang, D. Zhao, Nitrogen-containing carbon spheres with very large uniform mesopores: The superior electrode materials for EDLC in organic electrolyte, *Carbon N. Y.* 45 (2007) 1757–1763.

- [51]T. Cai, M. Zhou, D. Ren, G. Han, S. Guan, Highly ordered mesoporous phenol-formaldehyde carbon as supercapacitor electrode material, *J. Power Sources*. 231 (2013) 197–202.
- [52]L. Hou, L. Lian, D. Li, G. Pang, J. Li, X. Zhang, S. Xiong, C. Yuan, Mesoporous N-containing carbon nanosheets towards high-performance electrochemical capacitors, *Carbon N. Y.* 64 (2013) 141–149.

Chapter 4 Manganese dioxide/ biocarbon composites with superior performance in supercapacitors

4.1 Introduction

Supercapacitors, is one of the most promising energy storage devices with fast charge-discharge rates, superior power density and long cycle lifetime compared to the other chemical energy storage devices [1, 2]. According to the energy storage mechanism, supercapacitors are classified as electrical double-layer capacitors (EDLC) and pseudocapacitors. The EDLC is based on charge separation at the electrode/electrolyte interface, whereas the latter is based on redox reaction occurring within the active materials [3-5]. Currently, carbon materials are often used for EDLC due to their high electrical conductivity and fast energy storage-releasing, while the transition metal oxides often used for pseudocapacitors because of multiple oxidation states at the charge-discharge process [6, 7].

Among the multifarious transform metal oxides, MnO_2 is one of the most promising electrode materials for low cost, high theoretical capacity and environmental friendly supercapacitors devices [8]. However, the performances of single-phased MnO_2 are still insufficient to meet growing demands in supercapacitors due to its intrinsic properties, such as low conductivity and poor mechanical stability [9, 10]. To solve these problems, one-dimensional (1D) nanostructure MnO_2 (such as nanosheets MnO_2) has been found to be good candidate for its low density and excellent permeation [11, 12]. Nevertheless, 1D MnO_2 still does not achieve the desired electrochemical performance due to its electrochemical dissolution during cycling [13]. Therefore, development of new type MnO_2 materials to meet the desired electrochemical performance is urgently desirable.

To respond the above requirement, carbon materials have been select as a component for preparing MnO_2 -based composites to effectively improve electrochemical

performance [14]. At present, many kinds of carbon materials, such as activated carbon (AC) [15], graphene [16] and carbon nanotube [17] are often used as the carbon content in MnO₂-based composites because their high surface area, excellent electronic conductivity, unique internal structure and superior thermal stability [18]. However, most of methods for prepare of the above carbon materials often require complicated preparation conditions or special facilities, leading to the high cost [19]. For example, as a rising star of graphene, it is often obtained by reduction of graphene oxide (rGO), and graphene oxide (GO) often obtained from natural graphite by Hummers method [20]. The method is a complex process, and contains four steps: preoxidation, further oxidation, decomposition of excessive oxidant and removed metal ions [21]. Therefore, one preponderant method of preparation of carbon materials is direct pyrolysis of carbon precursors, such as pyrolysis of biomass or biowaste [22]. This method has been noticed by many researchers, and many biocarbon derived from biomass such as corncobs [23], cocoons [24] and watermelon rind [25] have been prepared. All the biocarbon materials described above present high specific surface area and abundant pore structure. Therefore, the biocarbon materials are very suitable for preparation of MnO₂-based composites.

Hence, in this work, we report an efficient method for preparation of MnO₂/biocarbon composites (KWBM) as the electrode materials for supercapacitors. The biocarbon (KWB) was obtained by direct pyrolysis of sugarcane bagasse, and then the KWBM was obtained by redox reaction between KMnO₄ and KWB under different mass ratios of KMnO₄/KWB. We found that the chemical component and specific surface area of KWBM had a profound effect on electrochemical performance of KWBM. In addition, an asymmetric two-electrode system was fabricated by employing KWBM-4 and KWB as positive and negative electrode, respectively. We also found that the asymmetric system possessed the high energy density and high cycle stability.

4.2 Experimental

4.2.1 Materials

Sugarcane bagasse was crushed by family-use grinder before use. The other reagents, such as ethanol, potassium hydroxide (KOH), hydrochloric acid (HCl) and potassium permanganate (KMnO₄), all were purchased from Nacalai Tesque, Inc. (Kyoto, Japan) and of analytical grade, were used without further purification.

4.2.2 Preparation of KOH-activated biocarbon (KWB) derived from sugarcane bagasse

KWB was obtained by KOH activation method and the typical process as follows: first, sugarcane bagasse was cut into small pieces (opening size approximately 2 mm) and washed with distilled water for 8 h at 90 °C, and then dried at 80 °C for 24 h. Second, 1 g cleanly sugarcane bagasse and 0.6 g KOH were poured into 12 ml absolute ethanol with stirring and heated at 60 °C until all of the ethanol was evaporated, and then dried at 70 °C for 12 h. Third, the remnant mixture was pyrolyzed in a tubular furnace in N₂ atmosphere at 800 °C (heating rate is 10 °C min⁻¹) for 2 h. Finally, the obtained carbon material was washed by 1 M HCl solution and deionized water till the filtrate became neutral and collected after vacuum dry.

4.2.3 Preparation of MnO₂/KWB composites (KWBM)

The KWBM composites were prepared by directly reacting KMnO₄ with KWB. In a typical process, 0.05 g KMnO₄ dissolved in 100 ml deionized water, and then 0.1 g KWB (the mass ratio of KMnO₄/KWB is 0.5:1) added the above solution. Subsequently, the mixture was stirred under water bath at 70 °C until the color of solution changed from modena to tawny. The products removed from solution and washed with deionized water for several times, and dried in vacuum at 80 °C for 12 h to obtain of the KWBM-1 composite. The other products were denoted as KWBM-2, KWBM-3 and KWBM-4

for the mass ratio of KMnO_4/KWB is 1:1, 1.5:1 and 2:1, respectively.

4.2.4 Structure characterization

The morphology of samples were observed by transmission electron microscopy (TEM, H-8110, Hitachi Co., Ltd. Tokyo, Japan) and scanning electron microscopy (SEM, S-4300, Hitachi Co., Ltd. Tokyo, Japan). Nitrogen adsorption-desorption isotherms were measured at $-196\text{ }^\circ\text{C}$ on a Micromeritics ASAP 2020 apparatus. The specific surface area was calculated according to the Brunauer-Emmett-Teller (BET) equation. All samples were outgassed under vacuum at $80\text{ }^\circ\text{C}$ overnight prior to measurement. The crystallographic structure of the samples was observed by X-ray diffraction (XRD, XRD-6000, Shimadzu Co., Ltd. Kyoto, Japan) equipped with $\text{Cu K}\alpha$ radiation. X-ray photoelectron spectroscopy (XPS) analysis was performed on the PHI Quantum 5000 equipped with an $\text{Al K}\alpha$ radiation source.

4.2.5 Electrochemical test

The electrochemical tests were measured with an electrochemical workstation (CHI 660D, Shanghai Chenhua, China) in the two or three-electrode system in 1M KOH electrolyte. For three-electrode system, saturated calomel electrolyte and platinum-wire electrode were used as reference and counter electrode, respectively. The test electrodes were first prepared by mixing the KWB and polytetrafluoroethylene (PTFE) at a mass ratio of 95:5, and mixing KWBM with carbon black (CB) and PTFE at a mass ratio of 80:15:5. After that, the mixing were grinding adequately to obtained a homogeneous paste, that was coated onto the Ni foam for current collector and dried under vacuum at $80\text{ }^\circ\text{C}$ for 24 h, and then compressed at 10 MPa for 5 min. Cyclic voltammetry (CV), and galvanostatic charge/discharge (GCD) were conducted in a potential window from -0.8 to 0 V for KWB biocarbon, and 0 to 0.7 V for KWBM composites respectively. Electrochemical impedance spectroscopy (EIS) was carried out in the frequency range from 10^5 to 10^{-2} Hz at open circuit potential with as ac perturbation of 5 mV. The symmetric two-electrode system was assembled with two almost identical working

electrodes (the active material was KWBM-4 composites sample, and the counter electrode was KWB biocarbon sample). The CV and GCD tests were run at different voltage windows.

The standard calomel reference electrode (SCE) based on GCD curves was evaluated according to the following equation (Eq. 1):

$$C_m = (I \times t) / (\Delta V \times m) \quad (\text{Eq. 1})$$

where I is discharge current (A), t is the discharge time (s), ΔV is the voltage window (V), and m is the mass of active material on working electrode in three-electrode system, in two-electrode system is the total mass of active material on two working electrodes [26].

4.3 Results and discussion

4.3.1 Microstructural characterization

Fig. 4.1 illustrates the preparation process of KWB frameworks and KWBM composites. At first, the KWB was obtained by carbonized and activated sugarcane bagasse at one step (as shown in Fig. 4.1a) [3]. As shown in Fig. 4.1d and e, the sugarcane bagasse exhibited a typical bundle-microtube-like structure of the biological

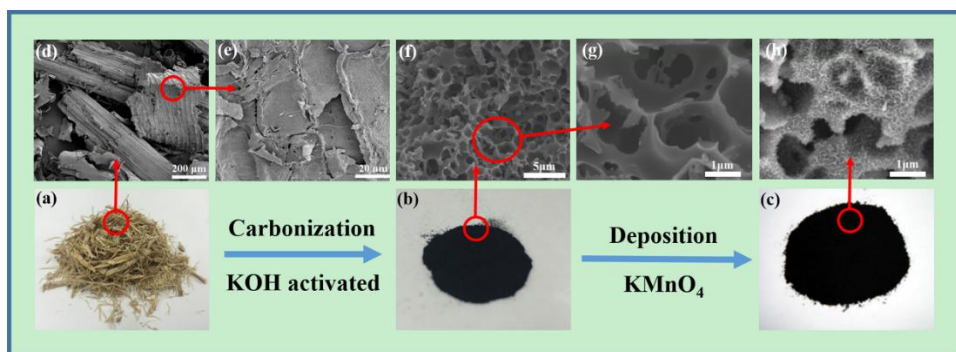


Fig. 4.1 Schematic illustration of the preparation process of KWBM composites. Digital photographs of sugarcane bagasse (a), KWB (b) and KWBM-3 (c). SEM images with different magnification of the sugarcane bagasse (d and e), KWB (f and g) and KWBM-3 composite (h).

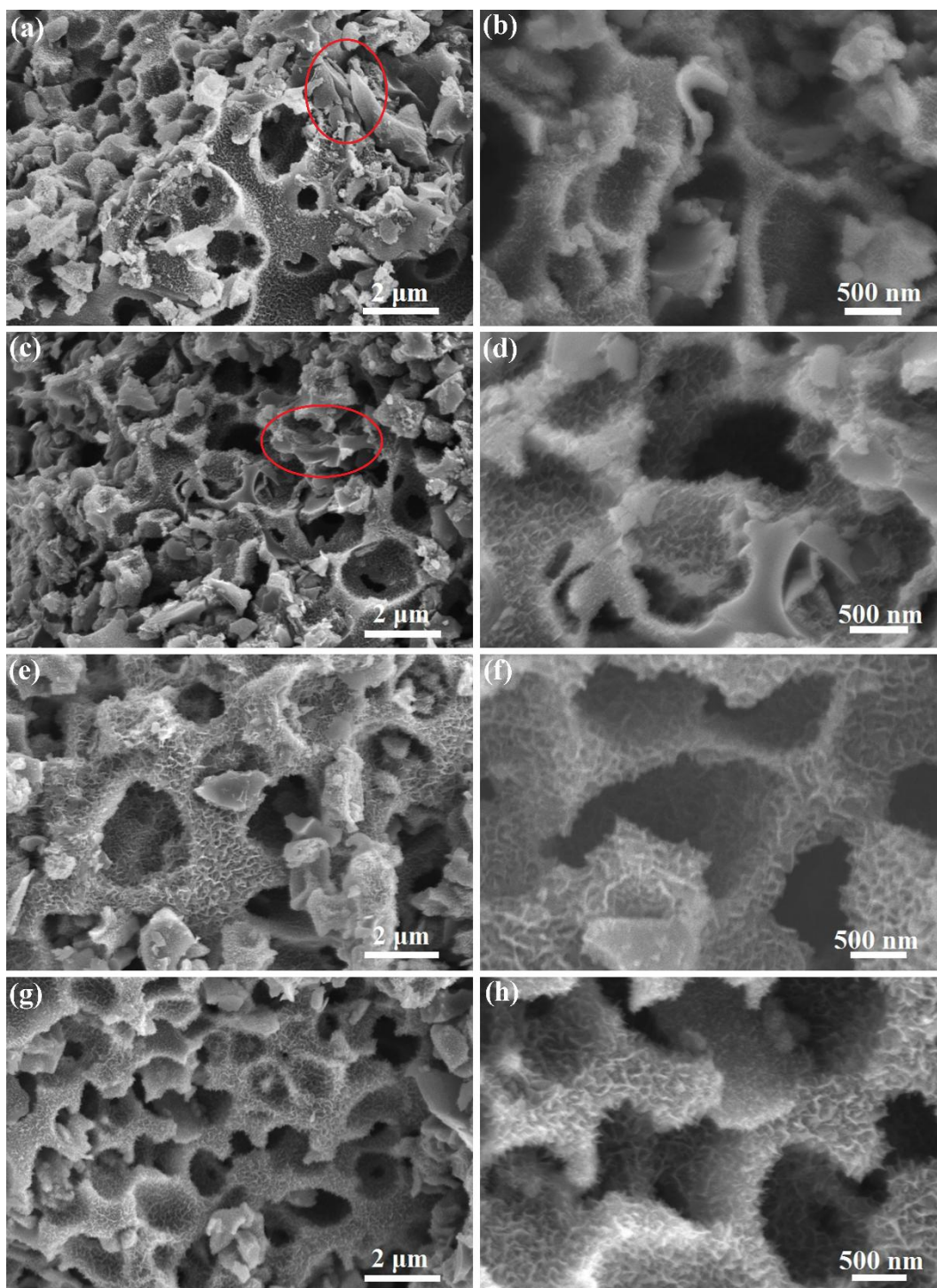
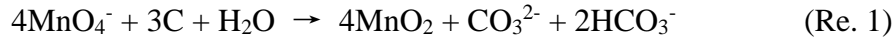


Fig. 4.2 SEM images of KWBM-1(a, b), KWBM-2(c, d), KWBM-3(e, f) and KWBM-4(g, h) composites.

tissue. While after carbonization and activation, the special structure was destroyed and an allium-giganteum-like structure with high interconnected frameworks which is favorable for the ion diffusion and suitable for preparation of MnO₂-based composites

[27], can be clearly found in the as-resulted KWB (as shown in Fig. 4.1f and g). Therefore, KWB was used as both scaffolds and reducing agents for MnO₂ growth in this study. MnO₂ nanosheets grew on the surface of KWB based on the self-limiting reaction (Re. 1) between KMnO₄ and KWB in neutral aqueous solution [28, 29].



The morphology and microstructure of the prepared KWBM composites are shown in Fig. 4.2. The surface and interconnected frameworks of KWBM were coated by MnO₂ nanosheets in all samples. Moreover, it is noteworthy that a little of uncoated KWB was observed in the red circle of Fig. 4.2a (KWBM-1) and c (KWBM-2). The uncoated KWB gradually decreased with the mass ratio of KMnO₄/KWB increased till, KWB was completely coated by MnO₂ nanosheets when the mass ratio of KMnO₄/KWB is 2 (as shown in Fig. 4.2g). In addition, the high resolution SEM image of samples (Fig. 4.2b, d, f and h) showed the size of MnO₂ nanosheets gradually increased with the mass ratio of KMnO₄/KWB increased. The above phenomena may impact electrochemical performance of KWBM composites profoundly.

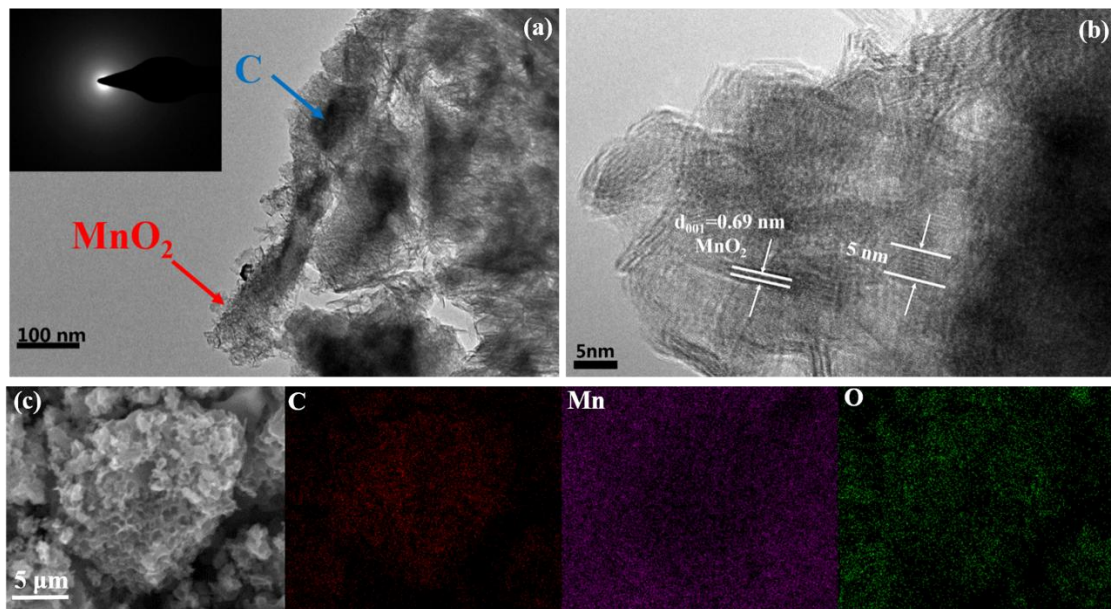


Fig. 4.3 TEM images of the KWBM-4 composite (a, b); the inset in a shows the corresponding SAED pattern taken from the edge of MnO₂ nanosheets; HRTEM image of the birnessite-type MnO₂ nanosheets (b); the EDX mapping images of the KWBM-4 composite (c).

The morphology of KWBM-4 can be further investigated by TEM. It can be clearly seen that the surface of KWB is coated by MnO₂ nanosheets (as shown in Fig. 4.3a). In addition, the nanosheets of MnO₂ structure is confirmed by HRTEM image (as shown in Fig. 4.3b). The interplanar spacing of MnO₂ nanosheets is 0.69 nm, corresponding to the typical interplanar spacing of the (001) plane of δ -MnO₂ which prefers forming sheet structures [28]. Fig. 4.3c is the energy-dispersive X-ray (EDX) mapping results of KWBM-4. The results reveal the co-existence and homogenous distribution of C, Mn and O across the core-shell nanostructure of KWBM-4. Moreover, the EDX mappings of other KWBM composites are showed in Fig. 4.4, and the chemical composition of KWBM can be obtained by EDX analysis (as shown in Table 4.1). For KWBM composites, the content of C and O gradually decreased and increased, respectively, with the mass ratio of KMnO₄/KWB increased. The ratio of Mn and C content also increased with the mass ratio of KMnO₄/KWB increased. The chemical composition of samples will be further analyzed by XPS spectra.

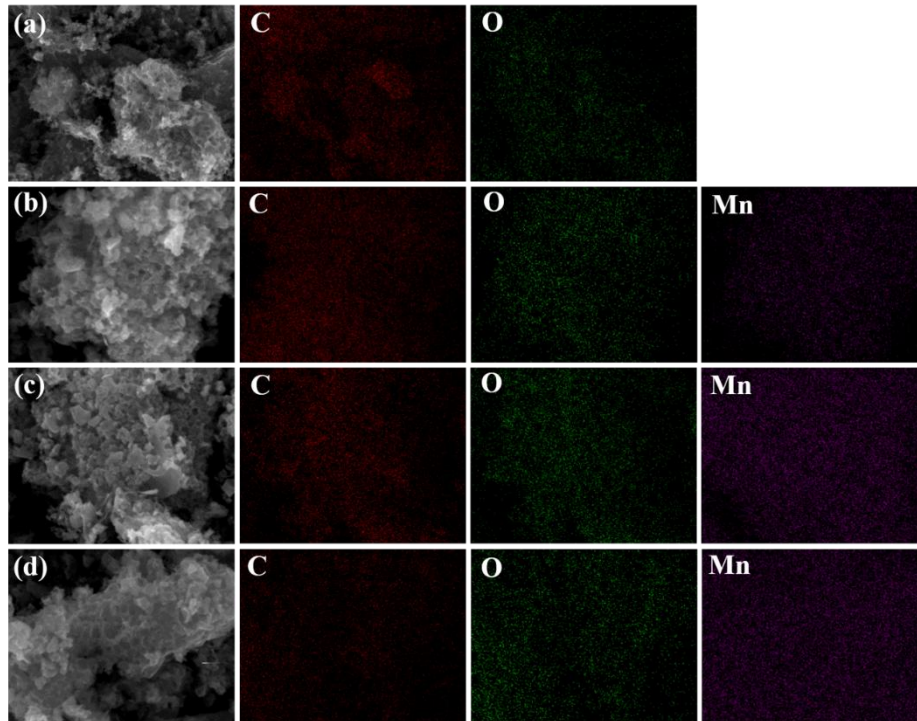


Fig. 4.4 The EDX mapping images of the KWB (a), KWBM-1 (b), KWBM-2 (c) and KWBM-3 (d) composites.

Table 4.1 EDX analysis of chemical compositions

Samples	C/at. %	O/at. %	Mn/at. %	Mn/C %
KWB	89.8	10.2	--	--
KWBM-1	57.7	15.9	26.4	45.8
KWBM-2	52.6	21.8	25.6	48.7
KWBM-3	47.3	26.5	26.2	55.4
KWBM-4	44.9	27.7	27.4	61.0

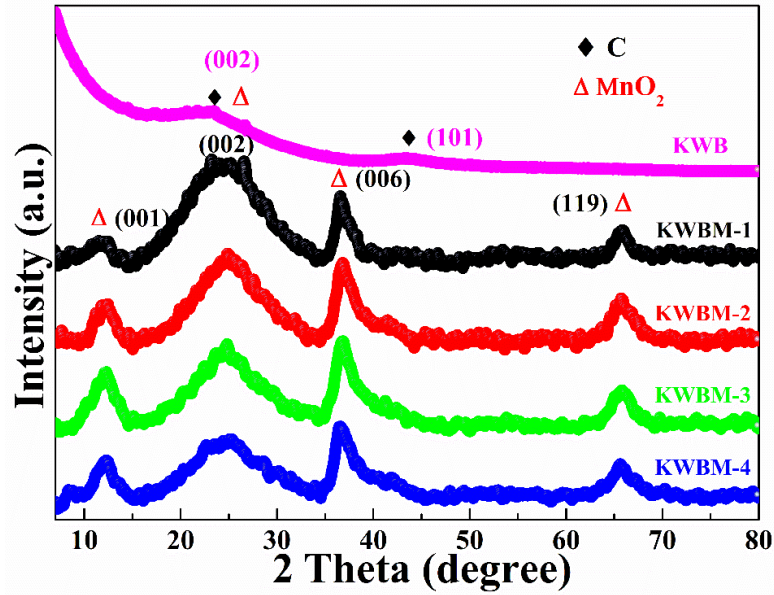


Fig. 4.5 X-ray diffraction patterns of the prepared KWB biocarbon, KWBM-1, KWBM-2, KWBM-3 and KWBM-4 composites.

The crystallinity of the samples was examined by X-ray diffraction analysis. Fig. 4.5 shows the XRD patterns of KWB and KWBM. A broad diffraction peak centered at 23.1° correspond to the (002) plane of graphite, indicating the amorphous nature [27]. Additionally, a weak diffraction peak centered at 43.4° can be attributed to the (101) plane of graphite, which means of the complete transformation of sugarcane bagasse to another kind of activated carbon [26]. For KWBM samples, the other three diffraction peaks appearing at 12.1° , 36.6° and 65.5° are indexed to the diffraction of (001), (006) and (119) planes of δ - MnO_2 , respectively (JCPDS no. 18-0802) [29]; the broad peaks suggest a poor crystallinity and almost amorphous nature of the MnO_2 nanosheets [19].

Table 4.2 Specific surface area, pore size and pore volume of samples.

Samples	Pore Volume ($\text{cm}^3 \text{g}^{-1}$)	S_{BET} ($\text{m}^2 \text{g}^{-1}$)	Average pore size (nm)	Ratio ^a (%)
KWB	0.775	1433.06	3.03	46.1
KWBM-1	0.700	1132.53	4.49	38.8
KWBM-2	0.487	769.82	5.56	33.9
KWBM-3	0.398	601.17	6.01	29.3
KWBM-4	0.331	471.33	6.23	28.8

^a Pore diameter less than 5 nm volume to total pore volume ratio.

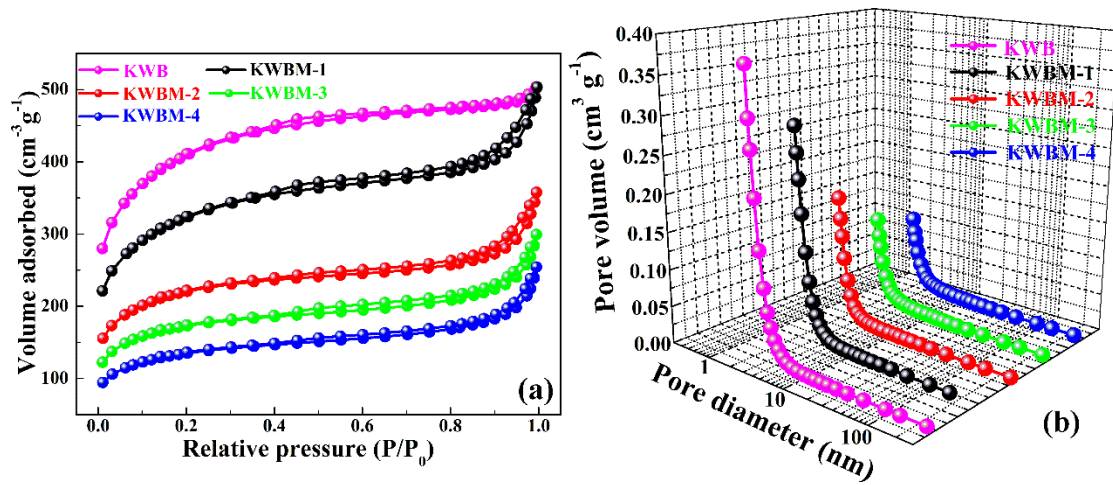


Fig. 4.6 N_2 adsorption-desorption isotherms (a) and pore size distribution by BJH method (b) of the prepared KWb biocarbon, KWBM-1, KWBM-2, KWBM-3 and KWBM-4 composites.

As we all know that the surface area and the pore-size distribution are the two key factors for the electrochemical performance of electrode materials. The specific surface area and pore-size distribution of KWb and KWBM were characterized by nitrogen adsorption/desorption measurements (as shown in Fig. 4.6a and b). It is clear that the KWb shows the typical combined I/IV type sorption isotherms, indicating the polyporous structure [30]. The specific surface area of KWb is up to $1433.06 \text{ m}^2 \text{ g}^{-1}$ (as shown in Table 4.2), which results KWb suit for acting as the scaffolds to combine with the active materials of MnO_2 . For KWBM composites, the MnO_2 nanosheets homogenously anchor on the surface of KWb and will block the mesopores and micropores of KWb. Presumably, the specific surface area of KWBM will be lower

than pure KWB, and the pore distribution will be changed.

Moreover, the specific surface area and pore distribution of KWBM can be controlled by adjust the mass ratio of KMnO_4/KWB . As shown in Table 4.2, the specific surface area and pore volume of KWBM was significantly decreased with the mass ratio of KMnO_4/KWB increased. On the contrary, the average pore size of KWBM was significantly increased with the mass ratio of KMnO_4/KWB increased. In addition, the volume ratio (pore diameter less than 5 nm volume to total pore volume ratio) of KWBM gradually decreased from 46.1% (volume ratio of KWB) with mass ratio of KMnO_4/KWB increased, which indicating that the micropores and mesopores structure of KWB gradually disappeared. However, the volume ratio and specific surface area of the KWBM-4 can still reach up to 28.8% and $471.33 \text{ m}^2 \text{ g}^{-1}$, respectively. These acceptable pore structure and specific surface area of KWBM-4 have an enough promise to be electrode material for supercapacitors application.

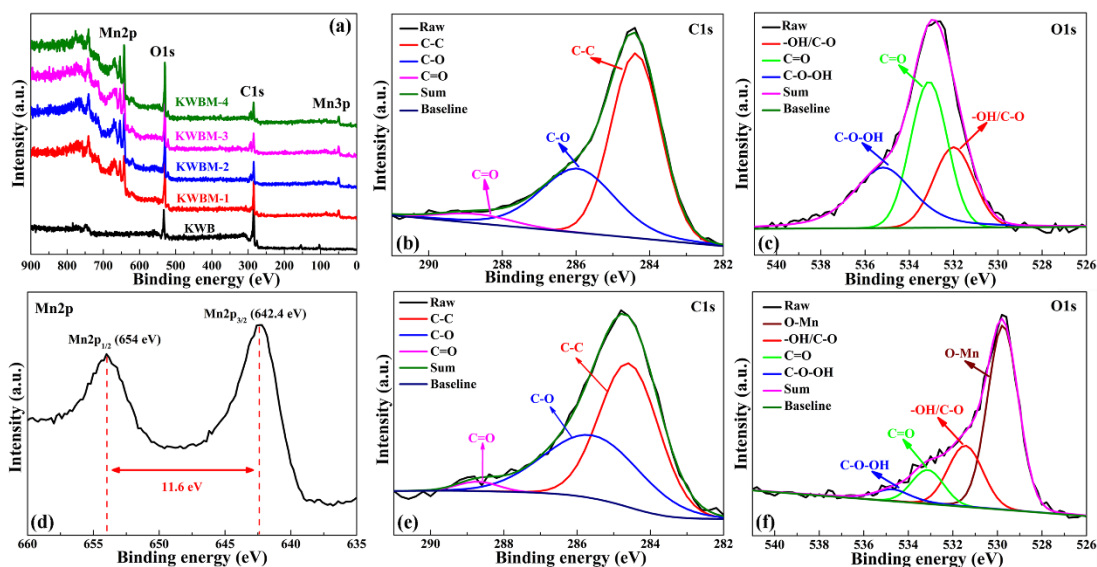


Fig. 4.7 XPS survey spectra of KWB biocarbon, KWBM-1, KWBM-2, KWBM-3 and KWBM-4 composites (a); high resolution C1s (b) and O1s (c) XPS spectra of KWB biocarbon; high resolution Mn2p (d), C1s (e) and O1s (f) XPS spectra of KWBM-4 composite.

The information of the surface chemical composition of samples was obtained from

XPS spectra. The full scan spectra of samples are shown in Fig. 4.7a. Compared with KWB, the XPS spectra of KWBM added a signal of Mn element. For KWBM composites, the content of C and O gradually decreased and increased, respectively, with the mass ratio of KMnO_4/KWB increased. Moreover, the ratio of Mn and C content were also increased with the mass ratio of KMnO_4/KWB increased. These phenomena were much accorded with EDX analysis. For Mn 2p spectra of KWBM-4 (as shown in Fig. 4.7d), two peaks located at 654 and 642.4 eV were attributed to the Mn 2p_{1/2} and Mn 2p_{3/2} with a spin-energy separation of 11.6 eV, confirmed the formation of MnO_2 [31].

Table 4.3 XPS spectrum analysis of samples

Samples	C/at. %	O/at. %	Mn/at. %	Mn/C (%)	O-Mn (%)
KWB	84.76	15.24	--	--	--
KWBM-1	50.72	26.45	22.83	45.01	56.46
KWBM-2	46.13	29.47	24.40	52.89	63.02
KWBM-3	43.43	31.89	24.68	56.83	64.22
KWBM-4	38.34	38.26	23.40	61.03	69.37

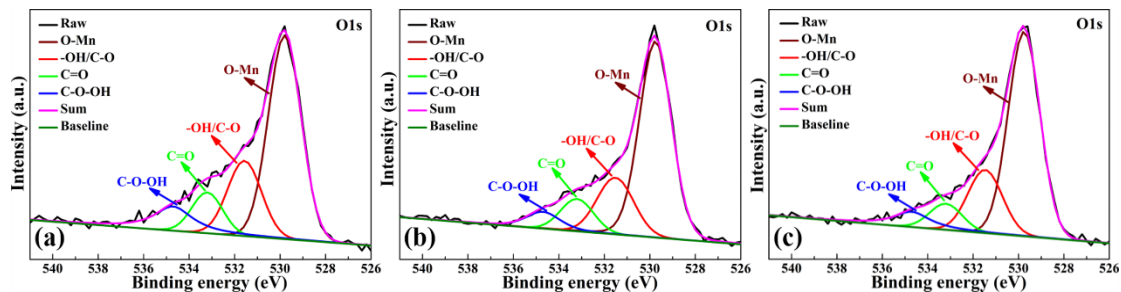


Fig. 4.8 High resolution O1s XPS spectra of KWBM-1 (a), KWBM-2 (b) and KWBM-3 (c) composites.

More information about the change of surface chemistry has been obtained by the deconvoluted high-resolution XPS spectra of two regions (C and O, as shown in Fig. 4.7). The C1s spectra of KWB and KWBM-4 in Fig. 4.7b and e can be deconvoluted into three components. The peaks of 284.4, 285.8 and 288.8 eV can be assigned to aromatic or other sp²-hybridised carbon atoms bound to neighboring carbon atoms (C-C, 284.4 eV), carbon in C-O (285.8 eV) and C=O (288.8 eV), respectively [32]. The

O1s spectra of KWB could be deconvoluted into three peaks (as shown in Fig. 4.7c) with binding energies of 531.5, 533.2 and 534.8 eV. These peaks could be assigned to –OH/C-O, C=O and C-O-OH groups, respectively [33]. Compared with KWB, except the above three peaks in O1s spectra of KWBM-4 (as shown in Fig. 4.7f), the other new peak appeared in 529.8 eV, which can be attributed to oxygen bonded with manganese (O-Mn) in MnO₂ crystal lattice [34]. The content of oxygen atom in O-Mn of KWBM (which obtained by O1s spectra of KWBM-1, 2, 3 and 4, as shown in Fig. 4.7f and 4.8) is also listed in Table 4.3. It is easy to find that the content of O-Mn was significantly increased with the mass ratio of KMnO₄/KWB increased. These transformation further evidences that the element composition of KWBM can be controlled by adjusting the mass ratio of KMnO₄/KWB, and the mass ratio has a meaningful impact on electrochemical performance of KWBM composites.

4.3.2 Electrochemical performance of KWBM composites

To explore potential applications of the KWBM composites to supercapacitors, we first performed the CV, GCD and EIS measurements in a three-electrode configuration. Fig. 4.9 shows the CV curves of KWBM composites at a scan rate of 0.01 V s⁻¹.

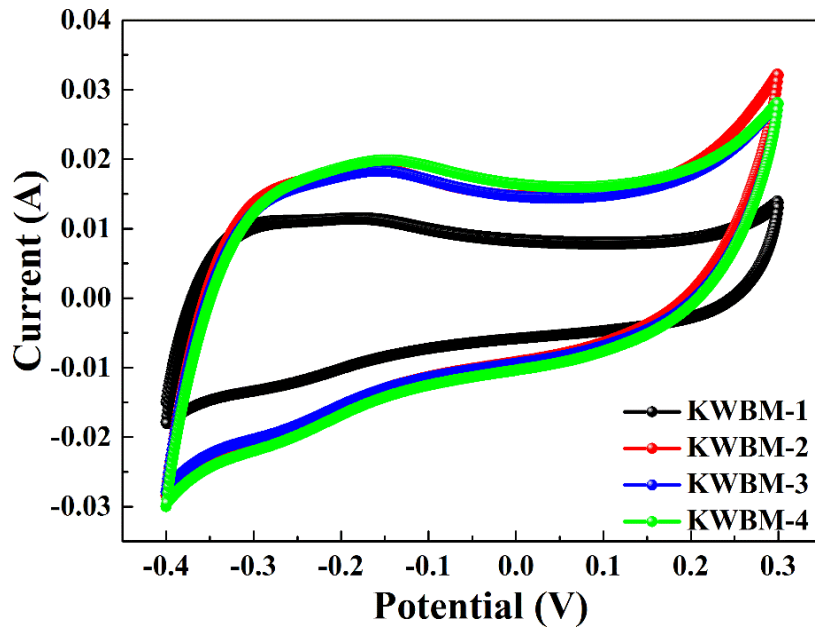


Fig. 4.9 CV curves of KWBM composites at scan rate of 0.01 V s⁻¹

Different from CV curve of KWB (as show in Fig. 3.11), all the CV curves of KWBM deviate from the rectangular shape, due to the charge storage process of MnO₂-based electrode. Some researchers have proposed that the process of charge storage was ascribed to the rapid intercalation of alkali metal cations such as K⁺ intercalation into the electrode during reduction and deintercalation upon oxidation [35, 36], as shown in reaction (Re. 2):



where M⁺ = Na⁺, K⁺, and Li⁺. It should be noted that the process involved a redox reaction, and which can significantly improve the capacitive performance. Furthermore, KWBM-4 electrode exhibited a much larger current response than that of the other electrode, and presented an excellent electrochemical performance, attributing to the acceptable microstructure and element composition.

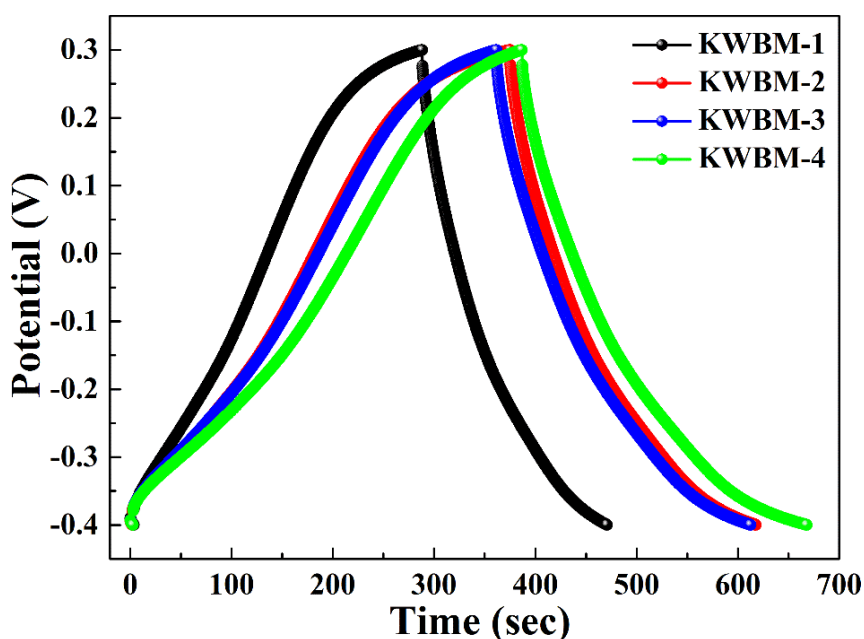


Fig. 4.10 GCD curves of KWBM composites at current density of 1 A g⁻¹.

The electrochemical performance of KWBM was further analyzed by the GCD method and the results are shown in Fig. 4.10. All the charge curves of the KWBM were almost symmetrical to their corresponding discharge curves with slight deformation, indicating that the capacitance is in account of the combination of

electrical double-layer capacitance (EDLC) and pseudocapacitance corresponds to Re. 2. Moreover, the discharge time of KWBM-4 is longer than that of other samples, indicating that the KWBM-4 possesses the more excellent capacitive performance than the other samples. The specific capacitance (SC) of KWBM could be got by Eq. 1. The SC of KWBM-1, 2, 3 and 4 are 260, 346, 360 and 402 F g⁻¹, respectively, at a current density of 1 A g⁻¹. The SC of KWBM increases with the increase of the KMnO₄/KWB mass ratio. These results are further evidences for the inference form CV curves.

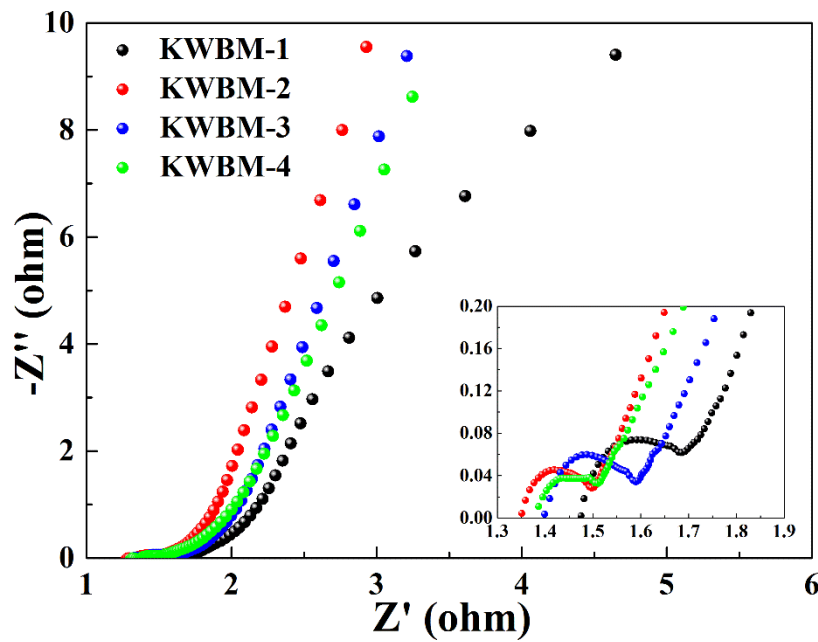


Fig. 4.11 EIS curves of KWBM composites.

The EIS measurements were performed in order to further explore the charge transport and ion diffusion between KWBM electrode and electrolyte. The Nyquist plots of KWBM are showed in Fig. 4.11. All samples present similar shapes, and are composed of three parts: a semi-circular line in the high frequency region (as shown in the inset of Fig. 4.11), a nearly 45° diagonal line in the medium frequency region and a nearly vertical line in the low frequency region. These three parts correspond to charge transfer resistance, diffusion resistance and capacitive behavior, respectively [37]. From the inset, is easily found that the KWBM-4 exhibits the smaller charge transfer resistance than the other samples due to the fact that it has the least diameter of arc.

Furthermore, KWBM-4 shows the shortest 45° diagonal line and the largest slope of the straight line at the medium and low frequency region, respectively, indicating that KWBM-4 also possesses the lowest different resistance and best excellent capacitive performance than those of the other samples. In addition, the very high-frequency intercept at the real axis at the beginning of the arc represents the internal resistance (R_s), including the intrinsic resistance of the sample, the contact resistance between the sample and current collector, and the resistance of bulk electrolyte [38]. The inset shows that the R_s of KWBM-1, 2, 3 and 4 are 1.48, 1.39, 1.40 and 1.35 Ω , respectively. These above results indicate that KWBM-4 possesses an outstanding capacitive performance, and this conclusion agrees with the analyses of CV and GCD measurements.

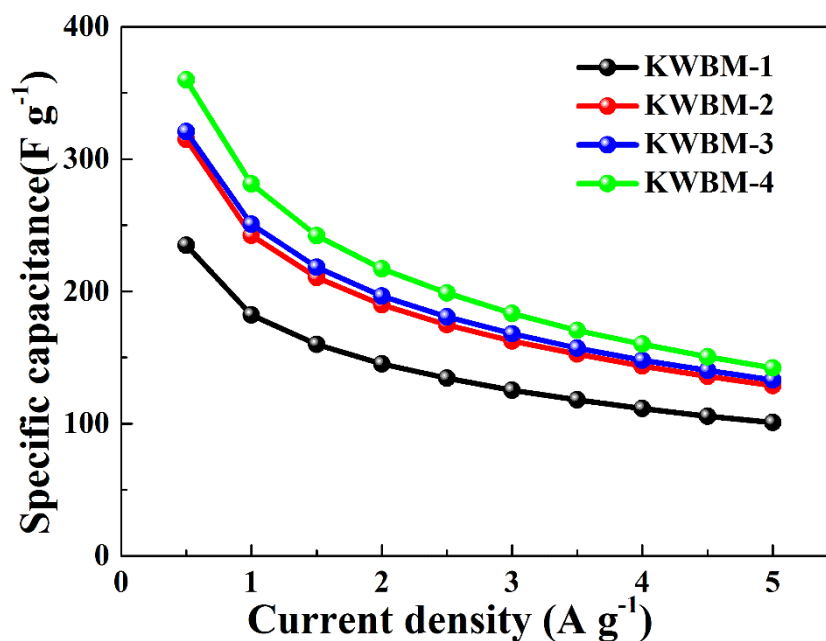


Fig. 4.12 Specific capacitance versus current density of KWBM composite

Fig. 4.12 shows the SC as a function of current density for KWBM composites. In general, the SC of all samples decreases with the increase of current density, this is may be due to the contribution of MnO_2 pseudocapacitance to total capacitance decrease with the current density increase. Moreover, it is noteworthy that the SC downtrend of KWBM-4 is larger than that of the other samples. This is mainly due to the specific surface area of KWBM-4 is smaller than that of the other samples, resulting in that the

contact area of KWBM-4 and electrolyte is smallest among all samples. However, the SC of KWBM-4 could still reach to 203 F g^{-1} at the current density of 5 A g^{-1} , and this value is still larger than that of the other samples. This result suggests that the KWBM-4 possesses the fast charge-discharge performance, which is essential for supercapacitors application.

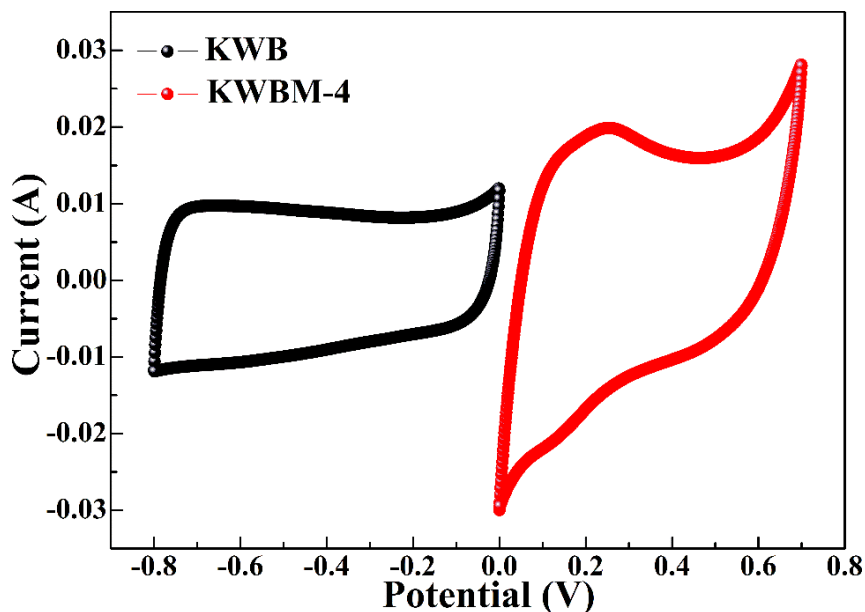


Fig. 4.13 CV curves of KWB and KWBM-4 in three-electrode asymmetric system at a scan rate of 0.01 V s^{-1} .

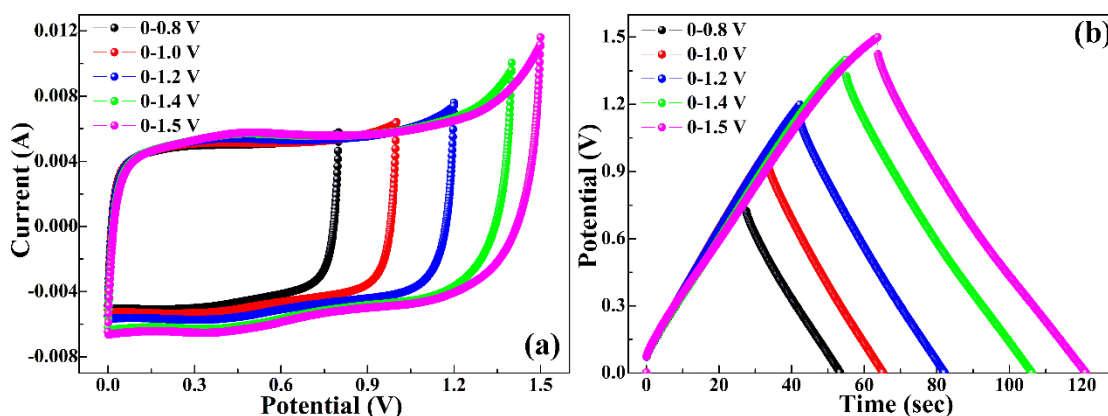


Fig. 4.14 CV (a, scan rate of 0.01 V s^{-1}) and GCD (b, current density of 1 A g^{-1}) curves of two-electrode asymmetric system (using KWBM-4 and KWB as the positive and negative electrode, respectively) at different potential windows.

CV curves of KWBM-4//KWB measured at scan rate of 0.01 V s^{-1} exhibit rectangular-like shapes (as shown in Fig. 4.14a) even at the potential window up to 1.5 V, demonstrating KWBM-4//KWB present an ideal capacitive behavior. Moreover, a pair of weak redox peaks appears in all CV curves, suggesting that the pseudocapacitance and EDLC capacitance are simultaneously exist. In addition, there is no significant increase of anodic current at potential window of 0-1.5 V, which implies that the electrolyte is not decomposed, because that the storage of nascent hydrogen on the electrode is below the thermodynamic potential for water decomposition [40]. Fig. 4.14b shows the GCD curves of KWBM-4//KWB at current density of 2 A g^{-1} under different potential windows. Similar to CV curves, all GCD curves show the equilateral triangle-like shape even at the potential window up to 1.5 V, which still implies the ideal capacitive behavior of KWBM-4//KWB. The SC of KWBM-4//KWB from these GCD curves can be obtained by Eq. 1. The SC is 63.4, 65.1, 66.5, 73.3 and 76.5 F g^{-1} at 0-0.8, 0-1.0, 0-1.2, 0-1.4 and 0-1.5 V, respectively. Therefore, these above results confirm that the best potential window of KWBM-4//KWB is 0-1.5 V.

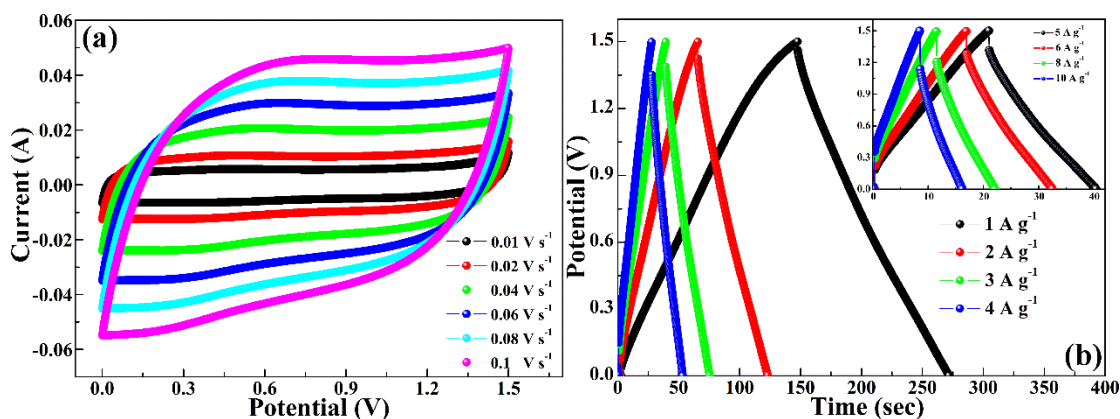


Fig. 4.15 CV (a) and GCD (b) curves of asymmetric system measured at different scan rates and current densities in a potential window of 1.5 V, respectively (using KWBM-4 and KWB as the positive and negative electrode, respectively).

Fig. 4.15a shows the CV curves of the KWBM-4//KWB measured at various scan rates of 0.01-0.1 V s^{-1} during 0 and 1.5 V. The CV curves exhibit a nearly rectangular-

like shape, which also indicate the ideal capacitive behavior. The rectangular CV shape remains very well even at a high scan rate of 0.1 V s^{-1} , indicating KWBM-4//KWB possesses outstanding rate capability and meets high-power supercapacitors. GCD measurements were made at different current densities to further evaluate the capacitive performance of the KWBM-4//KWB at the potential window of 0-1.5 V, as shown in Fig. 4.15b. These GCD curves are highly linear and symmetrical, indicating a rapid response of current and voltage, and an excellent electrochemical reversibility [9]. The SC of KWBM-4//KWB is 82.9 F g^{-1} at a current density of 1 A g^{-1} , and still remains at 51.3 F g^{-1} when the current density increases to 10 A g^{-1} , further suggesting that the KWBM-4//KWB has excellent capacitive performance.

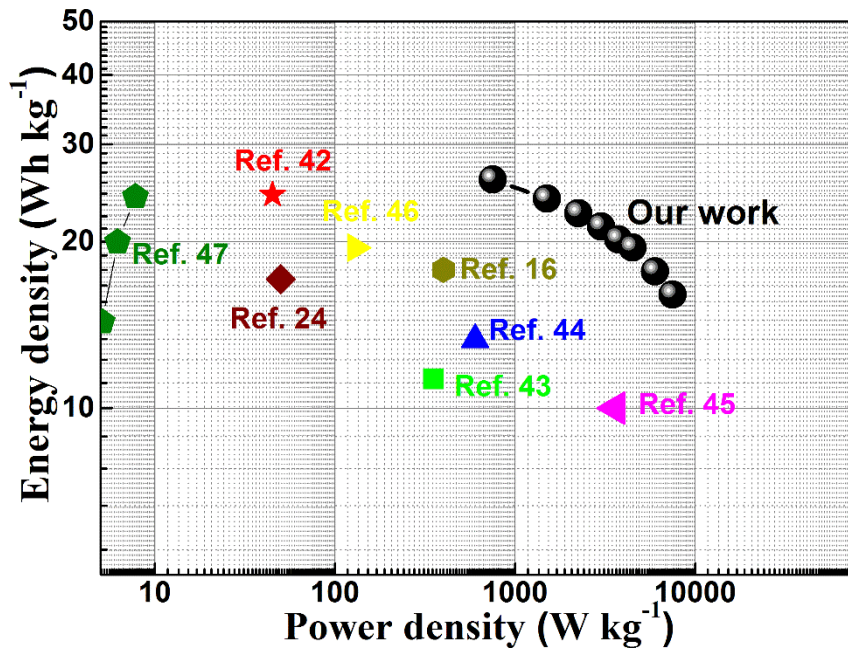


Fig. 4.16 Ragone plot of asymmetric system.

Ragone plot, a performance indicator of power density against energy density, was drawn to characterize the electrochemical performance of KWBM-4//KWB [37]. The energy density (E , Wh kg⁻¹) and power density (P , W kg⁻¹) were calculated from the discharge curves according to the following equations [41]:

$$E = 1/2 C_m (\Delta V)^2 \quad (\text{Eq. 2})$$

$$P = E/t \quad (\text{Eq. 3})$$

where C_m , t and ΔV are the SC, discharge time (h) and potential window (V) of

KWBM-4//KWB, respectively. Fig. 4.16 shows the Ragone plot of KWBM-4//KWB. It is obviously that the KWBM-4//KWB shows the outstanding performance with 25.9 Wh kg⁻¹ of the energy density at a power density of 750 W kg⁻¹. The exciting performance is comparable or superior to those of MnO₂-based asymmetric two-electrode system reported in literature (Table 4.4).

Table 4.4 Performance of MnO₂-based electrodes in asymmetric two-electrode system.

Positive electrode	Negative electrode	Cell voltage (V)	Energy density (Wh kg ⁻¹)	Power density	Ref.
rGO/MnO ₂ /CB	rGO/CB	1.8 V	24.3	45 kW kg ⁻¹	[42]
MnO ₂ /CNF	Bi ₂ O ₃ /CNF	1.8 V	11.3	352.6 W kg ⁻¹	[43]
MnO ₂ /CNTs	AC	1.5 V	13.3	600 W kg ⁻¹	[44]
MnO ₂	AC	1.5 V	7.4	400 W kg ⁻¹	[45]
NaMnO ₂	AC	1.8 V	19.5	130 W kg ⁻¹	[46]
MnO ₂ /MnCO ₃ /rGO	rGO	1.8 V	17.8	400 W kg ⁻¹	[16]
MnO ₂ -nanorods	rGO	1.6	14.31	5.1 kW kg ⁻¹	[47]
MnO ₂ -nanowires	rGO	1.4	19.97	6.2 kW kg ⁻¹	[47]
MnO ₂ -nanoneedles	rGO	1.8	24.12	7.8 kW kg ⁻¹	[47]
MnO ₂	PEDOT	1.8	13.5	120.1 kW kg ⁻¹	[48]
KWBM-4	KWB	1.5	25.9	750 W kg ⁻¹	This work

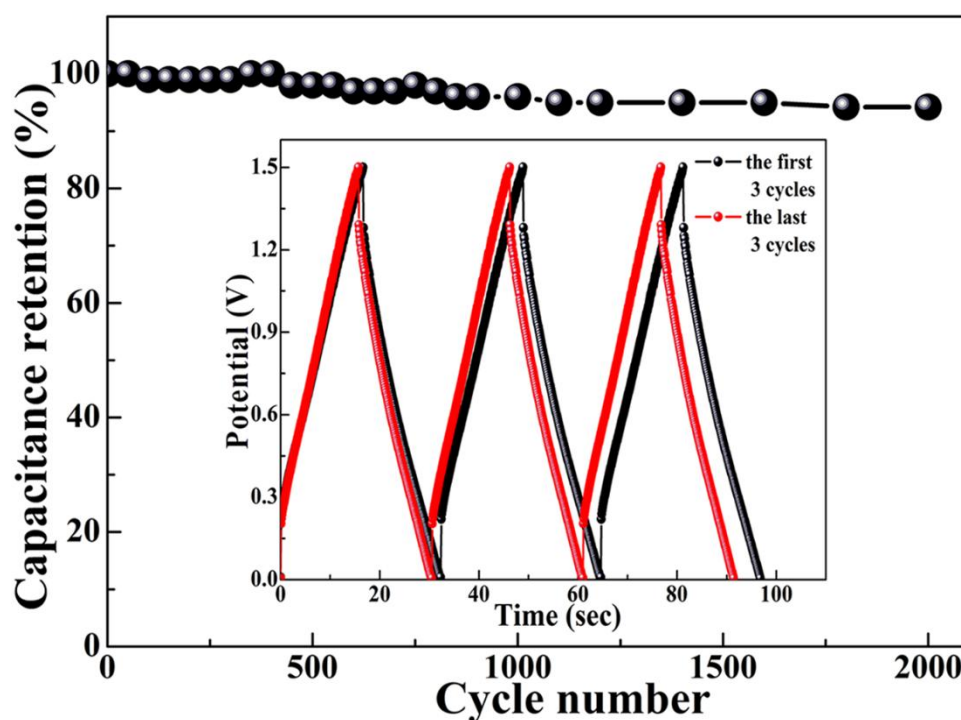


Fig. 4.17 Cycle stability of asymmetric system

The long-term cycling stability is an important criterion for supercapacitors applications. The cycle stability measurement 2000 cycles for KWBM-4//KWB was conducted using GCD test at 6 A g^{-1} and the results are shown in Fig. 4.17. The KWBM-4//KWB exhibits excellent cycle stability with 94.2 % SC retention after 2000 cycles. The inset in Fig. 4.17 represents GCD curves of the first three and last three cycles. The last three cycles remain the symmetric triangular shape, indicating KWBM-4//KWB still keep the ideal capacitive performance. Furthermore, cycling performance of KWBM-4//KWB is comparable to those of other MnO_2 -based asymmetric two-electrode system reported in literature (Table 4.5).

Table 4.5 Cycling performance of MnO_2 -based electrodes in asymmetric two-electrode system

Positive electrode	Negative electrode	Cell voltage	Capacitance retention after cycling	Ref.
MnO_2	CNT-CNF	2.0 V	92% after 2000 cycles	[11]
MnO_2/MWNT	MWNTs	2.45V	72% after 300 cycles	[49]
MnO_2	FeOOH	1.85 V	85% after 300 cycles	[50]
CNTs/ MnO_2	CNTs/ SnO_2	1.7 V	92% after 1000 cycles	[51]
KWBM-4	KWB	1.5 V	94.2% after 2000 cycles	This work

4.4 Conclusions

In this work, we successful prepared the allium-giganteum-like biocarbon—KWB, which derived from the common biomass of sugarcane bagasse using one-step facile carbonization and activation method. The interconnected frameworks of KWB offered a fine platform for anchoring MnO_2 nanosheets. Subsequently, MnO_2 nanosheets were uniformly distributed on the surface of KWB by in-suit redox deposition and obtained the KWBM composites. The electrochemical performance of KWBM was closely related to the mass ratio of KMnO_4/KWB . KWBM-4 showed the best electrochemical performance when the mass ratio of KMnO_4/KWB was 2 in three-electrode system. When employing the KWBM-4 as the positive electrode and the KWB as the negative

electrode, the assembled asymmetric two-electrode system exhibited a remarkable energy density of 25.9 Wh kg⁻¹, excellent rate capability and high cycle stability (SC retention is 94.2 % after 2000 cycles). Therefore, it is a promising strategy for employing low-cost and eco-friendly biomaterials to prepare advanced electrode materials for energy storage devices.

References

- [1] G. Wang, L. Zhang, J. Zhang, A review of electrode materials for electrochemical supercapacitors, *Chem. Soc. Rev.* 41 (2012) 797-828.
- [2] Y. Zhai, Y. Dou, D. Zhao, P.F. Fulvio, R.T. Mayes, S. Dai, Carbon materials for chemical capacitive energy storage, *Adv. Mater.* 23 (2011) 4828-4850.
- [3] Z. Zheng, Q. Gao, Hierarchical porous carbons prepared by an easy one-step carbonization and activation of phenol-formaldehyde resins with high performance for supercapacitors, *J. Power Sources.* 196 (2011) 1615-1619.
- [4] J. Wang, S. Kaskel, KOH activation of carbon-based materials for energy storage, *J. Mater. Chem.* 22 (2012) 23710-23725.
- [5] C. Yang, M. Zhou, Q. Xu, Three-dimensional ordered macroporous MnO₂/carbon nanocomposites as high-performance electrodes for asymmetric supercapacitors, *Phys. Chem. Chem. Phys.* 15 (2013) 19730-19740.
- [6] H. Chen, D. Liu, Z. Shen, B. Bao, S. Zhao, L. Wu, Functional Biomass Carbons with Hierarchical Porous Structure for Supercapacitor Electrode Materials, *Electrochim. Acta.* 180 (2015) 241-251.
- [7] M. Zhi, C. Xiang, J. Li, M. Li, N. Wu, Nanostructured carbon-metal oxide composite electrodes for supercapacitors: a review, *Nanoscale.* 5 (2013) 72-88.
- [8] L. Yuan, X.H. Lu, X. Xiao, T. Zhai, J. Dai, F. Zhang, B. Hu, X. Wang, L. Gong, J. Chen, C. Hu, Y. Tong, J. Zhou, Z.L. Wang, Flexible solid-state supercapacitors based on carbon nanoparticles/MnO₂ nanorods hybrid structure, *ACS Nano.* 6 (2012) 656-661.
- [9] C. Long, D. Qi, T. Wei, J. Yan, L. Jiang, Z. Fan, Nitrogen-doped carbon networks for high energy density supercapacitors derived from polyaniline coated bacterial cellulose, *Adv. Funct. Mater.* 24 (2014) 3953-3961.
- [10] T.E. Rufford, D. Hulicova-jurcakova, K. Khosla, Z. Zhu, G.Q. Lu, Microstructure and electrochemical double-layer capacitance of carbon electrodes prepared by zinc chloride activation of sugar cane bagasse, *J. Power Sources.* 195 (2010) 912-918.
- [11] C.H. Wang, H.C. Hsu, J.H. Hu, High-energy asymmetric supercapacitor based on

- petal-shaped MnO₂ nanosheet and carbon nanotube-embedded polyacrylonitrile-based carbon nanofiber working at 2 v in aqueous neutral electrolyte, *J. Power Sources*. 249 (2014) 1-8.
- [12] R. Jiang, T. Huang, J. Liu, J. Zhuang, A. Yu, A novel method to prepare nanostructured manganese dioxide and its electrochemical properties as a supercapacitor electrode, *Electrochim. Acta*. 54 (2009) 3047-3052.
- [13] W. Wei, X. Cui, W. Chen, D.G. Ivey, Manganese oxide-based materials as electrochemical supercapacitor electrodes, *Chem. Soc. Rev.* 40 (2011) 1697-1721.
- [14] Q. Li, X.-F.F. Lu, H. Xu, Y.-X.X. Tong, G.-R.R. Li, Carbon/MnO₂ double-walled nanotube arrays with fast ion and electron transmission for high-performance supercapacitors, *ACS Appl. Mater. Interfaces*. 6 (2014) 2726-2733.
- [15] P.C. Gao, A.H. Lu, W.C. Li, Dual functions of activated carbon in a positive electrode for MnO₂-based hybrid supercapacitor, *J. Power Sources*. 196 (2011) 4095-4101.
- [16] Y. Liu, D. He, H. Wu, J. Duan, Y. Zhang, Hydrothermal Self-assembly of Manganese Dioxide/Manganese Carbonate/Reduced Graphene Oxide Aerogel for Asymmetric Supercapacitors, *Electrochim. Acta*. 164 (2015) 154-162.
- [17] P. Xu, B. Wei, Z. Cao, J. Zheng, K. Gong, F. Li, J. Yu, Q. Li, W. Lu, J.-H. Byun, B.-S. Kim, Y. Yan, T.-W. Chou, Stretchable Wire-Shaped Asymmetric Supercapacitors Based on Pristine and MnO₂ Coated Carbon Nanotube Fibers, *ACS Nano*. 9 (2015) 6088-96.
- [18] M. Huang, F. Li, F. Dong, X. Zhang, L. Li, MnO₂-based nanostructures for high-performance supercapacitors, *J. Mater. Chem. A Mater. Energy Sustain.* 3 (2015) 21380-21423.
- [19] Y.Y. Li, N. Yu, P. Yan, Y.Y. Li, X. Zhou, S. Chen, G. Wang, T. Wei, Z. Fan, Fabrication of manganese dioxide nanoplates anchoring on biomass-derived cross-linked carbon nanosheets for high-performance asymmetric supercapacitors, *J. Power Sources*. 300 (2015) 309-317.
- [20] W. S. Hummers, R. E. Offeman, Preparation of graphitic oxide *J. Am. Chem. Soc.* 1958, 80, 1339.

- [21]H. Feng, B. Wang, L. Tan, N. Chen, N. Wang, B. Chen, Polypyrrole/hexadecylpyridinium chloride-modified graphite oxide composites: Fabrication, characterization, and application in supercapacitors, *J. Power Sources*. 246 (2014) 621-628.
- [22]E. Raymundo-Piñero, F. Leroux, F. Béguin, A high-performance carbon for supercapacitors obtained by carbonization of a seaweed biopolymer, *Adv. Mater.* 18 (2006) 1877-1882.
- [23]B. Li, F. Dai, Q. Xiao, L. Yang, J. Shen, C. Zhang, M. Cai, Nitrogen-doped Activated Carbon for High Energy Hybrid Supercapacitor, *Energy Environ. Sci.* 9 (2015) 102-106.
- [24]Q. Xie, R. Bao, C. Xie, A. Zheng, S. Wu, Y. Zhang, R. Zhang, P. Zhao, Core-shell N-doped active carbon fiber@graphene composites for aqueous symmetric supercapacitors with high-energy and high-power density, *J. Power Sources*. 317 (2016) 133-142.
- [25]R. J. Mo, Y. Zhao, M. Wu, H. M. Xiao, S. Kuga, Y. Huang, J. P. Li, S. Y. Fu, Activated carbon from nitrogen rich watermelon rind for high-performance supercapacitors, *RSC Adv.* 6 (2016) 59333-59342.
- [26]B. Wang, J. Qiu, H. Feng, E. Sakai, T. Komiyama, Nitrogen doped carbon nanowires prepared from polypyrrole nanowires for potential application in supercapacitors, *J. Electroanal. Chem.* 775 (2016) 219-227.
- [27]H. Feng, H. Hu, H. Dong, Y. Xiao, Y. Cai, B. Lei, Y. Liu, M. Zheng, Hierarchical structured carbon derived from bagasse wastes: A simple and efficient synthesis route and its improved electrochemical properties for high-performance supercapacitors, *J. Power Sources*. 302 (2016) 164-173.
- [28]M. Huang, R. Mi, H. Liu, F. Li, X.L. Zhao, W. Zhang, S.X. He, Y.X. Zhang, Layered manganese oxides-decorated and nickel foam-supported carbon nanotubes as advanced binder-free supercapacitor electrodes, *J. Power Sources*. 269 (2014) 760-767.
- [29]S. He, W. Chen, High performance supercapacitors based on three-dimensional ultralight flexible manganese oxide nanosheets/carbon foam composites, *J. Power*

Sources. 262 (2014) 391-400.

- [30] L. Mao, Y. Zhang, Y. Hu, K.H. Ho, Q. Ke, H. Liu, Z. Hu, D. Zhao, J. Wang, Activation of sucrose-derived carbon spheres for high-performance supercapacitor electrodes, *RSC Adv.* 5 (2015) 9307-9313.
- [31] M. Kim, J. Kim, Development of high power and energy density microsphere silicon carbide-MnO₂ nanoneedles and thermally oxidized activated carbon asymmetric electrochemical supercapacitors., *Phys. Chem. Chem. Phys.* 16 (2014) 11323–11336.
- [32] K. Y. Chun, H.S. Lee, C.J. Lee, Nitrogen doping effects on the structure behavior and the field emission performance of double-walled carbon nanotubes, *Carbon N. Y.* 47 (2009) 169-177.
- [33] H. Liu, Y. Zhang, R. Li, X. Sun, S. D é silets, H. Abou-Rachid, M. Jaidann, L.S. Lussier, Structural and morphological control of aligned nitrogen-doped carbon nanotubes, *Carbon N. Y.* 48 (2010) 1498-1507.
- [34] B. Wang, J. Qiu, H. Feng, N. Wang, E. Sakai, T. Komiyama, Preparation of MnO₂/carbon nanowires composites for supercapacitors, *Electrochim. Acta.* 212 (2016) 710-721.
- [35] B. Yin, S. Zhang, H. Jiang, F. Qu, X. Wu, Phase-controlled synthesis of polymorphic MnO₂ structures for electrochemical energy storage, *J. Mater. Chem. A.* 3 (2015) 5722-5729.
- [36] V. Subramanian, H. Zhu, R. Vajtai, P.M. Ajayan, B. Wei, Hydrothermal synthesis and pseudocapacitance properties of MnO₂ nanostructures, *J. Phys. Chem. B.* 109 (2005) 20207-20214.
- [37] J.G. Wang, Y. Yang, Z.H. Huang, F. Kang, A high-performance asymmetric supercapacitor based on carbon and carbon-MnO₂ nanofiber electrodes, *Carbon N. Y.* 61 (2013) 190-199.
- [38] T. Cai, M. Zhou, D. Ren, G. Han, S. Guan, Highly ordered mesoporous phenol-formaldehyde carbon as supercapacitor electrode material, *J. Power Sources.* 231 (2013) 197-202.
- [39] J. Yan, Q. Wang, T. Wei, Z. Fan, Recent advances in design and fabrication of

- electrochemical supercapacitors with high energy densities, *Adv. Energy Mater.* 4 (2014) 1300816.
- [40] C. Long, L. Jiang, X. Wu, Y. Jiang, D. Yang, C. Wang, T. Wei, Z. Fan, Facile synthesis of functionalized porous carbon with three-dimensional interconnected pore structure for high volumetric performance supercapacitors, *Carbon N. Y.* 93 (2015) 412-420.
- [41] S.A. El-Khodary, G.M. El-Enany, M. El-Okr, M. Ibrahim, Preparation and Characterization of Microwave Reduced Graphite Oxide for High-Performance Supercapacitors, *Electrochim. Acta.* 150 (2014) 269-278.
- [42] J. Chen, Y. Wang, J. Cao, Y. Liu, J.H. Ouyang, D. Jia, Y. Zhou, Flexible and solid-state asymmetric supercapacitor based on ternary graphene/MnO₂/carbon black hybrid film with high power performance, *Electrochim. Acta.* 182 (2015) 861-870.
- [43] H. Xu, X. Hu, H. Yang, Y. Sun, C. Hu, Y. Huang, Flexible asymmetric micro-supercapacitors based on Bi₂O₃ and MnO₂ nanoflowers: Larger areal mass promises higher energy density, *Adv. Energy Mater.* 5 (2015) 1-7.
- [44] L. Li, Z.A. Hu, N. An, Y.Y. Yang, Z.M. Li, H.Y. Wu, Facile Synthesis of MnO₂/CNTs Composite for Supercapacitor Electrodes with Long Cycle Stability, *J. Phys. Chem. C.* 118 (2014) 22856-22872.
- [45] T. Brousse, M. Toupin, D. Bélanger, A Hybrid Activated Carbon-Manganese Dioxide Capacitor using a Mild Aqueous Electrolyte, *J. Electrochem. Soc.* 151 (2004) A614-A622.
- [46] Q.T. Qu, Y. Shi, S. Tian, Y.H. Chen, Y.P. Wu, R. Holze, A new cheap asymmetric aqueous supercapacitor: Activated carbon//NaMnO₂, *J. Power Sources.* 194 (2009) 1222-1225.
- [47] D.P. Dubal, R. Holze, P. Gomez-Romero, Three-Dimensional Arrays of 1D MnO₂ Nanocrystals for All-Solid-State Asymmetric Supercapacitors, *Chempluschem.* (2015) 1-9.
- [48] V. Khomenko, E. Raymundo-Piñero, E. Frackowiak, F. Béguin, High-voltage asymmetric supercapacitors operating in aqueous electrolyte, *Appl. Phys. A Mater. Sci. Process.* 82 (2006) 567-573.

- [49]G.X. Wang, B.L. Zhang, Z.L. Yu, M.Z. Qu, Manganese oxide/MWNTs composite electrodes for supercapacitors, *Solid State Ionics*. 176 (2005) 1169-1174.
- [50]W.H. Jin, G.T. Cao, J.Y. Sun, Hybrid supercapacitor based on MnO₂ and columned FeOOH using Li₂SO₄ electrolyte solution, *J. Power Sources*. 175 (2008) 686-691.
- [51]K.C. Ng, S. Zhang, C. Peng, G.Z. Chen, Individual and Bipolarly Stacked Asymmetrical Aqueous Supercapacitors of CNTs/SnO₂ and CNTs/MnO₂ Nanocomposites, *J. Electrochem. Soc.* 156 (2009) A846-A853.

Chapter 5 Polyaniline/sugarcane bagasse derived biocarbon composites with superior performance in supercapacitors

5.1 Introduction

Supercapacitors are one of the most promising energy storage devices due to their superior power density, fast charge/discharge rate, and long cycle life [1-4]. According to the energy storage mechanism, supercapacitors can be classified as pseudocapacitors and electrical double-layer capacitors (EDLC) [5, 6]. Polyaniline is a typical electrode material of pseudocapacitors, and it possesses many advantages, such as: ease of synthesis, high conductivity, highly reversibility and large storage capacity [7-9]. Unfortunately, its electrochemical performance tends to fade for swelling and shrinking during cycling (the insertion/deinsertion process of counter ions), which hinder its further application in supercapacitors [10].

To respond the above problems, some research focused on preparation of PANI/carbon composites. Until now, many kinds of carbon materials, such as carbon nanotube [11], graphene [12] and carbon nanofibers [13] are often used as the content of PANI/carbon composites because their superior electronic conductivity, high specific surface, special microstructure, reasonable chemical stability and excellent thermal stability [14]. However, the preparation processes of these carbon materials are complex, and these carbon materials usually need a pretreatment process for preparation of PANI/carbon composites, leading to high cost [15-17].

Therefore, simple and low cost preparation method of carbon materials such as direct pyrolysis of biomass or biowaste entered the researcher's vision [18-21]. In recent years, many biocarbon materials have been prepared from biomass such as fallen leave [22], ramie [23], coffee endocarp [24] and cassava peel [25]. The above biocarbon materials present high specific surface area and abundant surface oxygen functional groups,

which makes them suitable for preparation of PANI/carbon composites. Especially, we found an allium-giganteum-like microstructure in sugarcane bagasse derived biocarbon, it not only has the above advantages, but also presents an allium-giganteum-like microstructure [26]. This particular microstructure is possibly beneficial to ion transport if this biocarbon is applied to supercapacitors.

In this paper, we report an efficient method for preparation of PANI/biocarbon composites (PANI/KWB) which are going to be as electrode materials for supercapacitors. The biocarbon (KWB) was obtained by direct pyrolysis of sugarcane bagasse, and then PANI/KWB was obtained by in-site polymerization method under different mass ratios of An/KWB. During the polymerization process, [CMMIm]Cl ionic liquid (IL) was chosen as dopant is due to its proton acid and surfactant features [27, 28]. We found that chemical composition and microstructure of PANI/KWB were closely related to the mass ratio of aniline monomer (An) and KWB, and which further impacted electrochemical performance of PANI/KWB profoundly. In addition, an asymmetric two-electrode system was assembled by employing PANI/KWB and KWB as positive and negative electrode. We also found that the asymmetric system possessed the high energy density and high cycle stability. The results indicate a promising candidate for supercapacitors.

5.2 Experimental

5.2.1 Materials

Sugarcane bagasse was crushed by family-use grinder before use. Aniline monomer (An) was purified by distillation under reduced pressure and stored at 4 °C in dark. The ionic liquid (IL), 1-methyl-3-alkylcarboxylic acid imidazolium chloride ([CMMIm]Cl), was synthesized in our laboratory and the synthesis method described in supporting information. The other reagents, such as ethanol, potassium hydroxide (KOH), hydrochloric acid (HCl), and ammonium persulfate (APS), were all purchased from Nacalai Tesque, Inc.(Kyoto, Japan) and of analytical grade, being used without further

purification.

5.2.2 Synthesis of 1-methyl-3-alkylcarboxylic acid imidazolium chloride ([CMMIm]Cl) ionic liquid

The [CMMIm]Cl was prepared as Fei reported. [27] In a typical fabrication of [CMMIm]Cl, 0.17 mol chloroacetic acid solid was added spoonful to 0.15 mol N-Methylimidazole liquid with stirring in 1 h at 15-20 °C. When the mixed solution uniform, put it into water bath kettle to heat up to 70 °C and run the reaction for 3-5 h. After that, the solution was used for suction filtration and washed the material with 30 ml of methyl cyanide for twice. Finally, the product was dried in vacuum at 40 °C for 12 h to obtain the white solid of [CMMIm]Cl.

5.2.3 Preparation of KOH-activated biocarbon (KWB) derived from sugarcane bagasse

KWB was obtained by KOH activation method according to the previous reported work [26] and the typical process as follows: first, sugarcane bagasse was cut into small pieces (opening size approximately 2 mm) and immersed in distilled water for 8 h at 90 °C, and then dried at 80 °C for 24 h. Second, 1 g clean sugarcane bagasse and 0.6 g KOH were poured into 12 ml absolute ethanol with stirring and heated at 60 °C until all of the ethanol was evaporated, and then dried at 70 °C for 12 h. Third, the remnant mixture was pyrolyzed in a tubular furnace in N₂ atmosphere at 800 °C (heating rate is 10 °C min⁻¹) for 2 h. Finally, the obtained carbon material was washed by 1 M HCl solution and deionized water till the filtrate became neutral and collected after vacuum dry.

5.2.4 Preparation of polyaniline/ activated biocarbon composites (PANI/KWB)

The PANI/KWB composites were prepared by in-site polymerization method. 5 g [CMMIm]Cl IL dissolved in 100 ml deionized water. Then add 1 ml An monomer and

0.1 g KWB (the mass ratio of An/KWB is 10:1) to the above solution. Subsequently, the mixture was sonicated for 0.5 h, and the APS solution (1.5 g APS dissolved in 10 ml of hydrochloric acid solution (1 M)) was added drop by drop to the mixture to start the polymerization. The reaction was performed with stirring at room temperature for 2 h. Finally, the product was removed from solution, washed with distilled water until pH=6-7, and dried in vacuum at 80 °C for 12 h to obtain the PANI/KWB-1 as black green powder. The other products were denoted as PANI/KWB-2, PANI/KWB-3, PANI/KWB-4 and PANI/KWB-5 for the mass ratios of An/KWB was 20:1, 30:1, 40:1 and 50:1 (the mass ratio of An monomer to ILs and APS was kept at 1:5:1.5), respectively. In addition, we also prepared pure PANI as control.

5.2.5 Synthesis of pure PANI without IL

For composite with the PANI via [CMMIm]Cl Brønsted acidic IL as dopant, the pure were prepared by the same method while used sulfamic acid (SA) as the dopant. Typically, 5 g SA dissolved in 100 ml deionized water, then 1 ml An monomer added the above solution. Subsequently, the mixture was ultrasonication for 0.5 h, and the APS solution (1.5 g APS dissolved in 10 ml of hydrochloric acid solution (1 M)) was by drop to the mixture to start the polymerization. The reaction was performed with stirring at room temperature for 2 h. Finally, the product was removed from solution, washed with distilled water until pH=6-7, and dried in vacuum at 80 °C for 12 h to obtain the pure PANI as black green powder.

5.2.6 Structure characterization

The morphology of samples were observed by transmission electron microscopy (TEM, H-8110, Hitachi Co., Ltd. Tokyo, Japan) and scanning electron microscopy (SEM, S-4300, Hitachi Co., Ltd. Tokyo, Japan). Nitrogen adsorption-desorption isotherms were measured at -196 °C on a Micromeritics ASAP 2020 apparatus. The specific surface area was calculated according to the Brunauer-Emmett-Teller (BET) equation. All samples were outgassed under vacuum at 80 °C overnight prior to

measurement. The chemical structures of the samples were confirmed by Fourier transform infrared spectroscopy (FTIR, IRT-7000, JASCO, Japan). The crystallographic structure of the samples was observed by X-ray diffraction (XRD, XRD-6000, Shimadzu Co., Ltd. Kyoto, Japan) equipped with Cu K α radiation. X-ray photoelectron spectroscopy (XPS) analysis was performed on the PHI Quantum 5000 equipped with an Al K α radiation source.

5.2.7 Electrochemical test

The electrochemical tests were measured with an electrochemical workstation (CHI 660D, Shanghai Chenhua, China) in the two or three-electrode system in 1 M Na₂SO₄ electrolyte. For three-electrode system, saturated calomel electrolyte and platinum-wire electrode were used as reference and counter electrode, respectively. The test electrodes were first prepared by mixing PANI/KWB composites with carbon black (CB) and PTFE at a mass ratio of 80:15:5. After that, the mixing were grinding adequately to obtained a homogeneous paste, that was coated onto the Ni foam for current collector and dried under vacuum at 80 °C for 24 h, and then compressed at 10 MPa for 5 min. The mass loading of active material in an electrode is about 8 mg. Cyclic voltammetry (CV), and galvanostatic charge/discharge (GCD) were conducted in a potential window from -0.8 to 0.2 V for AB, and -0.2 to 0.8 V for PANI/KWB composites, respectively. Electrochemical impedance spectroscopy (EIS) was carried out in the frequency range from 10⁵ to 10⁻² Hz at open circuit potential with as ac perturbation of 5 mV. The asymmetric two-electrode system was assembled with two almost identical working electrodes (the active material was PANI/KWB composites sample, and the counter electrode was KWB sample). The CV and GCD tests were run at different voltage windows.

The standard calomel reference electrode (SCE) based on GCD curves was evaluated according to the following equation (Eq. 1):

$$C_m = (I \times t) / (\Delta V \times m) \quad (\text{Eq. 1})$$

where I is discharge current (A), t is the discharge time (s), ΔV is the voltage window

(V), and m is the mass of active material on working electrode in three-electrode system, in two-electrode system is the total mass of active material on two working electrodes [29].

The energy density (E , Wh kg^{-1}) and power density (P , W kg^{-1}) of the asymmetric two-electrode system were calculated from the discharge curves according to the following equations [30]:

$$E = 1/2 C_m (\Delta V)^2 \quad (\text{Eq. 2})$$

$$P = E/t \quad (\text{Eq. 3})$$

where C_m , t and ΔV are the specific capacitance (F g^{-1}), discharge time (h) and potential window (V) from GCD curves in two-electrode system, respectively.

5.3 Results and discussion

5.3.1 Microstructural characterization

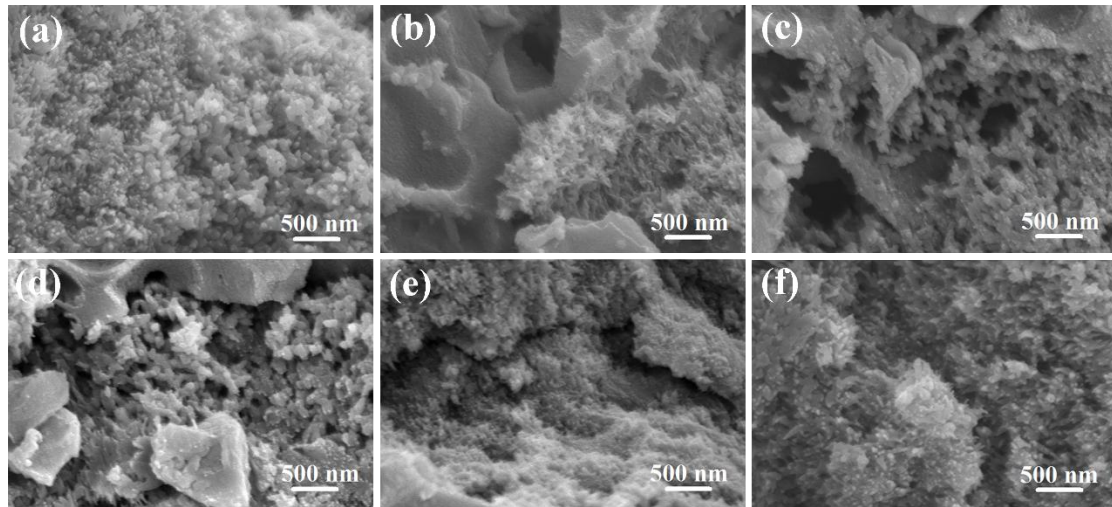


Fig. 5.1 SEM images of PANI (a), PANI/KWB-1 (b), PANI/KWB-2 (c), PANI/KWB-3 (d), PANI/KWB-4 (e) and PANI/KWB-5 (f) composites.

The morphology and microstructure of the prepared samples are shown in Fig. 5.1. As shown in Fig. 5.1a, PANI nanoparticles exhibit a coral-like structure and with a large number of conical protrusions (as shown in Fig. 5.2c and d). Compared with pristine KWB, the clean surface and interconnected frameworks of KWB (as shown in Fig. 5.2a

and b) were gradually covered by PANI nanoparticles with the mass ratios of An/KWB increased. It is noteworthy that the surface and frameworks of KWB were completely covered by PANI nanoparticles (as shown in Fig. 5.1e) when the mass ratio of An/KWB is 40:1.

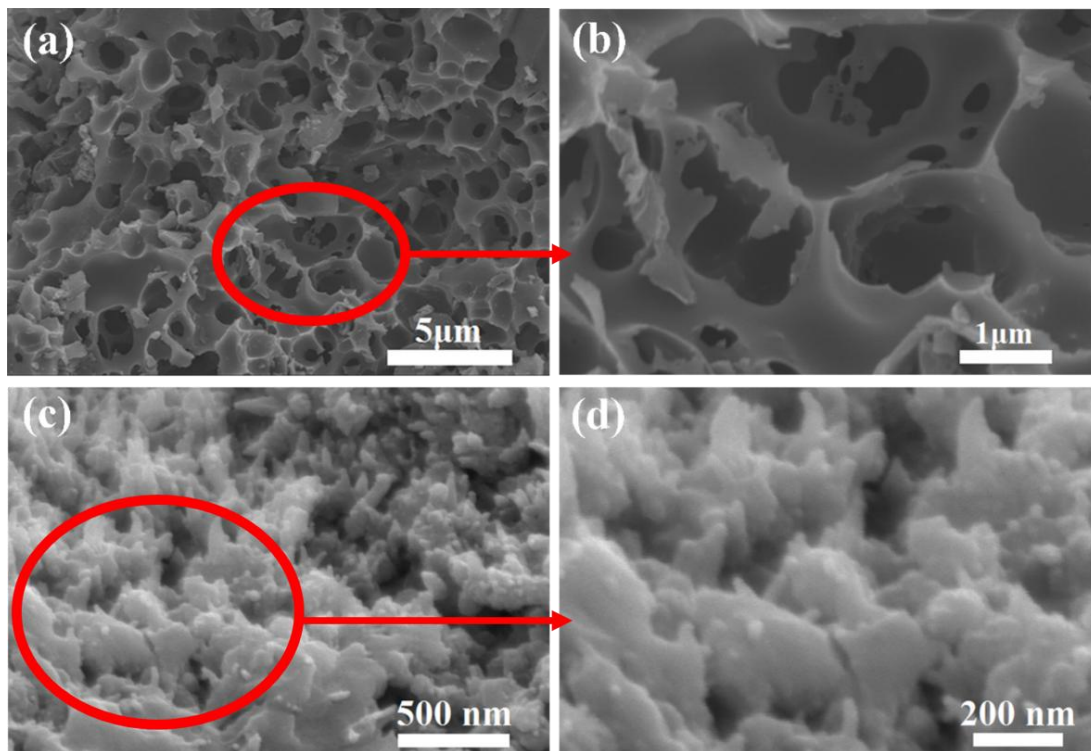


Fig. 5.2 SEM images of AB (a-b) and PANI (c-d)

For compare with PANI/KWB composites, the SEM of KWB and PANI shown in Fig. 5.2. The morphology of KWB is hierarchical porous structure (as shown in Fig. 5.2a and b). It is clearly observed that there are a large number of nano-scale pores on the inner wall of the micron-sized macropores, and the surface of KWB is smooth.

The morphology of PANI/KWB-4 was further investigated by TEM. It can be clearly seen that the surface of KWB is coated by PANI as shown in Fig. 5.3a. Moreover, the conical projection corresponding to SEM image of PANI was also observed (as shown in Fig. 5.3b). In addition, for PANI/KWB-5 (Fig. 5.1f), the porous structure of KWB completely disappeared, which means that the porous structure of KWB was filled by PANI nanoparticles. The above phenomena may impact electrochemical performance of PANI/KWB composites profoundly.

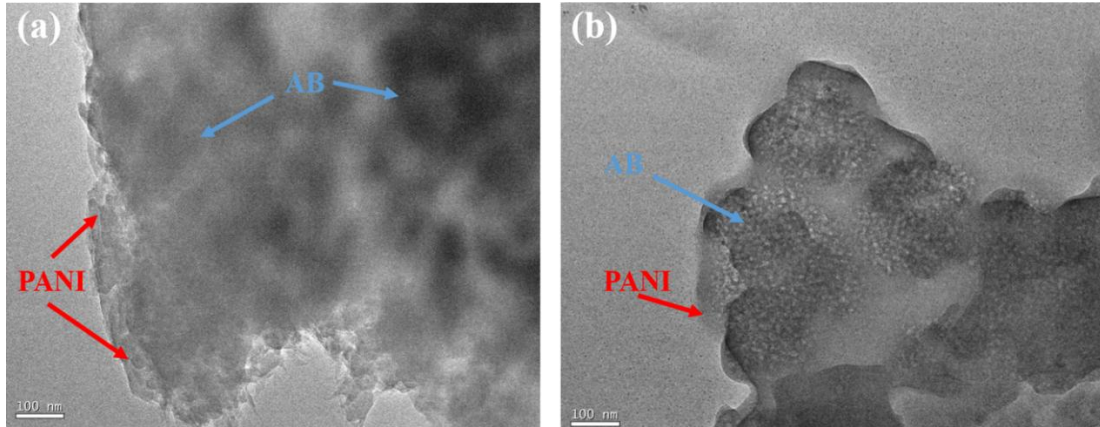


Fig. 5.3 TEM images of PANI/KWB-4 composites

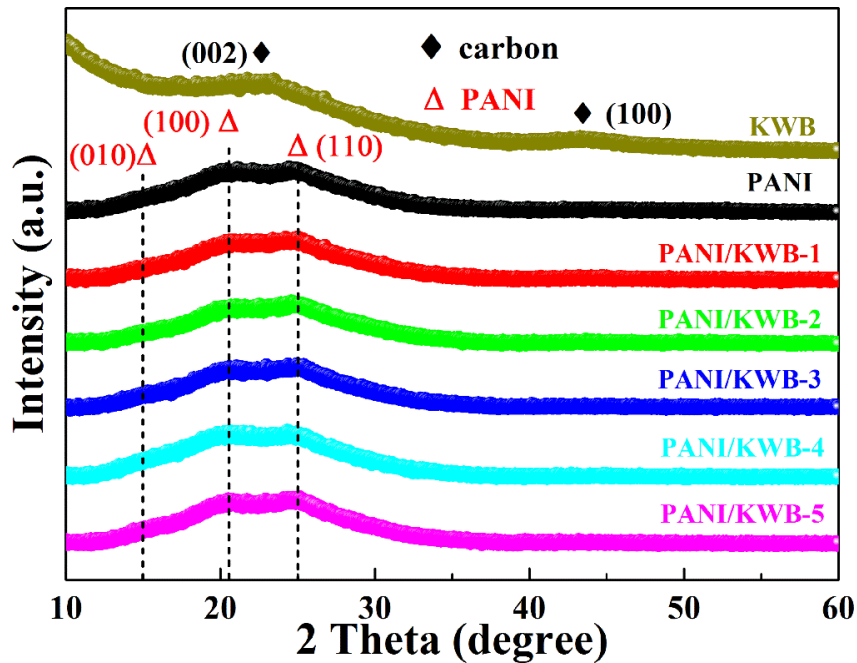


Fig. 5.4 X-ray diffraction patterns of the prepared KWB, PANI and PANI/KWB composites.

The crystallinity of the samples was examined by X-ray diffraction analysis. Fig. 5.4 shows the XRD patterns of KWB, PANI and PANI/KWB composites. For KWB, a broad diffraction peak centered at 24.5° correspond to the (002) plane of graphite, arising from the amorphous nature of graphite [31]. Furthermore, a weak diffraction peak can be observed at 43.4° corresponding to graphite (100), which means of the complete transformation of sugarcane bagasse to another kind of activated carbon [32]. For pure PANI, three broad diffraction peaks at 15, 20.4 and 25° were correspond to the

(010), (100), and (110) plane of PANI, respectively [33], and these peaks suggest a poor crystallinity and partially crystalline of the PANI [34]. The characteristic peaks of PANI/KWB are exactly the same as those of pure PANI, indicating that PANI nanoparticles covered on the surface of KWB.

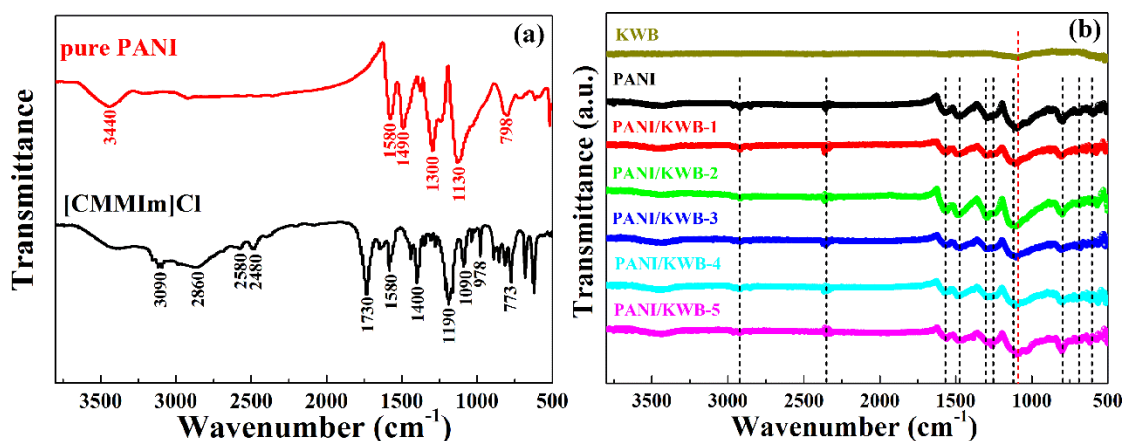


Fig. 5.5 FT-IR spectra of the prepared pure PANI and [CMMIm]Cl (a), and AB biocarbon, PANI and PANI/KWB (b) composites .

For [CMMIm]Cl sample (as shown in Fig. 5.5a), the peaks at 3090 cm^{-1} is attributed to the overlap peaks of the V=C-H stretching of the imidazole ring and the hydroxyl groups of carboxylic acid. The peaks at 2861 cm^{-1} correspond to the saturation C-H stretching mode. The peaks at $2580, 2480\text{ cm}^{-1}$ are attributed to the characteristic C-N and C=N stretching of the imidazole rings. The peak at $1730, 1650$ and 1580 cm^{-1} are the characteristic of carbonyl group, the C-N and C=N of the imidazole rings, respectively. Band located around 1400 cm^{-1} are C=C and C-C stretching. The peak at 1190 cm^{-1} is the C-O stretching. The peak at 1090 cm^{-1} is attributed to O-H out-of-plane bending. In addition, Bands around 978 and 773 cm^{-1} are attributed to C-H in-plane and out-of-plane bending [27]. For pure PANI sample (as shown in Fig. 5.5a), the absorption band at 3440 cm^{-1} is the associating hydroxyl groups. The bands at 1580 and 1490 cm^{-1} are attributed to the characteristic N=Q=N stretching of the quinoid, N-B-N of the benzenoid, and band centered at 1300 cm^{-1} correspond to N-H bending and asymmetric C-N stretching modes of the benzenoid ring. Bands around 1130 and 798

cm^{-1} are attributed to C–H in-plane and out-of-plane bending of aniline rings in protonation [36].

The chemical structure of KWB, PANI and PANI/KWB composites were characterized by FT-IR spectra (as shown in Fig. 5.5b). In the spectra of KWB, the peak at 1099 cm^{-1} was for C–O group, and this group formed during the bagasse pyrolysis and activation process [35]. In the spectra of PANI, the peak at 1115 cm^{-1} assigned to the C–H in-plane stretching of the quinoid. Other peaks are assigned as follows: saturation C–H stretching peak at 2921 cm^{-1} , C–N and C=N stretching of the imidazole ring peak at 2358 cm^{-1} , N=Q=N stretching of the quinoid peak at 1567 cm^{-1} , N–H bending of the benzenoid ring peak at 1261 cm^{-1} , and C–H in-plane bending of aniline ring peak at 796 cm^{-1} [36, 37]. Once KWB composited with PANI, the feature peak of KWB will overlap with the peak of PANI (peak at 1115 cm^{-1}), and the other feature peak of PANI will still existed. It further suggests that PANI nanoparticles covered on the surface of KWB.

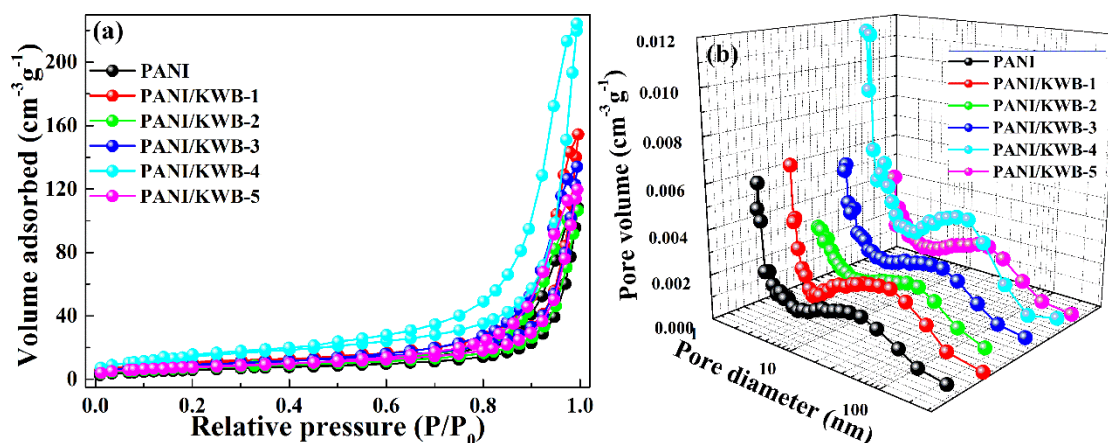


Fig. 5.6 N_2 adsorption-desorption isotherms (a) and pore size distribution by BJH method (b) of the prepared PANI and PANI/KWB-1, PANI/KWB-2, PANI/KWB-3, PANI/KWB-4 and PANI/KWB-5 composites.

The nitrogen adsorption/desorption isotherm for the PANI and PANI/KWB composites and their corresponding pore size distribution are shown in Fig. 5.6. For PANI, its isotherm can be classified as a type III isotherm with a type H3 hysteresis,

suggesting the non-porous structure [38]. The KWB display type I isotherms with a type H2 hysteresis (as shown in Fig. 5.7a) and possess a particularly high specific surface area ($1433.06 \text{ m}^2 \text{ g}^{-1}$, as shown in Table 5.1), indicating the polyporous structure [39]. For PANI/KWB composites, the PANI nanoparticles covered on the surface of KWB and will block the porous structure of KWB. Possibly, the S_{BET} of PANI/KWB will be lower than KWB, and the P will be changed.

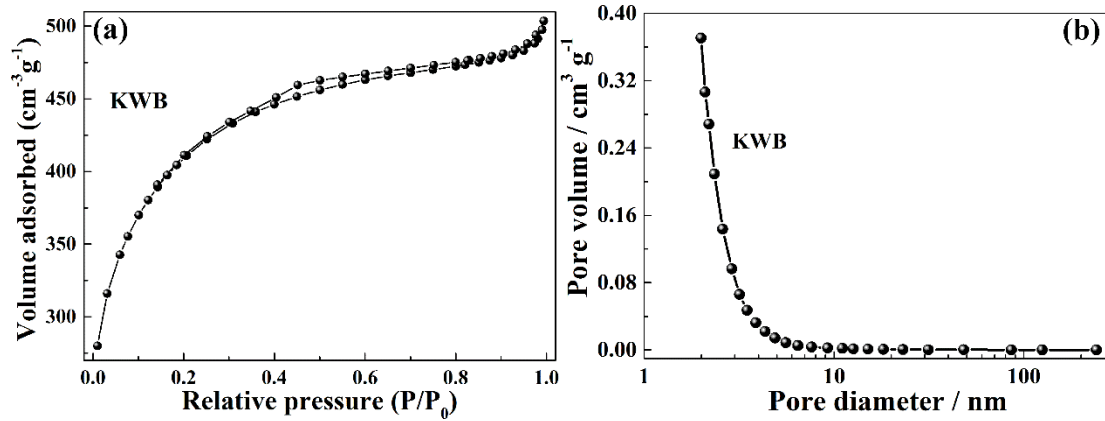


Fig. 5.7 N_2 adsorption-desorption isotherms (a) and pore size distribution by BJH method (b) of the prepared KWB.

Table 5.1 Specific surface area, pore size of samples. (S_{BET} - the specific surface area; S_{mi} - the micropore specific surface area; P - the main pore size; V_t - the total pore volume)

Sample	S_{mi} ($\text{m}^2 \text{ g}^{-1}$)	S_{BET} ($\text{m}^2 \text{ g}^{-1}$)	V_t ($\text{cm}^3 \text{ g}^{-1}$)	P (nm)
KWB	634.88	1433.06	0.775	3.03
PANI	--	22.58	0.093	20.58
PANI/KWB-1	5.10	36.82	0.130	23.94
PANI/KWB-2	--	25.6539	0.109	19.03
PANI/KWB-3	--	33.58	0.123	19.6
PANI/KWB-4	--	54.47	0.234	18.58
PANI/KWB-5	--	28.57	0.117	19.32

The S_{BET} and P of PANI/KWB can be influenced by the mass ratio of An/KWB. As shown in Table 1, the S_{BET} of PANI/KWB was increased first and then decreased with

the mass ratio of An/KWB increased. On the contrary, the P of PANI/KWB was decreased first and then increased with the mass ratio of An/KWB increased. When the mass ratio of An/KWB reached to 40:1 (PANI/KWB-4), the S_{BET} of PANI/KWB showed the maximum value of $54.47 \text{ m}^2 \text{ g}^{-1}$. In addition, the S_{BET} of PANI/KWB is higher than that of PANI and much smaller than that of KWB, which indicating that the polyporous structure of KWB is conducive to improving the S_{BET} of electrode material. Moreover, only PANI/KWB-1 has a S_{mi} , which is due to part of surface and porous structure of KWB is covered by PANI nanoparticles when the mass ratio of An/KWB is 10. Soon afterwards, the surface and porous structure of KWB is completely covered by PANI nanoparticles with the increase of the mass ratio of An/KWB, which has been proved by SEM images. However, the S_{BET} of KWB will be close to pure PANI and the support function of KWB will lose when the mass ratio of An/KWB is too large (more than 40), which is owing to KWB buried by a large number of PANI nanoparticles. Nevertheless, the S_{BET} of PANI/KWB-4 can still reach up to $54.47 \text{ m}^2 \text{ g}^{-1}$ (much higher than that of pure PANI). This acceptable S_{BET} of PANI/KWB-4 has an enough promise to be electrode material for supercapacitors application.

Table 5.2 XPS spectrum analysis of samples

Sample	C/at. %	N/at. %	O/at. %
KWB	84.76	--	15.24
PANI	81.11	8.28	10.61
PANI/KWB-1	80.58	8.13	11.28
PANI/KWB-2	81.24	8.95	9.81
PANI/KWB-3	80.98	8.75	10.27
PANI/KWB-4	80.63	8.87	10.50
PANI/KWB-5	81.08	8.04	10.88

The information of the surface chemical composition of samples was obtained from XPS spectra. The full scan spectra of samples are shown in Fig. 5.7a. Compared with KWB, the XPS spectra of PANI/KWB composites added a signal of N element. In addition, the signal of O element of PANI spectra indicates that the [CMMIm]⁺ (contain

-COOH) as the cationic of IL were doped into the molecular chain of PANI.

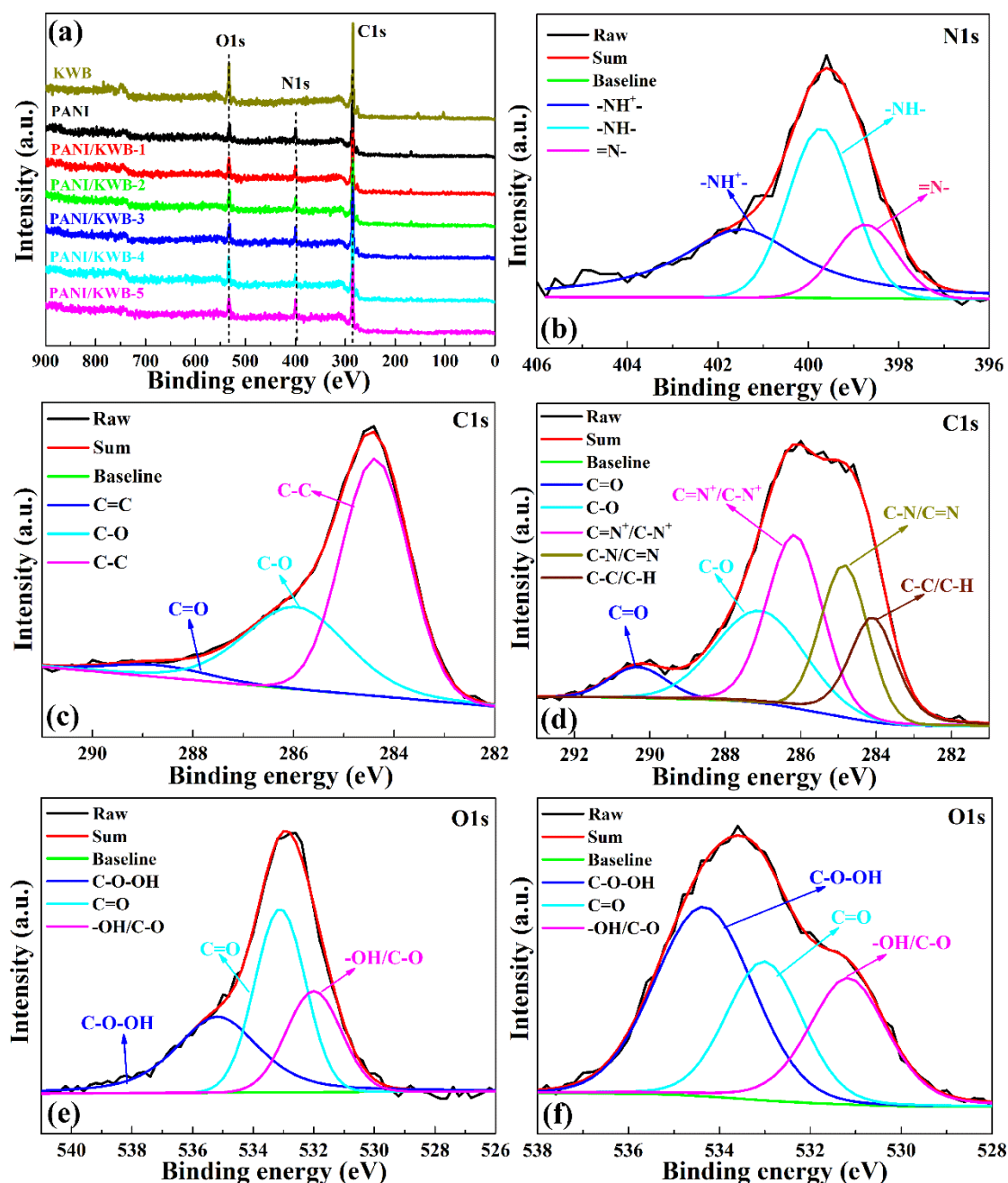


Fig. 5.8 XPS survey spectra of KWBBiobarbon, PANI and PANI/KWB composites (a); high resolution C1s (c) and O1s (e) XPS spectra of KWBBiobarbon; high resolution N1s (b), C1s (d) and O1s (f) XPS spectra of PANI/KWB-4 composite.

More information about the change of surface chemistry has been obtained by the deconvoluted high-resolution XPS spectra of three regions (C, O and N, as shown in Fig. 5.8). The C1s spectra of KWBBiobarbon could be deconvoluted into three peaks (as shown

in Fig. 5.8c) with binding energies of 531.5, 533.2 and 534.8 eV. These peaks could be assigned to aromatic or other sp^2 -hybridised carbon atoms bound to neighboring carbon atoms (C-C, 284.4 eV), carbon in C-O (285.8 eV) and C=O (288.8 eV), respectively [40]. Compared with KWB, except for the above three peaks in C1s spectra of PANI/KWB-4 (as shown in Fig. 5.8d), the other new peaks appeared in 286.2 and 284.8 eV, can be attributed to $C=N^+/C-N^+$ and C-N/C=N, respectively [41]. The N1s spectra of PANI/KWB-4 (as shown in Fig. 5.8b) could be deconvoluted into three components. The peaks of 401.5, 399.7 and 398.7 eV can be attributed to cationic atoms ($-N^+$), amine ($-NH-$) and imine ($=N-$), respectively [42]. The O1s spectra of KWB and PANI/KWB-4 in Fig. 5.8e and f can be deconvoluted into three components. The peaks of 531.5, 533.2 and 534.8 eV can be assigned to $-OH/C-O$, C=O and C-O-OH groups, respectively [43]. Obviously, the content of C-O-OH group in PANI/KWB-4 is much higher than that of AB, which is also owing to the $[CMMIm]^+$ doped into the molecular chain of PANI. The high content of C-O-OH group in PANI/KWB-4 has a meaningful impact on electrochemical performance of composites.

5.3.2 Electrochemical performance of PANI/KWB composites

To explore potential applications of the PANI/KWB composites to supercapacitors, we first performed the CV, GCD and EIS measurements in a three-electrode configuration. Fig. 5.9 shows the CV curves of PANI and PANI/KWB composites at a scan rate of 0.01 V s⁻¹. The CV curve of KWB shows nearly symmetric rectangular shape (as shown in Fig. 3.11), indicating an ideal double-layer capacitor behavior [44]. Different from CV curve of KWB, both the CV curves of PANI and PANI/KWB composites deviate from the rectangular shape, due to the charge storage process of PANI-based material. In the CV curves of PANI/KWB composites, the pairs of peaks P1/P2 (the weak peak of P1 as shown in the dark green circle of Fig. 5.9) are attributed to the redox of PANI molecules (leucoemeraldine and pernigraniline species), and the other pairs of peaks P3/P4 are ascribed to benzoquinone/hydroquinone redox transitions [44]. The PANI/KWB-4 shows the larger area enclosed by the CV curve than that of

the PANI and PANI/KWB, revealing the highest specific capacitance (SC).

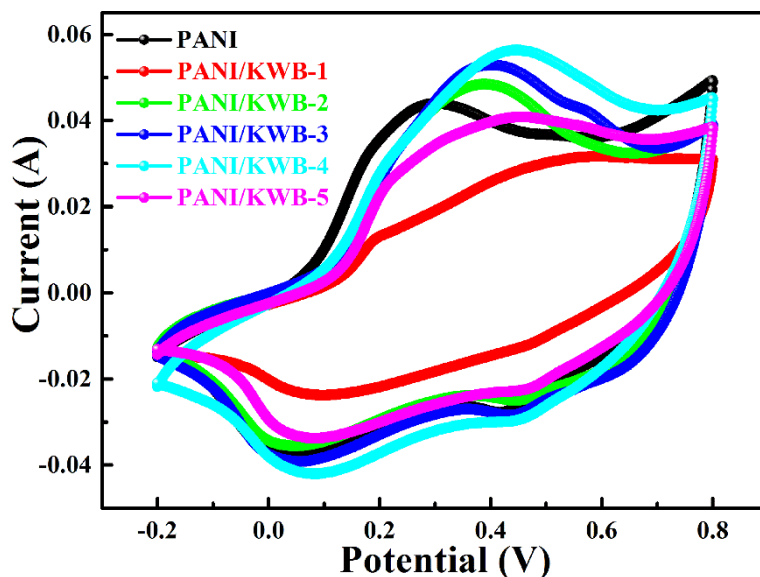


Fig. 5.9 CV curves of PANI and PANI/KWB composites at scan rate of 0.01 V s^{-1}

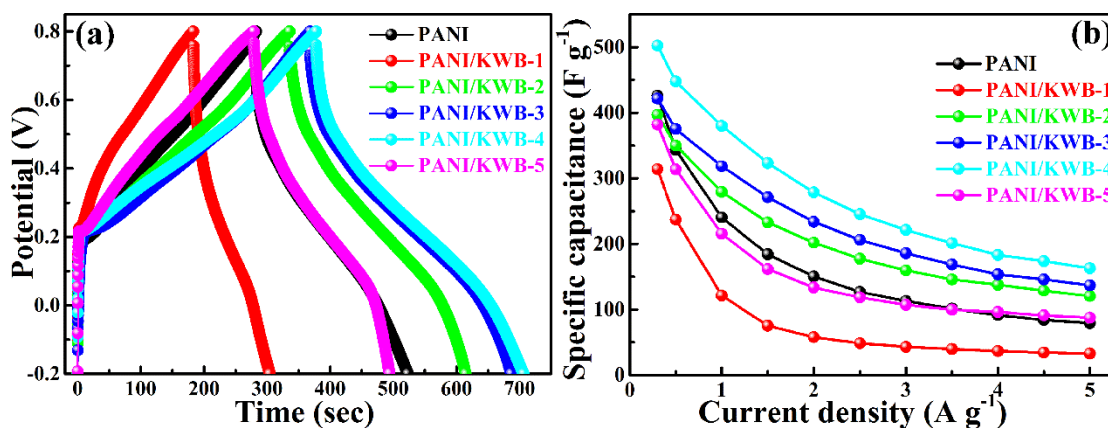


Fig. 5.10 GCD curves (a, at current density of 1 A g^{-1}) and specific capacitance (b, versus current density) of PANI and PANI/KWB composites.

The enhancement of the SC is also confirmed by the GCD curves, as shown in Fig. 5.10a. The SC of the PANI and PANI/KWB at various current densities is calculated from the discharge curves and the results were shown in Fig. 5.10b. In general, the SC of all samples decreases with the increase of current density. The SC of PANI, PANI/KWB-1, 2, 3, 4 and 5 are $343, 236, 350, 375, 447$ and 323 F g^{-1} , respectively, at a current density of 0.5 A g^{-1} . The SC of PANI/KWB composites first increases and

then decreases with the increase of the An/KWB mass ratio. These results are further evidences for the inference from CV curves. Furthermore, the SC of PANI/KWB-4 is higher than that of the other PANI/KWB composites at various current densities. This is due to S_{BET} of PANI/KWB-4 is bigger than that of the other samples, resulting in the contact area of PANI/KWB-4 and electrolyte being biggest among all samples.

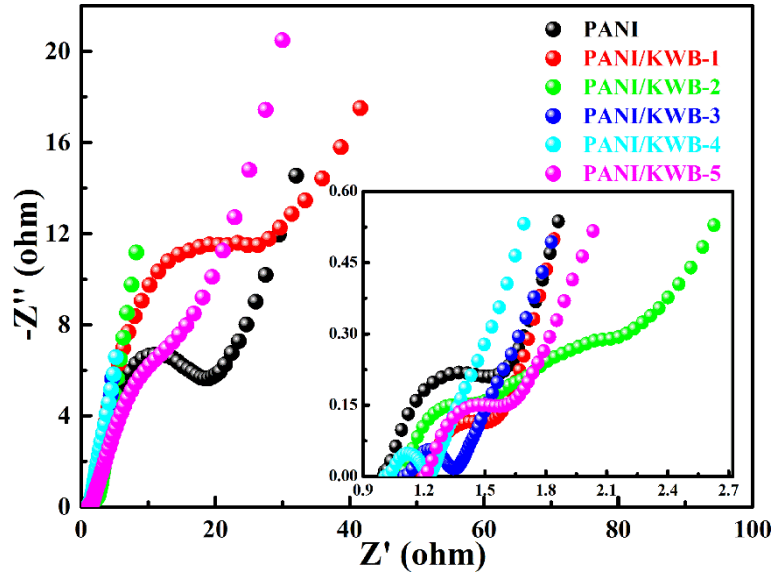


Fig. 5.11 EIS curves of PANI and PANI/KWB composites.

To further study the capacitive behavior samples, EIS was used to measure the charge transport and ion diffusion. The Nyquist plots of PANI and PANI/KWB are showed in Fig. 5.11. In EIS curve, the internal resistance (R_s , including the intrinsic resistance of the sample, the contact resistance between the sample and current collector, and the resistance of bulk electrolyte) can be obtained from the point intersecting with the real axis in the region of high frequency. The semicircle is due to the charge transfer and which will affect capacitive behavior at high current loading [45]. The inset shows that R_s of PANI/KWB-1, 2, 3, 4 and 5 are 1.19, 1.09, 1.10, 1.01 and 1.20 Ω , respectively. It is worth noting that R_s of PANI/KWB-4 is lower than those of PANI/KWB composites. The semicircle radius of PANI/KWB-4 is lower than the other samples, means that the PANI/KWB-4 possesses the lowest charge resistance among PANI/KWB composites. Moreover, the nearly vertical line at lower frequency of PANI/KWB-4 indicates the

pure capacitor behavior as an ideal capacitor [46, 47]. In short, the analyses of EIS reveal that PANI/KWB-4 sample possesses an excellent capacitive performance, and this result agrees with the analyses of GCD and CV.

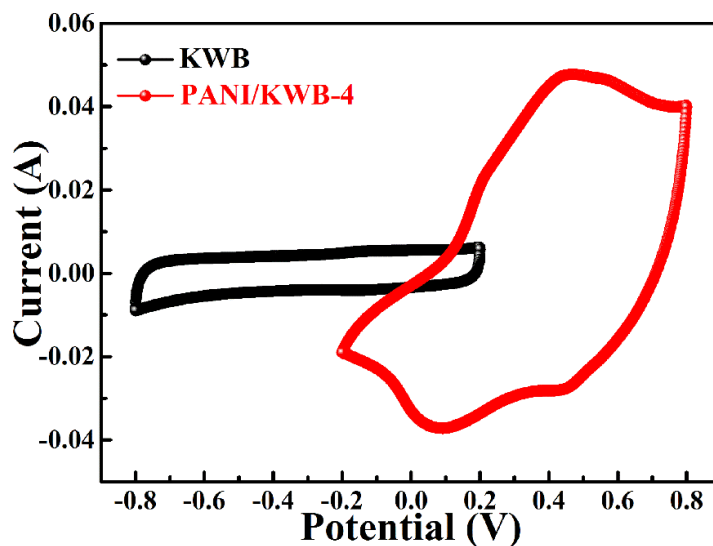


Fig. 5.12 CV curves of KWB and PANI/KWB-4 in three-electrode asymmetric system at a scan rate of 0.01 V s^{-1} (a)

In order to further evaluate the potential application of PANI/KWB in supercapacitors, an asymmetric two-electrode system with the PANI/KWB-4 as the positive electrode and the KWB as the negative electrode is assembled (the two-electrode system denoted as PANI/KWB-4//KWB). The voltage window is a key factor for two-electrode system, for it can impact the energy density of supercapacitors [48]. In three-electrode system, the stable potential window of KWB is $-0.8 \sim 0.2 \text{ V}$, while PANI/KWB-4 is stable between $-0.2 \sim 0.8 \text{ V}$ (as shown in Fig. 5.12). Accordingly, it is expected that the potential window of PANI/KWB-4//KWB can be extended up to 1.6 V .

The comparative CV curves of PANI/KWB-4//KWB at different voltage windows were measured at a scan rate of 0.01 V s^{-1} to evaluate the optimized voltage window (as shown in Fig. 5.13a). It can be found that all CV curves exhibit a rectangular shape when the voltages are below 1.6 V . There is no significant increase of anodic current even when voltage reach to 1.6 V , which mean that the electrolyte is not being decomposed due to the storage of nascent hydrogen on the electrode below the

thermodynamic potential for water decomposition [49]. Furthermore, a redox peak appears at 1.5 V in CV curve when voltage is 1.6 V, indicating that the electric double-layer capacitance and pseudocapacitance simultaneously exist. The SC of PANI/KWB-4//KWB calculated from GCD curves at 1 A g^{-1} at different voltage windows are displayed in Fig. 7c. The SC increases from 57 to 77 F g^{-1} as the voltage window increase from 1.0 to 1.6 V. The GCD curve still maintains nearly symmetric even at 1.6 V, suggesting the fast current response and small resistance [50]. These above data analyses show that the best voltage window of PANI/KWB//KWB is 0~1.6 V.

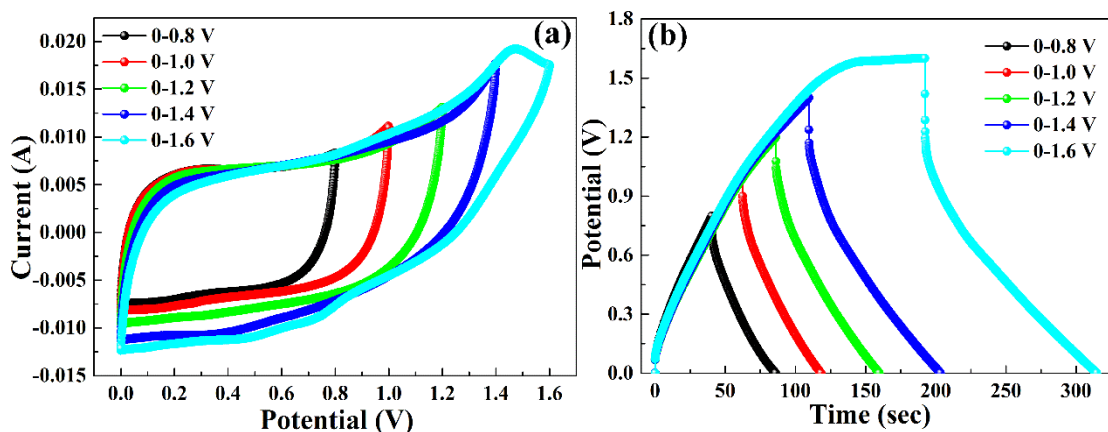


Fig. 5.13 CV (a, scan rate of 0.01 V s^{-1}) and GCD (b, current density of 1 A g^{-1}) curves of two-electrode asymmetric system (using PANI/KWB-4 and KWB as the positive and negative electrode, respectively) at different potential windows;

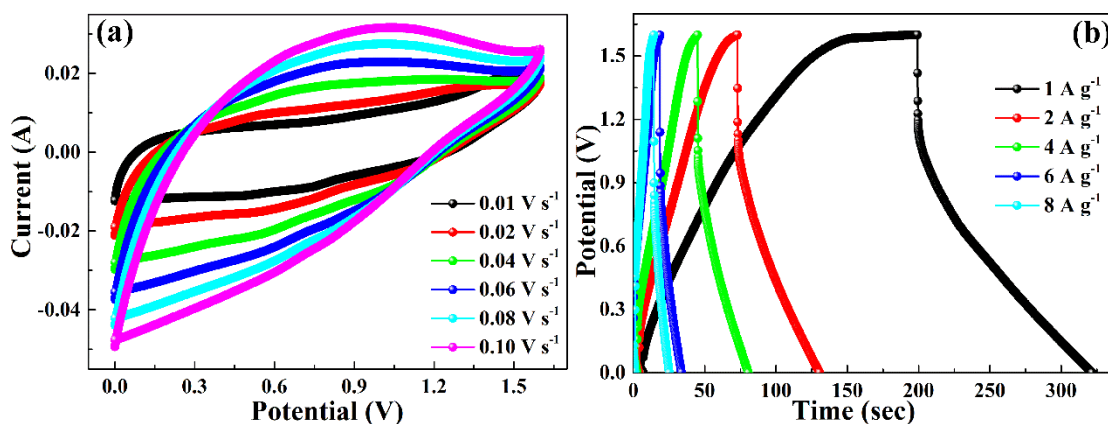


Fig. 5.14 CV (a) and GCD (b) curves of asymmetric system measured at different scan rates and current densities in a potential window of 1.6 V, respectively (using PANI/KWB-4 and KWB as the positive and negative electrode, respectively).

The CV curves of PANI/KWB-4//KWB at different scan rates (0.01~0.1 V s⁻¹) measured between 0~1.6 V are displayed in Fig. 5.14. The current increases as the scan rate increases, while its shape gradually deviate from the rectangular shape, which suggests that the PANI/KWB-4//KWB gradually deviate from the ideal capacitive behavior with the scan rate increase. GCD measurements were made at different current densities to further evaluate the capacitive performance of the PANI/KWB-4//KWB at the voltage window of 0~1.6 V, as shown in Fig. 5.14. The SC of the PANI/KWB-4//KWB is also obtained from GCD curves. The SC is 77 F g⁻¹ at a current density of 1 A g⁻¹, and still maintains at 55 F g⁻¹ when the current density increases to 8 A g⁻¹.

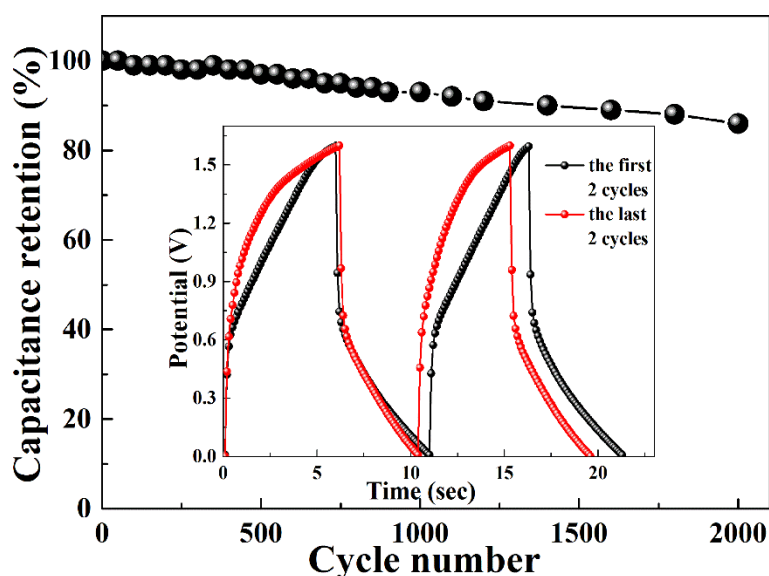


Fig. 5.15 Cycle stability of asymmetric system (using PANI/KWB-4 and KWB as the positive and negative electrode, respectively).

The long-term cycling stability is an essential property of Supercapacitors. The cycle stability of the PANI/KWB-4//AB is evaluated by the GCD test in a voltage window of 0~1.6 V at a current density of 8 A g⁻¹ for 2000 cycles (as shown in Fig. 8f). The PANI/KWB-4//KWB retains about 87% of the initial SC after 2000 cycles, which is comparable to those of other polymer-based asymmetric or symmetric two-electrode system, including PANI/MnO₂/carbon//activated grapheme (70% retention after 5000 cycles) [51], PANI/RGO//PANI/RGO (85% retention after 1000 cycles) [52] ,

graphene/RuO₂//graphene/PANI (70% retention after 2500 cycles) [53], RGO–PANI//RGO–PANI (80% retention after 1000 cycles) [54], manganese dioxide/reduced graphene oxide/indium tin oxide (MRI)//polypyrrole/reduced graphene oxide/indium tin oxide (PRI) (75% retention after 2000 cycles) [55], and 3D-hollow balls of graphene and polyaniline (HBGP)//3D-HBGP (86% retention after 500 cycles) [56].

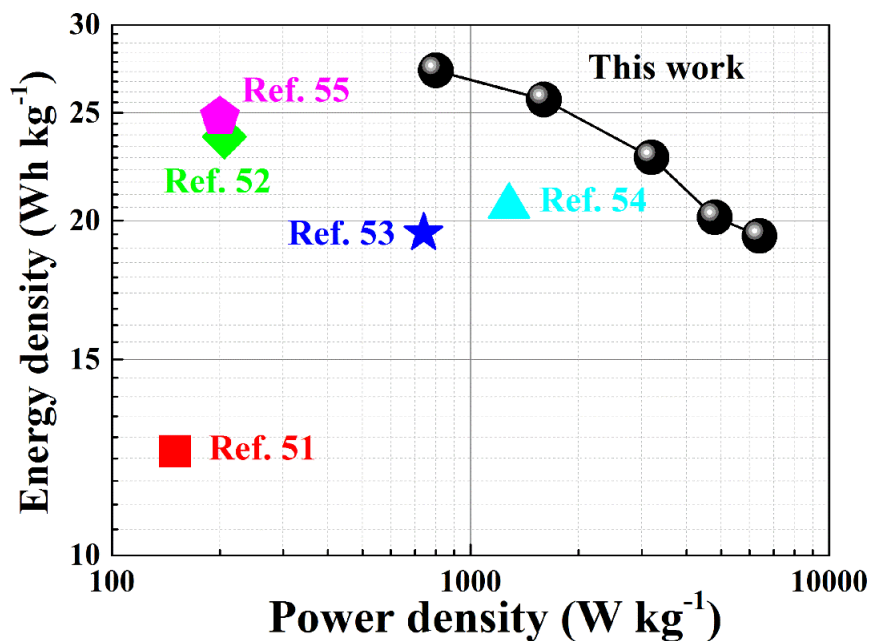


Fig. 5.16 Ragone plot of asymmetric system (using PANI/KWB-4 and KWB as the positive and negative electrode, respectively).

Supercapacitors with excellent performance, the high power and energy density are expected. The energy and power density of the PANI/KWB-4//KWB are calculated from the GCD curves according to Eqs. (2) and (3), and the results of Ragone plots are shown in Fig. 8. Basically, the energy density of PANI/KWB-4//KWB decreases gradually with the power density increases. The maximum energy density is 27.29 Wh kg⁻¹ at a power density of 800 W kg⁻¹ and still maintains 19.38 Wh kg⁻¹ at a ‘power density of 6400 W kg⁻¹. These values are superior to the previous reported that of majority asymmetric or symmetric devices, such as RGC-RuO₂//RGO-PANI (26.3 Wh kg⁻¹, 150 W kg⁻¹) [54], RGC-PANI//RGO-PANI (13.9 Wh kg⁻¹, 150 W kg⁻¹) [54], PANI/CMK-3//CMK-3 (23.8 Wh kg⁻¹, 206 W kg⁻¹) [57], graphene-wrapped PANI

nanofibers//activated carbon (19.5 Wh kg⁻¹, 738.9 W kg⁻¹) [58], layered PPy fibre//graphene film (20.6 Wh kg⁻¹, 1.28 kW kg⁻¹) [50], CNT/MnO₂/GR//CNT/PANI (24.8 Wh kg⁻¹, 200 W kg⁻¹) [59], XC-72// rGO/CNT/PPy (14.3 Wh kg⁻¹, 6.62 kW kg⁻¹) [60], and Co(OH)₂/NEMG//PPy/rG-O (24.9 Wh kg⁻¹, 224 W kg⁻¹) [61]. These findings suggest the PANI/KWB-4//KWB holds a great promise in the practical application.

5.4 Conclusions

In this work, PANI/KWB composites were synthesized via in-site polymerization method. In this synthesis process, KWB (derived from the biomass waste of sugarcane bagasse) and [CMMIm]Cl IL acted as the scaffolds for PANI growth and paint, respectively. The electrochemical performance of PANI/KWB was closely related to the mass ratio of An/KWB. PANI/KWB-4 showed the best electrochemical performance when the mass ratio of An/KWB was 40 in three-electrode system. In addition, the assembled asymmetric two-electrode system based on PANI/KWB-4 and KWB exhibits high energy density (27.29 Wh kg⁻¹), high power density (800 W kg⁻¹) and excellent cycling stability of 87% SC retention after 2000 cycles within the voltage window of 0~1.6 V. The PANI/KWB composites synthesized with facile and low cost method shows an excellent electrochemical performance, marking it a promising candidate in energy storage devices.

References

- [1] G. Wang, L. Zhang, J. Zhang, A review of electrode materials for electrochemical supercapacitors, *Chem. Soc. Rev.* 41 (2012) 797-828.
- [2] Z. Fan, J. Yan, T. Wei, L. Zhi, G. Ning, T. Li, F. Wei, Asymmetric Supercapacitors Based on Graphene/MnO₂ and Activated Carbon Nanofiber Electrodes with High Power and Energy Density, *Adv. Funct. Mater.* 21 (2011) 2366-2375.
- [3] M. Shao, Z. Li, R. Zhang, F. Ning, M. Wei, D.G. Evans, Hierarchical Conducting Polymer @ Clay Core – Shell Arrays for Flexible All-Solid-State Supercapacitor Devices, *Small.* 11 (2015) 1-9.
- [4] P. Shi, L. Li, L. Hua, Q. Qian, P. Wang, J. Zhou, G. Sun, W. Huang, Design of Amorphous Manganese Oxide@Multiwalled Carbon Nanotube Fiber for Robust Solid-State Supercapacitor, *ACS Nano.* 11 (2017) 444-452.
- [5] Y. Zhai, Y. Dou, D. Zhao, P.F. Fulvio, R.T. Mayes, S. Dai, Carbon materials for chemical capacitive energy storage, *Adv. Mater.* 23 (2011) 4828-4850.
- [6] M. Huang, F. Li, F. Dong, X. Zhang, L. Li, MnO₂-based nanostructures for high-performance supercapacitors, *J. Mater. Chem. A Mater. Energy Sustain.* 3 (2015) 21380-21423.
- [7] A.G. Macdiarmid, J.C. Chiang, A.F. Richter, A.J. Epstein, Polyaniline: a new concept in conducting polymers, *Synth. Met.* 18 (1987) 285-290.
- [8] R. Mathew, D. Yang, B.R. Mattes, M.P. Espe, Effect of Elevated Temperature on the Reactivity and Structure of Polyaniline, *Macromolecules.* 35 (2002) 7575-7581.
- [9] S. Bhadra, D. Khastgir, N.K. Singha, J.H. Lee, Progress in preparation, processing and applications of polyaniline, *Prog. Polym. Sci.* 34 (2009) 783-810.
- [10] H. Zhang, Q. Zhao, S. Zhou, N. Liu, X. Wang, J. Li, F. Wang, Aqueous dispersed conducting polyaniline nanofibers: Promising high specific capacity electrode materials for supercapacitor, *J. Power Sources.* 196 (2011) 10484-10489.
- [11] Y. Li, X. Zhao, Q. Xu, Q. Zhang, D. Facile preparation and enhanced capacitance of Polyaniline/sodium alginate nanofiber networks for supercapacitors, *Chen, Langmuir.* 2 (2011) 2-6.

- [12]J. Zhang, X.S. Zhao, Conducting polymers directly coated on reduced graphene oxide sheets as high-performance supercapacitor electrodes, *J. Phys. Chem. C*. 116 (2012) 5420-5426.
- [13]C. Tran, R. Singhal, D. Lawrence, V. Kalra, Polyaniline-coated freestanding porous carbon nanofibers as efficient hybrid electrodes for supercapacitors, *J. Power Sources*. 293 (2015) 373-379.
- [14]S. Bose, T. Kuila, A.K. Mishra, R. Rajasekar, N.H. Kim, J.H. Lee, Carbon-based nanostructured materials and their composites as supercapacitor electrodes, *J. Mater. Chem.* 22 (2012) 767-784.
- [15]A. Ameli, M. Arjmand, P. Pötschke, B. Krause, U. Sundararaj, Effects of synthesis catalyst and temperature on broadband dielectric properties of nitrogen-doped carbon nanotube/polyvinylidene fluoride nanocomposites, *Carbon*. 106 (2016) 260-278.
- [16]X. Jin, W. Zhou, S. Zhang, G.Z. Chen, Nanoscale Microelectrochemical Cells on Carbon Nanotubes, *Small*. 3 (2007) 1513-1517.
- [17]Z. Spitalsky, D. Tasis, K. Papagelis, C. Galiotis, Carbon nanotube-polymer composites: Chemistry, processing, mechanical and electrical properties, *Prog. Polym. Sci.* 35 (2010) 357-401.
- [18]Y. Gao, L. Li, Y. Jin, Y. Wang, C. Yuan, Y. Wei, G. Chen, J. Ge, H. Lu, Porous carbon made from rice husk as electrode material for electrochemical double layer capacitor, *Appl. Energy*. 153 (2015) 41-47.
- [19]X. Ma, F. Zhang, J. Zhu, L. Yu, X. Liu, Preparation of highly developed mesoporous activated carbon fiber from liquefied wood using wood charcoal as additive and its adsorption of methylene blue from solution, *Technol.* 164 (2014) 1-6.
- [20]L. Jiang, J. Yan, L. Hao, R. Xue, G. Sun, B. Yi, High rate performance activated carbons prepared from ginkgo shells for electrochemical supercapacitors, *Carbon*. 56 (2013) 146-154.
- [21]X. Liu, M. Zhang, D. Yu, T. Li, M. Wan, H. Zhu, M. Du, J. Yao, Functional materials from nature: honeycomb-like carbon nanosheets derived from silk cocoon

- as excellent electrocatalysts for hydrogen evolution reaction, *Electrochim. Acta.* 215 (2016) 223-230.
- [22] Y.-T. Li, Y.-T. Pi, L.-M. Lu, S.-H. Xu, T.-Z. Ren, Hierarchical porous active carbon from fallen leaves by synergy of K_2CO_3 and their supercapacitor performance, *J. Power Sources.* 299 (2015) 519-528.
- [23] X. Du, W. Zhao, Y. Wang, C. Wang, M. Chen, T. Qi, C. Hua, M. Ma, Preparation of activated carbon hollow fibers from ramie at low temperature for electric double-layer capacitor applications, *Bioresour. Technol.* 149 (2013) 31-37.
- [24] J.M.V. Nabais, J.G. Teixeira, I. Almeida, J.M. Valente Nabais, J.G. Teixeira, I. Almeida, Development of easy made low cost bindless monolithic electrodes from biomass with controlled properties to be used as electrochemical capacitors, *Bioresour. Technol.* 102 (2011) 2781-2787.
- [25] A.E. Ismanto, S. Wang, F.E. Soetaredjo, S. Ismadji, Preparation of capacitor's electrode from cassava peel waste, *Bioresour. Technol.* 101 (2010) 3534-3540.
- [26] J. Chen, J. Qiu, B. Wang, H. Feng, Y. Yu, E. Sakai, Manganese dioxide/biocarbon composites with superior performance in supercapacitors, *J. Electroanal. Chem.* 791 (2017) 159-166.
- [27] Z. Fei, D. Zhao, T. J. Geldbach, R. Scopelliti, P. J. Dyson, Brønsted acidic ionic liquids and their zwitterions: synthesis, characterization and pKa determination, *Chem. Eur. J.* 10 (2004) 4886-4893.
- [28] D.S. Sutar, N. Padma, D.K. Aswal, S.K. Deshpande, S.K. Gupta, J. V. Yakhmi, Preparation of nanofibrous polyaniline films and their application as ammonia gas sensor, *Sensors Actuators, B Chem.* 128 (2007) 286-292.
- [29] B. Wang, J. Qiu, H. Feng, E. Sakai, T. Komiyama, Nitrogen doped carbon nanowires prepared from polypyrrole nanowires for potential application in supercapacitors, *J. Electroanal. Chem.* 775 (2016) 219-227.
- [30] S. W. Zhang, B. S. Yin, C. Liu, Z. B. Wang, D. M. Gu, Self-assembling hierarchical $NiCo_2O_4/MnO_2$ nanosheets and MoO_3/PPy core-shell heterostructured nanobelts for supercapacitor, *Chem. Eng. J.* 312 (2017) 296-305.
- [31] H. Feng, H. Hu, H. Dong, Y. Xiao, Y. Cai, B. Lei, Y. Liu, M. Zheng, Hierarchical

- structured carbon derived from bagasse wastes: A simple and efficient synthesis route and its improved electrochemical properties for high-performance supercapacitors, *J. Power Sources*. 302 (2016) 164-173.
- [32] B.N.M. Dolah, M. Deraman, M.A.R. Othman, R. Farma, E. Taer, Awitdrus, N.H. Basri, I.A. Talib, R. Omar, N.S.M. Nor, A method to produce binderless supercapacitor electrode monoliths from biomass carbon and carbon nanotubes, *Mater. Res. Bull.* 60 (2014) 10-19.
- [33] X. Zhang, J. Zhu, N. Haldolaarachchige, J. Ryu, D.P. Young, S. Wei, Z. Guo, Synthetic process engineered polyaniline nanostructures with tunable morphology and physical properties, *Polymer*. 53 (2012) 2109-2120.
- [34] D. Zhang, J. Zhao, C. Feng, R. Zhao, Y. Sun, T. Guan, B. Han, N. Tang, J. Wang, K. Li, J. Qiao, J. Zhang, Scalable synthesis of hierarchical macropore-rich activated carbon microspheres assembled by carbon nanoparticles for high rate performance supercapacitors, *J. Power Sources*. 342 (2017) 363-370.
- [35] M. Graglia, J. Pampel, T. Hantke, T.-P. Fellingner, D. Esposito, Nitro Lignin-Derived Nitrogen-Doped Carbon as an Efficient and Sustainable Electrocatalyst for Oxygen Reduction, *ACS Nano*. 10 (2016) 4364-4371.
- [36] Y. Yang, Y. Hao, J. Yuan, L. Niu, F. Xia, In situ preparation of caterpillar-like polyaniline/carbon nanotube hybrids with core shell structure for high performance supercapacitors, *Carbon*. 78 (2014) 279-287.
- [37] M.A. Dar, R.K. Kotnala, V. Verma, J. Shah, W. a. Siddiqui, M. Alam, High Magneto-Crystalline Anisotropic Core-Shell Structured $Mn_{0.5}Zn_{0.5}Fe_2O_4$ /Polyaniline Nanocomposites Prepared by in Situ Emulsion Polymerization, *J. Phys. Chem. C*. 116 (2012) 5277-5287.
- [38] V. Dondur, M. Milojevic, S. Mentus, A. Radulovic, Z. Vukovic, J. Stejskal, G. Ciric-Marjanovic, Synthesis and characterization of conducting self-assembled polyaniline nanotubes/zeolite nanocomposite, *Langmuir*. 25 (2009) 3122-3131.
- [39] M. Zhou, F. Pu, Z. Wang, S. Guan, Nitrogen-doped porous carbons through KOH activation with superior performance in supercapacitors, *Carbon*. 68 (2014) 185-194.

- [40] K. Y. Chun, H.S. Lee, C.J. Lee, Nitrogen doping effects on the structure behavior and the field emission performance of double-walled carbon nanotubes, *Carbon*. 47 (2009) 169-177.
- [41] F. Ye, B. Zhao, R. Ran, Z. Shao, A polyaniline-coated mechanochemically synthesized tin oxide/graphene nanocomposite for high-power and high-energy lithium-ion batteries, *J. Power Sources*. 290 (2015) 61-70.
- [42] N. Wang, G. Li, X. Zhang, X. Qi, Chemical synthesis and characterization of dodecylbenzene sulfonic acid-doped polyaniline/viscose fiber, *RSC Adv*. 5 (2015) 44687-44695.
- [43] H. Liu, Y. Zhang, R. Li, X. Sun, S. D é silets, H. Abou-Rachid, M. Jaidann, L.S. Lussier, Structural and morphological control of aligned nitrogen-doped carbon nanotubes, *Carbon*. 48 (2010) 1498-1507.
- [44] P. Yu, Z. Zhang, L. Zheng, F. Teng, L. Hu, X. Fang, A Novel Sustainable Flour Derived Hierarchical Nitrogen-Doped Porous Carbon/Polyaniline Electrode for Advanced Asymmetric Supercapacitors, *Adv. Energy Mater*. 201601111 (2016) 1-10.
- [45] T. Cai, M. Zhou, D. Ren, G. Han, S. Guan, Highly ordered mesoporous phenol-formaldehyde carbon as supercapacitor electrode material, *J. Power Sources*. 231 (2013) 197-202.
- [46] Y. Liu, Y. Ma, S. Guang, H. Xu, X. Su, Facile fabrication of three-dimensional highly ordered structural polyaniline-graphene bulk hybrid materials for high performance supercapacitor electrodes, *J. Mater. Chem. A*. 2 (2014) 813-823.
- [47] C. Hu, S. Chen, Y. Wang, X. Peng, W. Zhang, J. Chen, Excellent electrochemical performances of cabbage-like polyaniline fabricated by template synthesis, *J. Power Sources*. 321 (2016) 94-101.
- [48] Y. Su, I. Zhitomirsky, Asymmetric electrochemical supercapacitor, based on polypyrrole coated carbon nanotube electrodes, *Appl. Energy*. 153 (2015) 48-55.
- [49] B. Wang, J. Qiu, H. Feng, N. Wang, E. Sakai, T. Komiyama, Preparation of MnO₂/carbon nanowires composites for supercapacitors, *Electrochim. Acta*. 212 (2016) 710-721.

- [50] S. Li, C. Zhao, K. Shu, C. Wang, Z. Guo, G.G. Wallace, H. Liu, Mechanically strong high performance layered polypyrrole nano fibre/graphene film for flexible solid state supercapacitor *Carbon*. 79 (2014) 554-562
- [51] X. Zhao, C. Chen, Z. Huang, L. Jin, J. Zhang, Y. Li, L. Zhang, Q. Zhang, Rational design of polyaniline/MnO₂/carbon cloth ternary hybrids as electrodes for supercapacitors, *RSC Adv.* 5 (2015) 66311-66317.
- [52] C. Chang, Z. Hu, T. Lee, Y. Huang, W. Ji, W. Liu, J. Yeh, Y. Wei, Biotemplated hierarchical polyaniline composite electrodes with high performance for flexible, *J. Mater. Chem. A Mater. Energy Sustain.* 4 (2016) 9133-9145.
- [53] J. Liu, L. Zhang, H. Bin Wu, J. Lin, Z. Shen, X.W. (David) Lou, High-performance flexible asymmetric supercapacitors based on a new graphene foam/carbon nanotube hybrid film, *Energy Environ. Sci.* 7 (2014) 3709-3719.
- [54] J. Zhang, J. Jiang, H. Li, X.S. Zhao, A high-performance asymmetric supercapacitor fabricated with graphene-based electrodes, *Energy Environ. Sci.* 4 (2011) 4009-4015.
- [55] W. H. Khoh, J. D. Hong, Solid-state asymmetric supercapacitor based on manganese dioxide/reduced-graphene oxide and polypyrrole/reduced-graphene oxide in a gel electrolyte, *Colloids and Surfaces A: Physicochem. Eng. Aspects* 456 (2014) 26–34.
- [56] N. B. Trung, T. V. Tam, H. R. Kim, S. H. Hur, E. J. Kim, W. M. Choi, *Chemical Engineering Journal* 255 (2014) 89–96.
- [57] J.J. Cai, L. Bin Kong, J. Zhang, Y.C. Luo, L. Kang, A novel polyaniline/mesoporous carbon nano-composite electrode for asymmetric supercapacitor, *Chinese Chem. Lett.* 21 (2010) 1509-1512.
- [58] S. Zhou, H. Zhang, Q. Zhao, X. Wang, J. Li, F. Wang, Graphene-wrapped polyaniline nanofibers as electrode materials for organic supercapacitors, *Carbon*. 52 (2013) 440-450.
- [59] Y. Jin, H. Chen, M. Chen, N. Liu, Q. Li, Graphene-patched CNT/MnO₂ nanocomposite papers for the electrode of high-performance flexible asymmetric supercapacitors, *ACS Appl. Mater. Interfaces.* 5 (2013) 3408-3416.

- [60] Y. J. Peng, T. H. Wu, C. T. Hsu, S. M. Li, M. G. Chen, C. C. Hu, Electrochemical characteristics of the reduced graphene oxide/carbon nanotube/polypyrrole composites for aqueous asymmetric supercapacitors, *Journal of Power Sources* 272 (2014) 970-978.
- [61] X. Cai, S. H. Lim, C. K. Poh, L. Lai, J. Lin, Z. Shen, High-performance asymmetric pseudocapacitor cell based on cobalt hydroxide/graphene and polypyrrole/graphene electrodes, *Journal of Power Sources* 275 (2015) 298-304.

Chapter 6 Fe₃O₄ / biocarbon composites with superior performance in supercapacitors

6.1 Introduction

The global energy crisis and the accompanying environmental pollution has been becoming more and more critical. Therefore, the efficient energy storage conversion equipment and the efficient use of renewable resources have become an urgent requirement [1, 2]. Supercapacitors are novel energy storage devices, which exhibits fast charge/discharge rate and excellent cycle life. Recently, supercapacitors have attracted much more attention due to its superior energy density compared with batteries and other common capacitors [3-6]. Based on the different charge storage mechanisms, supercapacitors can generally be divided into two types: the electrical double-layer capacitors (EDLC) and the pseudocapacitors [7, 8]. In pseudocapacitors, the reversible multielectron redox faradaic reactions makes pseudocapacitors revealing much higher specific capacitance and energy density [9]. Metal oxides and conductive polymer are usually used as pseudocapacitors electrode materials, such as RuO₂, MnO₂, NiO, polyaniline, polypyrrole and PEDOT [10, 11]. In contrast to pseudocapacitors, the energy storing of EDLC arises from the accumulation of ionic charges at the interface between the electrode and the electrolyte. Carbon materials with high specific surface area and good conductivity are usually used in EDLC electrode, but their low energy density limited their further application [12-15].

In recent year, development and application of carbon materials have been becoming a central issue of materialogy [16]. Among multifarious carbon materials, biocarbon has been the most concerned due to its high specific surface area, abundant surface oxygen functional groups, low cost and simple preparation method [17-19]. Many biocarbon derived from biomass including rice husk [20], coconut fiber [21] and

tobacco stems [22] have been prepared. Sugarcane bagasse is a kind of typical biomass waste, and it is sometimes used as animal feed. Besides, it is always discarded and thus leads to many disposal problems. Fortunately, the sugarcane bagasse has abundant hollow and tubular morphology, which can be facilely converted into hierarchical porous biocarbon material via simple pyrolysis and alkali activated [23, 24]. Especially, compared with other biocarbon materials, the sugarcane bagasse derived biocarbon not only has the above advantages, but also presents an allium-giganteum-like microstructure (has been confirmed in our previous work [25]). This particular structure of sugarcane bagasse derived biocarbon is very beneficial to ion transport if this biocarbon is applied to supercapacitors.

As one of transition-metal oxides, magnetite (Fe_3O_4) have two valence states (Fe^{2+} , Fe^{3+}) which make a promise to be applied as supercapacitor material. Furthermore, this material has advantages of low cost and environmentally affinity [26]. However, the intrinsic problem of Fe_3O_4 supercapacitor electrode is lack of electrical conductivity (the specific capacitance of pure Fe_3O_4 is $60\text{-}80 \text{ F g}^{-1}$) [27]. To solve this problem, the common countermeasure is preparation of hybrid nanostructured material by integrating Fe_3O_4 with a carbon host, where the carbon host acts as the conductive network [28, 29]. Until now, many kind of Fe_3O_4 /carbon composites have been prepared. Kim et al. [30] prepared Fe_3O_4 /carbon nanotubes (CNTs) nanocomposites with a high specific capacitance of 165 F g^{-1} . The Fe_3O_4 /reduced graphene oxide [31] and Fe_3O_4 /active carbon [32] were also prepared, and both of them had high surface area/conductivity serve of carbon material.

Hence, in this paper, an efficient method for preparation of Fe_3O_4 /biocarbon composites (KBFe) was developed. The biocarbon (KWB) was obtained by one-step direct pyrolysis of sugarcane bagasse, and then the KBFe composites were obtained by coprecipitation method under different mass ratios of Fe_3O_4 to KWB. As a result, the chemical component and specific surface area of KBFe had a profound effect on the electrochemical performance of KBFe, and the highest specific capacitance of KBFe reached 342 F g^{-1} at a current density of 1 A g^{-1} . In addition, an asymmetric two-electrode system was fabricated by employing KWBM as positive electrode and KBFe-

4 as negative electrode. The asymmetric system also possessed a high energy density and a high cycle stability.

6.2 Experimental

6.2.1 Materials

Sugarcane bagasse was crushed by family-use grinder before use. Ethanol, potassium hydroxide (KOH), hydrochloric acid (HCl), iron dichloride tetrahydrate ($\text{FeCl}_2 \cdot 4\text{H}_2\text{O}$), ferric chloride hexahydrate ($\text{FeCl}_3 \cdot 6\text{H}_2\text{O}$), and sodium hydroxide (NaOH) were purchased from Nacalai Tesque, Inc. (Kyoto, Japan). All the chemicals were analytical grade and used without further purification.

6.2.2 Preparation of KOH-activated biocarbon (KWB) derived from sugarcane bagasse

KWB was obtained by KOH activation method and the typical process as follows [25]: first, sugarcane bagasse was cut into small pieces (opening size approximately 2 mm) and washed with distilled water for 8 h at 90 °C, and then dried at 80 °C for 24 h. Second, 1 g cleanly sugarcane bagasse and 0.6 g KOH were poured into 12 ml absolute ethanol with stirring and heated at 60 °C until all of the ethanol was evaporated, and then dried at 70 °C for 12 h. Third, the remnant mixture was pyrolyzed in a tubular furnace in N_2 atmosphere at 800 °C (heating rate is 10 °C min^{-1}) for 2 h. Finally, the obtained carbon material was washed by 1 M HCl solution and deionized water till the filtrate became neutral and collected after vacuum dry.

6.2.3 Preparation of Fe_3O_4 /KWB composites (KBF_e)

KBF_e composites were prepared via a coprecipitation method. In a typical process, 0.24 g $\text{FeCl}_3 \cdot 6\text{H}_2\text{O}$ and 0.10 g $\text{FeCl}_2 \cdot 4\text{H}_2\text{O}$ (the molar ratio of $\text{Fe}^{3+}/\text{Fe}^{2+}$ is 1.8:1) were dissolved in 100 ml deionized water, and then 0.2 g KWB was added with a vigorous stirring for 10 min. Subsequently, the NaOH solution (1 M) was added drop by drop to

the mixture until the pH value of mixture reached to 11. Then the mixture was heated at 90 °C for 1 h with a vigorous stirring. Finally, the product was removed from the mixture solution by suction and washed several times by deionized water. The black solid product was dried in vacuum at 80 °C for 12 h to obtain the KBF_e-1 composite (the theoretical value of mass ratio of Fe₃O₄ to KWB is 0.25:1). The other products were denoted as KBF_e-2, KBF_e-3, KBF_e-4 and KBF_e-5 for the products prepared with the theoretical value of mass ratio of Fe₃O₄ to KWB is 0.5:1, 0.75:1, 1:1 and 1.5:1, respectively.

6.2.4 Preparation of pure Fe₃O₄

Fe₃O₄ was prepared via a coprecipitation method. In a typical process, 0.24 g FeCl₃ 6H₂O and 0.10 g FeCl₂ 4H₂O (the molar ratio of Fe³⁺/Fe²⁺ is 1.8:1) were dissolved in 100 mL deionized water with a vigorous stirring for 10 min. Subsequently, the NaOH solution (1 M) was added drop by drop to the mixture until the pH value of mixture reached to 11. Then the mixture was heated at 90 °C for 1 h with a vigorous stirring. Finally, the product was removed from the mixture solution by suction and washed several times by deionized water. The black solid product was dried in vacuum at 80 °C for 12 h to obtain the Fe₃O₄.

6.2.5 Preparation of MnO₂/KWB composites (KWBM)

The KWBM composites were prepared by directly reacting KMnO₄ with KWB. In a typical process, 0.2 g KMnO₄ dissolved in 100 ml deionized water, and then 0.1 g KWB (the mass ratio of KMnO₄/KWB is 0.5:1) added the above solution. Subsequently, the mixture was stirred under water bath at 70 °C until the color of solution changed from modena to tawny. The products removed from solution and washed with deionized water for several times, and dried in vacuum at 80 °C for 12 h to obtain of the KWBM composite.

6.2.6 Structure characterization

The morphology and microstructure of samples were observed by scanning electron microscopy (SEM) and transmission electron microscopy (TEM). The SEM was performed by S-4300 instrument (Hitachi, Japan). Transmission electron microscopy (TEM) was carried out on a TF20 field emission electron microscope (FEI, USA). The chemical composition was investigated by energy-dispersive X-ray spectroscopy (EDX). The specific surface areas of samples were determined by Brunauer-Emmett-Teller (BET) method of nitrogen sorption at 77 K using ASAP 2020 analyzer (Micromeritics, USA). The crystallographic structure was carried out via X-ray diffraction (XRD) measurements at XRD-6000 instrument (Shimadzu, Japan) with Cu-K α radiation ($\lambda=0.154$ nm) at a speed of 5° min⁻¹ from 2 θ = 5° to 90°. The surface states of samples were analyzed via X-ray photoelectron spectroscopy (XPS) using a PHI Quantum 5000 instrument (ULVAC-PHI, Japan) equipped with Al K α radiation source.

6.2.7 Electrochemical testing

Conventional three-electrolyte system and asymmetric two-electrode system were used in supercapacitors to measure the electrochemical characterization of KBF_e using Models 1287 electrochemical workstations (Solartron Analytical, UK). The test electrodes were first prepared by mixing the KBF_e or KWBM with carbon black (CB) and PTFE at a mass ratio of 80:15:5, then the mixing were adequately ground to obtain a homogeneous paste for coating onto the Ni foam to forming a current collector. After that, the test electrodes were dried in vacuum at 80 °C for 24 h, then compressed at 10 MPa for 5 min. In three-electrode system, the KBF_e composites test electrodes was used as working electrode, a saturated calomel electrolyte as the reference electrolyte, and a platinum-wire electrodes as counter electrolyte. Cyclic voltammetry (CV) and galvanostatic charge/discharge (GCD) were conducted in a potential window from -1.2 to 0 V for KBF_e composites and -0.3 to 0.4 V for KWBM composite respectively. Electrochemical impedance spectroscopy (EIS) was accomplished at open circuit potential with perturbation of 5 mV in the frequency range from 10⁵ to 10⁻² Hz. For

asymmetric two-electrode system, the system were assembled with KBF₄-4 and KWBM test electrodes as working electrodes. The CV and GCD tests were tested at different voltage windows. A 1M KOH solution was used as an electrolyte for all electrochemical measurements.

The standard calomel reference electrode (SCE) based on GCD curves was evaluated according to the following equation [33] (Eq. 1):

$$C_m = (I \cdot t) / (\Delta V \cdot m) \quad (\text{Eq. 1})$$

where C_m (F g⁻¹) is the specific capacitance (SC), I (A) is discharge current, t (s) is the discharge time, ΔV (V) is the voltage window, and m (g) is the total mass of active material on working electrode in a two-electrode system or three-electrode system.

The energy density (E , Wh kg⁻¹) and power density (P , W kg⁻¹) of the asymmetric supercapacitors were calculated from the discharge curves according to the following equations [34]:

$$E = 1/2 C_m (\Delta V)^2 \quad (\text{Eq. 2})$$

$$P = E/t \quad (\text{Eq. 3})$$

where C_m (F g⁻¹) is SC, t (h) is the discharge time, and ΔV (V) is the potential window from GCD curves of two-electrode system, respectively.

6.3 Results and discussion

6.3.1 Microstructural characterization

As shown in Fig. 6.1, the KWB was obtained by carbonized and activated sugarcane bagasse at one step. It is clearly found that the KWB (SEM image as shown in Fig. 6.2a) presented an allium-giganteum-like structure with high interconnected frameworks which is favorable for the ion diffusion and suitable for preparation of Fe₃O₄-based composites [35]. And then, Fe³⁺ and Fe²⁺ were absorbed on the surface of KWB. Finally, the surface of KWB was uniformly covered by Fe₃O₄ nanoparticles when NaOH solution was dropped slowly into the mixture. The Fe₃O₄ nanoparticles grew on the surface of KWB because of the chemical reaction between Fe³⁺ and Fe²⁺ through

coprecipitation method (Re. 1) [30, 32]:

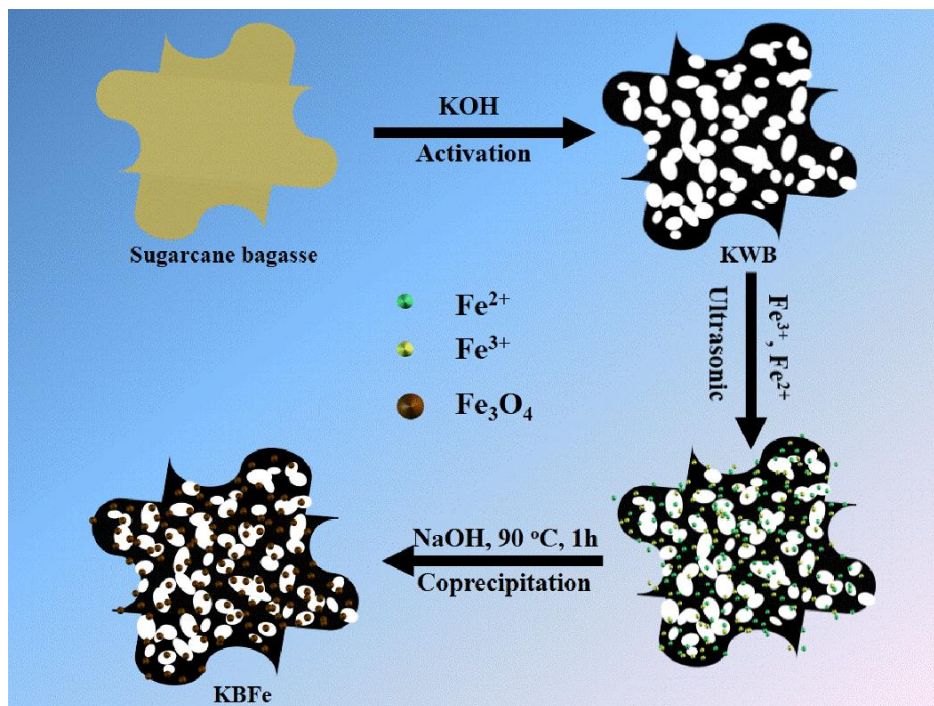


Fig. 6.1 Illustration of preparation procedure of KBFc composites

The morphology of the prepared samples were examined by SEM analysis (Fig. 6.2). An interconnected framework is clearly observed in the KWB (Fig. 6.2a) caused by a lot of secondary pores in the primary pores, which is favorable for the ion diffusion and is suitable for preparation of carbon-based composites. As shown in Fig. 6.2b, Fe₃O₄ nanoparticles exhibit a globular structure forming agglomerates. The surface and interconnected frameworks of KWB in the KBFc composites were coated by Fe₃O₄ nanoparticles. However, it is noteworthy that a little of uncoated KWB was observed in KBFc-1 (Fig. 6.2c and d). The uncoated KWB gradually decreased with the increase in the mass ratio of Fe₃O₄/KWB until the KWB was completely coated by Fe₃O₄ nanoparticles when the mass ratio of Fe₃O₄/KWB is 1 (KBFc-4, Fig. 6.2i and j). In addition, the interconnected structure of KWB was filled by Fe₃O₄ nanoparticles when the mass ratio of Fe₃O₄/KWB was 1.5 (KBFc-5, Fig. 6.2k and l). This phenomenon will affect the ion diffusion and thus the electrochemical performance of KBFc.

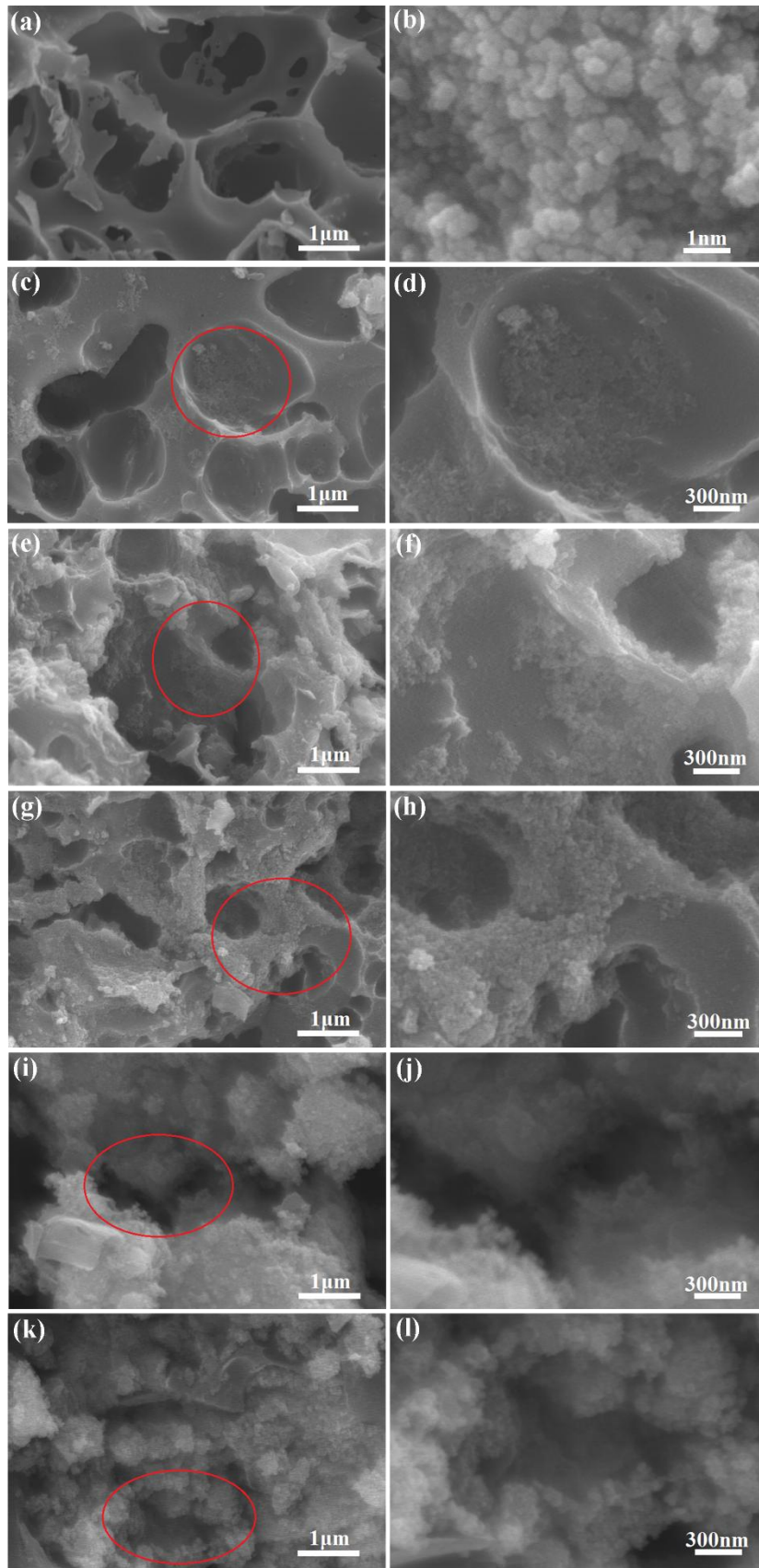


Fig. 6.2 SEM images of KWB (a), Fe₃O₄ (b), KBF_x-1 (c, d), KBF_x-2 (e, f), KBF_x-3 (g, h), KBF_x-4 (i, j) and KBF_x-5 (k, l) composites.

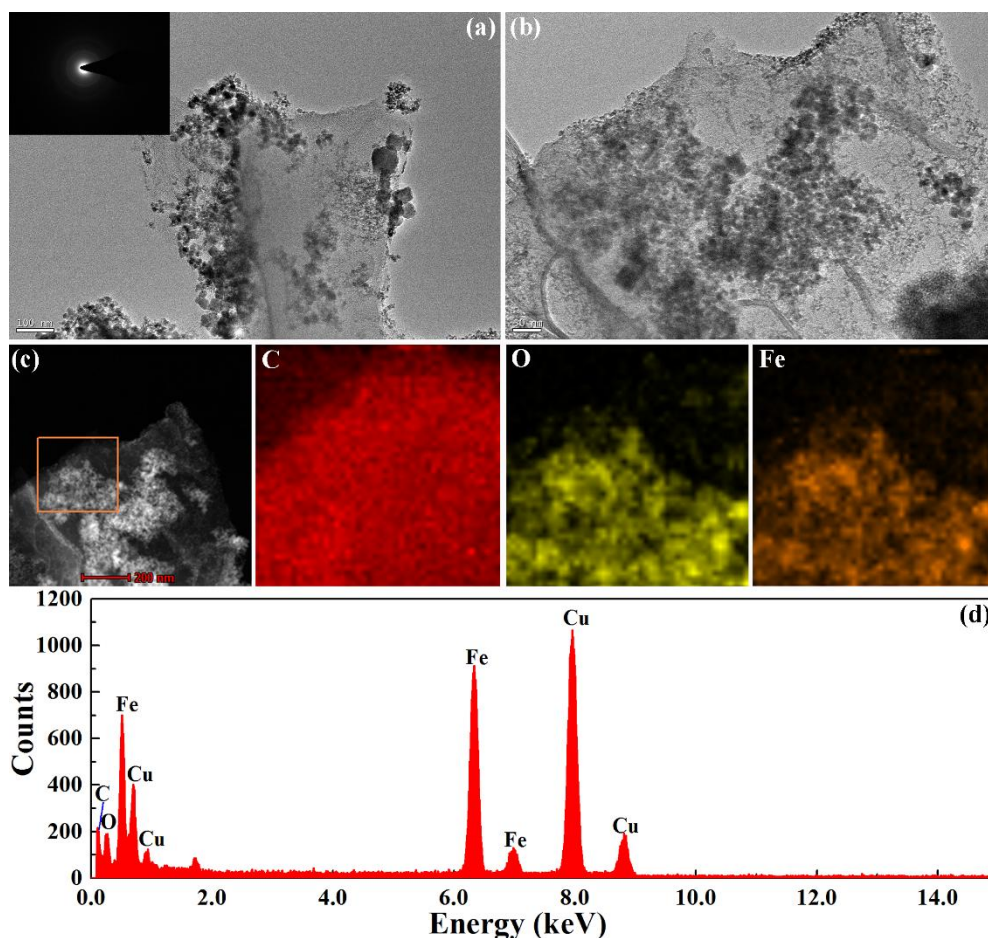


Fig. 6.3 TEM images of the KBFc-4 nanocomposites (a, b); the inset shows the corresponding SAED pattern taken from the edge of Fe_3O_4 nanoparticles; EDX mapping image of C, O and Fe in KBFc-4 (c). EDX spectrum of the KBFc-4 nanocomposites (d).

The morphology of KBFc-4 was further investigated by TEM. As we all know, the diffraction rings of selected area electron diffraction pattern (SAED) correspond to polycrystals, and the diffraction points of SAED correspond to single crystals [36, 37]. For the inset of Fig. 6.3a, it can be clearly observed the diffraction rings, which correspond to the polycrystals of magnetite Fe_3O_4 (The polycrystals of Fe_3O_4 is including $\alpha\text{-Fe}_2\text{O}_3$, $\gamma\text{-Fe}_2\text{O}_3$, FeO and so on [38, 39]). About the magnetite of Fe_3O_4 , it will be further confirmed by XRD. In addition, for Fig. 6.3a, it can be clearly observed that only few Fe_3O_4 was aggregating, however, most Fe_3O_4 nanoparticles were uniformly loaded on the surface of KWB biocarbon with several nanometers size due

to the conductive of carbon better for dispersion of Fe_3O_4 [40]. Furthermore, EDX mapping image reveals the co-existence and homogenous distribution of C, Fe and O across the core-shell nanostructure of KBF_e-4; also, the EDX spectrum of the KBF_e-4 nanoparticles demonstrates the covering effect of Fe_3O_4 for the high content of Fe element.

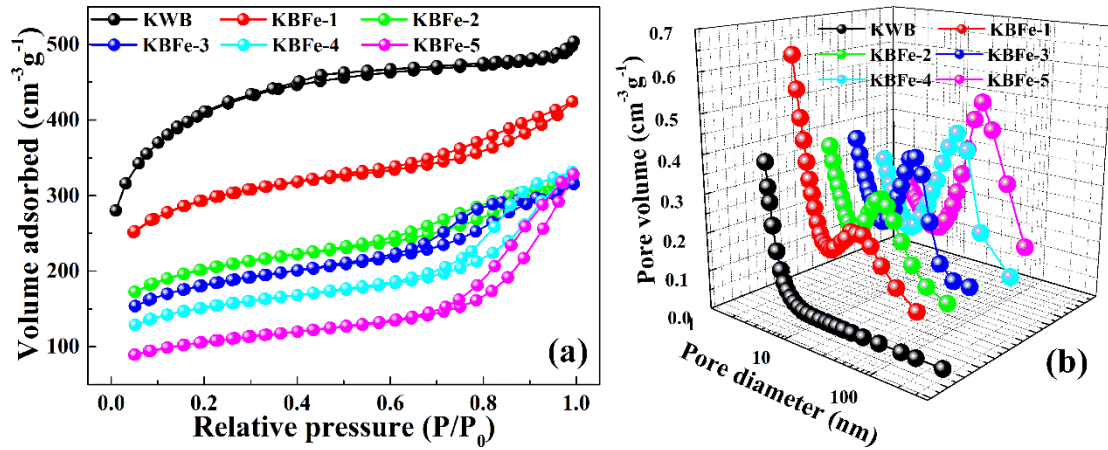


Fig. 6.4 N₂ adsorption-desorption isotherms (a), pore size distribution by BJH method (b) of the prepared KWB biocarbon, KBF_e-1, KBF_e-2, KBF_e-3, KBF_e-4 and KBF_e-5 composites.

Table 6.1 Specific surface area and pore size of samples. (S_{BET} - the specific surface area; P - the main pore size; V_t - the total pore volume)

Sample	V_t (cm ³ g ⁻¹)	S_{BET} (m ² g ⁻¹)	P (nm)
KWB	0.755	1433.06	3.03
KBF _e -1	0.656	936.64	4.19
KBF _e -2	0.502	652.01	4.55
KBF _e -3	0.488	586.51	4.94
KBF _e -4	0.513	490.93	6.83
KBF _e -5	0.508	346.86	9.37

The nitrogen adsorption/desorption isotherm and corresponding pore size distribution of samples were shown in Fig. 6.4a and b. Obviously, the KWB shows the

typically combined I/IV type sorption isotherms, indicating a polyporous structure [41, 42]. As given in Table 6.1, the S_{BET} of KWB is up to $1433.06 \text{ m}^2 \text{ g}^{-1}$, which results in KWB suitable for acting as the scaffolds to combine with the active materials of Fe_3O_4 . For KBFc composites, the Fe_3O_4 nanoparticles were covered on the surface of KWB, which will block the mesopores and micropores of KWB. The S_{BET} , P and V_t of KBFc can be controlled by adjusting the mass ratio of $\text{Fe}_3\text{O}_4/\text{KWB}$. As shown in Table 1, the S_{BET} and V_t of KBFc significantly decreased with the increase of mass ratio of $\text{Fe}_3\text{O}_4/\text{KWB}$. By contrary, the P of KBFc significantly increased when the mass ratio of $\text{Fe}_3\text{O}_4/\text{KWB}$ increased. These results indicate that the micropores and mesopores structure of KWB gradually disappeared. However, the V_t and S_{BET} of the KBFc-4 still increased to $0.513 \text{ cm}^3 \text{ g}^{-1}$ and $490.93 \text{ m}^2 \text{ g}^{-1}$, respectively. These acceptable pore structure and specific surface area of KBFc-4 have a great potential for electrode material in supercapacitors application.

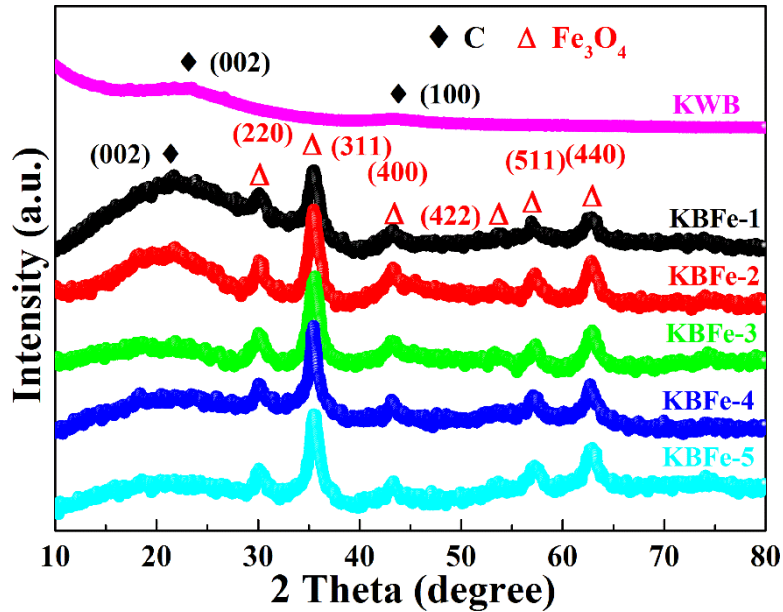


Fig. 6.5 X-ray diffraction patterns of the prepared KWB biocarbon, KBFc-1, KBFc-2, KBFc-3, KBFc-4 and KBFc-5 composites.

The phase and crystallinity of samples were tested by XRD and the results were shown in Fig. 6.5. A broad diffraction peak centered at 23.1° can be attributed to the (002) plane of graphite resulted from its amorphous nature. In addition, a weak

diffraction peak at 43.4° corresponded to the (101) plane of graphite, which is owing to the complete transformation of sugarcane bagasse to a kind of activated carbon [43, 44]. For KBF_e composites, the six diffraction peaks appearing at 30.2°, 35.5°, 43.3°, 53.8°, 57.2° and 62.7° are indexed to the diffraction of (220), (311), (400), (422), (511) and (440) planes of the Fe₃O₄ nanoparticles, respectively (JCPDS no. 19629) [45]. Additionally, the diffraction peak intensity of KWB (peak centered at 23.1°) decreased with the increased mass ratio of Fe₃O₄/KWB. This phenomenon further shows that the surface of KWB is gradually coated by Fe₃O₄ nanoparticles as the mass ratio of Fe₃O₄/KWB increased.

Table 6.2 Chemical compositions of samples.

Samples	C/at. %	O/at. %	Fe/at. %	Fe/C (%)	O-Fe (%)
KWB	84.76	15.24	--	--	--
KWFe-1	67.63	22.67	9.70	14.34	30.81
KWFe-2	63.29	23.79	12.96	20.47	39.32
KWFe-3	55.61	29.61	14.78	26.58	46.39
KWFe-4	42.63	36.01	21.36	50.11	60.00
KWFe-5	42.82	35.77	21.41	50.00	60.15

The surface chemical composition of KWB and KBF_e composites were examined by XPS analysis (Fig. 6.6). The survey spectra of samples are shown in Fig. 6.6a. Except for the signals of C and O elements, there is a signal of Fe element in the XPS spectra of KBF_e when compared with KWB. Table 6.2 indicates that the contents of Fe and O progressively increased with the increase of mass ratio of Fe₃O₄/KWB; however, a reverse situation occurred in the content of C. More information about the change of surface chemistry was further acquired from the deconvoluted high-resolution XPS spectra. The Fe 2p spectra of KBF_e-4 (Fig. 6.6b) presents two main peaks located at 711.4 and 725 eV due to Fe 2p_{3/2} and Fe 2p_{1/2} with a spin-energy separation of 13.6 eV, which confirms that the oxide in the sample is magnetite Fe₃O₄ [46]. The peak of Fe

2p_{3/2} was deconvoluted into two peaks at 710.8 and 712.8 eV, and that of Fe 2p_{1/2} was deconvoluted into two peaks at 724.6 and 726.3 eV. The peaks of 710.8 and 726.3 eV was attributed to the Fe³⁺ of Fe₃O₄, and the others (peak at 712.8 and 724.6 eV) was assigned to the Fe²⁺ of Fe₃O₄ [47, 48].

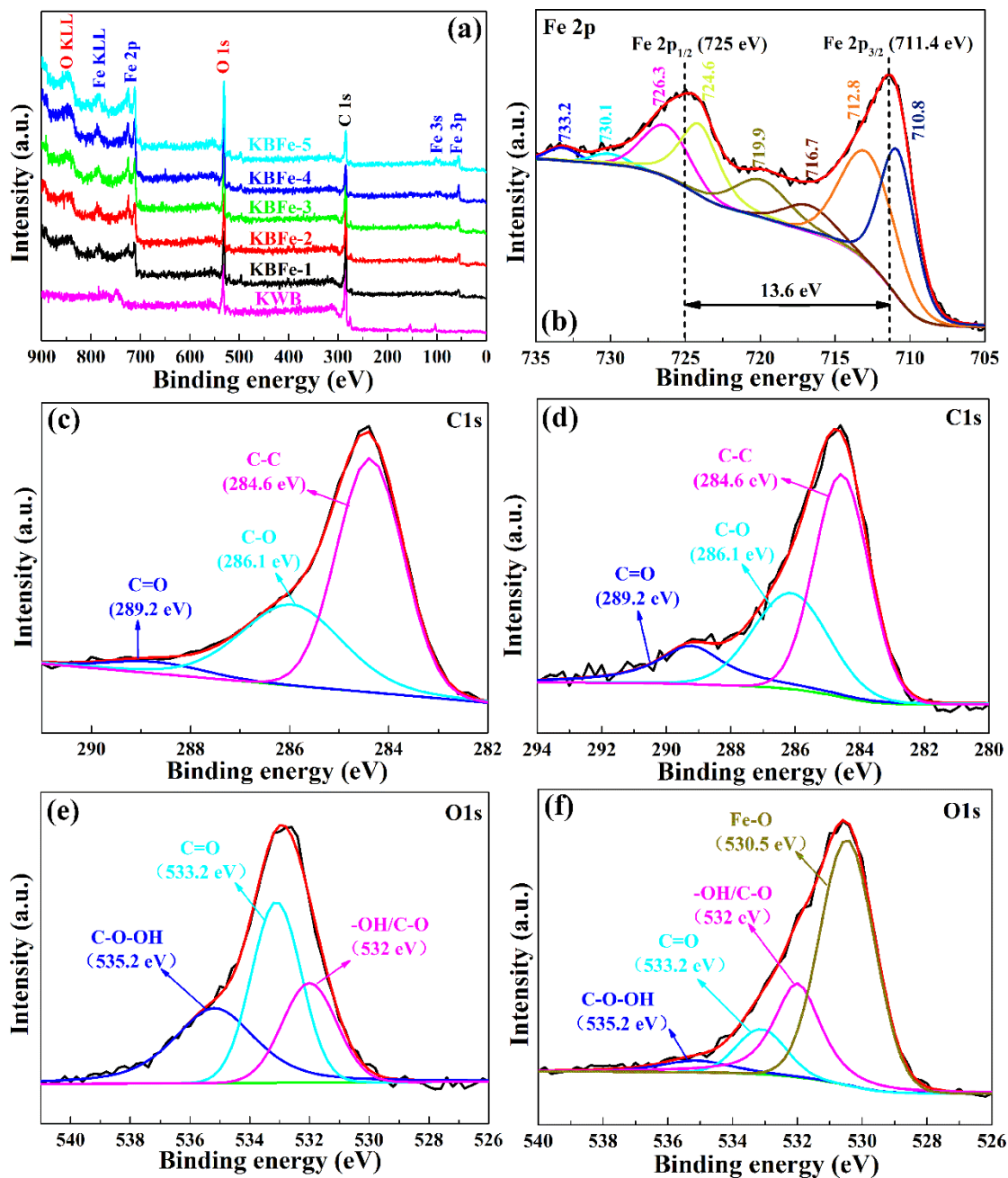


Fig. 6.6 XPS survey spectra of KWB biocarbon, KBFc-1, KBFc-2, KBFc-3, KBFc-4 and KBFc-5 composites (a); high resolution C1s (c) and O1s (e) XPS spectra of KWB and high resolution Fe2p (b), C1s (d) and O1s (f) XPS spectra of KBFc-4 composite.

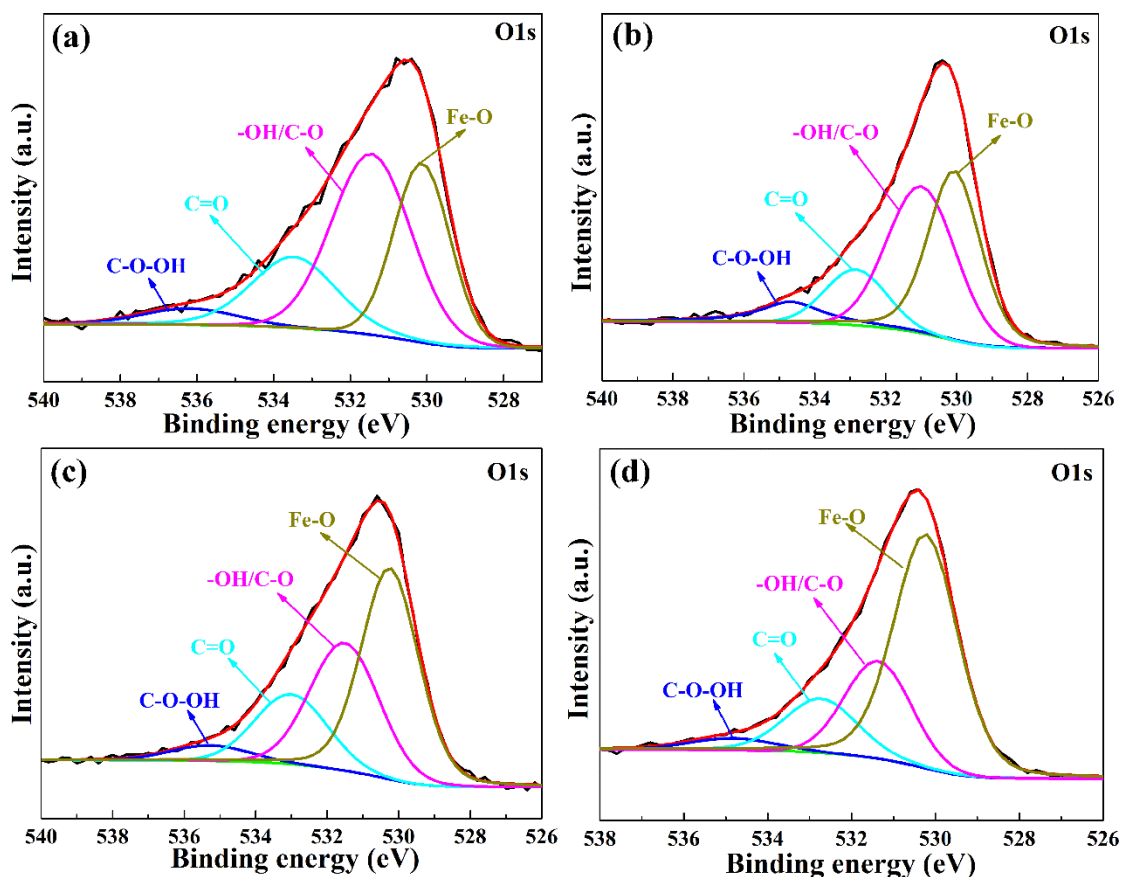


Fig. 6.7. High resolution O1s XPS spectra of KBFc-1 (a), KBFc-2 (b), KBFc-3 (c) and KBFc-5 (d) composites.

The C1s spectra of KWB and KBFc-4 (Fig. 6.6c and e) were deconvoluted into three components. The peaks of 284.4, 285.8 and 288.8 eV were attributed to C–C, C–O, and C=C bonds resulted from the sp^2 -hybridised carbon atoms bonded with neighboring atoms, respectively [49]. The O1s spectrum of KWB were deconvoluted into three peaks (Fig. 6.6e) with binding energies of 531.5, 533.2 and 534.8 eV, which were attributed to -OH/C–O, C=O and C–O–OH groups, respectively [50]. However, for the O1s spectrum of KBFc-4 (Fig.5f), a new peak appeared at 530.5 eV due to the oxygen bonded with iron (O–Fe) in Fe_3O_4 crystal lattice [47]. The content of O–Fe in KBFc (it is obtained by O1s spectra of KBFc-1, 2, 3, 4 and 5, and as shown in Fig. 6.6f and Fig. 6.7) is listed in Table 6.2. The content of O–Fe significantly increased along with the increase of the mass ratio of Fe_3O_4 /KWB from 0.25 to 1), and then reached to constant when the mass ratio of Fe_3O_4 /KWB was higher than 1. These results indicate that the

content of Fe_3O_4 in the KBF_e composites is in a dominant position when the mass ratio of $\text{Fe}_3\text{O}_4/\text{KWB}$ is greater than 1. Additionally, these transformations evidence that the element composition of KBF_e can be adjusted by the mass ratio of $\text{Fe}_3\text{O}_4/\text{KWB}$. In summary, the mass ratio of $\text{Fe}_3\text{O}_4/\text{KWB}$ has a significant impact on the S_{BET} and element composition and hence the electrochemical performance of the KBF_e.

6.3.2 Electrochemical performance of KBF_e composites

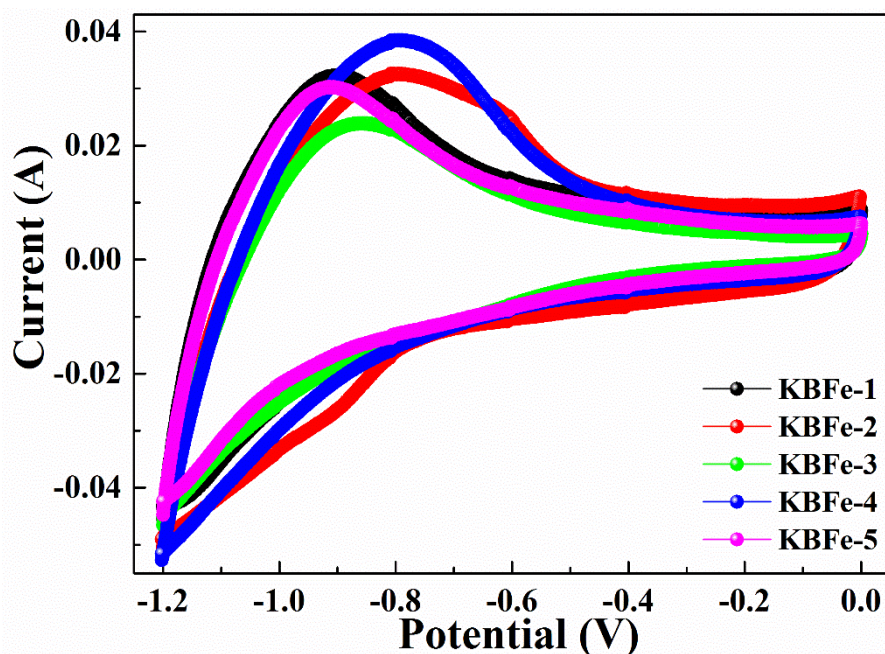
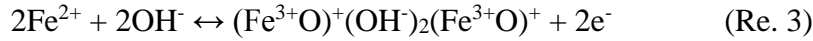
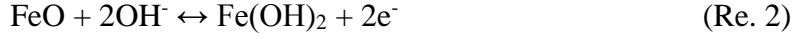


Fig. 6.8 CV curves of KBF_e composites at scan rate of 0.01 V s^{-1} .

To explore potential applications of the KBF_e composites in supercapacitors, the CV, GCD and EIS measurements were performed firstly in a three-electrode configuration. Fig. 6a illustrates the CV curves of the KBF_e at a scan rate of 0.01 V s^{-1} . Compared with CV curve of KWB (as shown in Fig.3.11), all the CV curves of KBF_e show the redox peaks, indicating the existence of pseudocapacitive of Fe_3O_4 . The pseudocapacitance was resulted from the redox reaction of Fe ions, i.e., the oxidation of Fe^{2+} to Fe^{3+} and the reduction of Fe^{3+} back to Fe^{2+} [51]. In addition, the pseudocapacitance reaction of Fe_3O_4 in KOH electrolyte was accompanied by intercalation of OH^- balance the extra charge with the Fe_3O_4 layers, as shown in Re. 2 and 3 [29]:



KBFe-4 exhibited a much larger current response than the other composites, and presented an excellent electrochemical performance thanks to the element composition and acceptable S_{BET} .

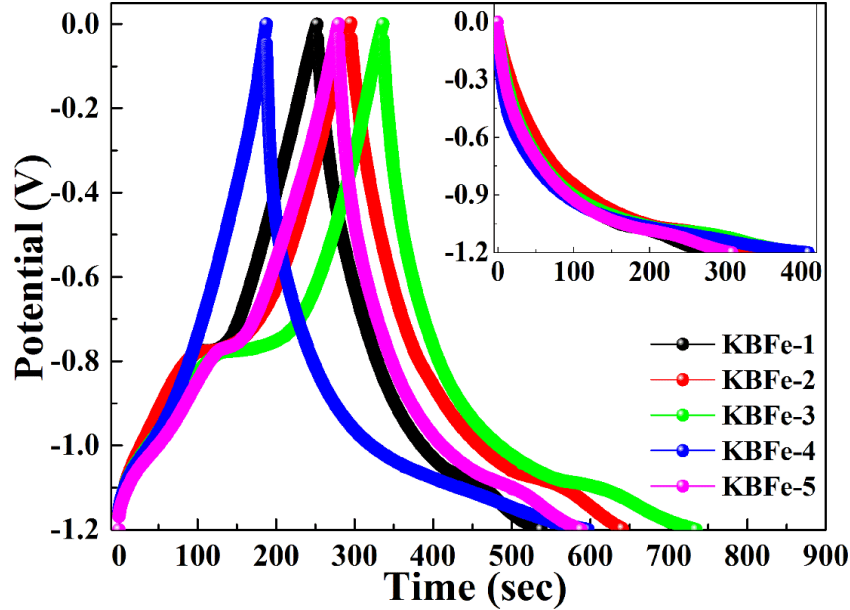


Fig. 6.9 GCD curves of KBFe composites at current density of 1 A g^{-1}

Meanwhile, GCD method was also conducted to compare the capacitive performance of KBFe composites (Fig. 6.9). Overall, all the charge curves of KBFe were nearly symmetrical to their corresponding discharge curves except that the potential is within the range of $-0.8 \sim -1.2 \text{ V}$, indicating that the capacitance is in account of the blend of EDLC and pseudocapacitance corresponding to Re. 2 and 3. Furthermore, the discharge time of KBFe-4 is longer than that of other samples, demonstrating that the KBFe-4 possesses more excellent capacitive performance among all the KBFe composites. According to Eq. 1, the SC of KBFe-1, 2, 3, 4 and 5 were calculated to 237, 288, 332, 342 and 258 F g^{-1} , respectively, at a current density of 1 A g^{-1} . Furthermore, the SC of KBFe increased firstly and then decreased with the mass ratio of the $\text{Fe}_3\text{O}_4/\text{KWB}$ increasing, which are further evidenced by the inference from CV curves.

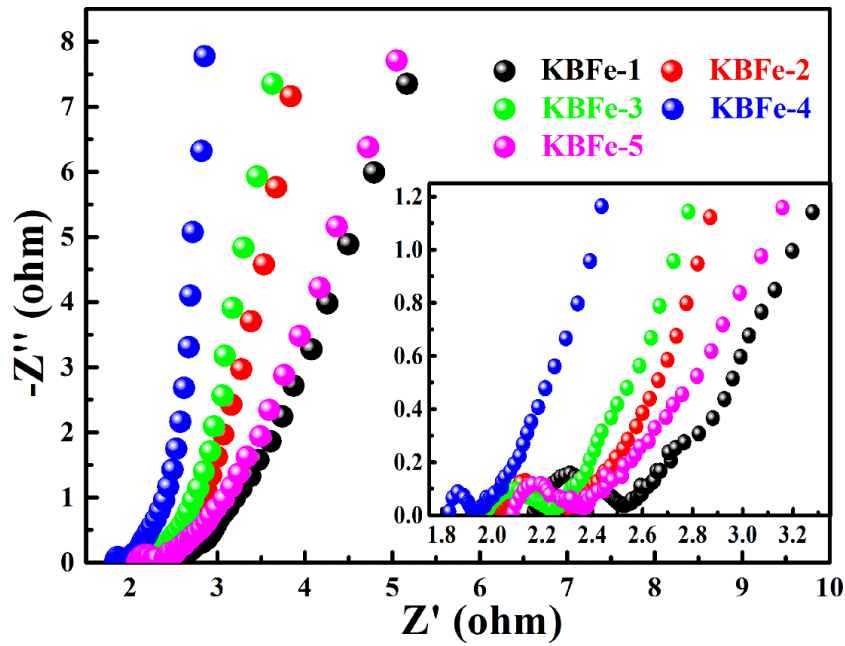


Fig. 6.10 EIS curves of KBFc composites

To further evaluate the capacitive behavior of KBFc, EIS was used to evaluate the ion diffusion and charge transport. The Nyquist plots of KBFc are showed in Fig. 6.10. In general, all the EIS curves consist of three parts: a semicircle in the high frequency region, a nearly diagonal line in the medium frequency region, and a nearly vertical line in the low frequency region, which correspond to the charge-transfer resistance, diffusion resistance between electrolyte and electrode, and capacitive behavior, respectively [26]. The KBFc-4 represents the shortest 45° diagonal line at medium frequency region and the largest slope of straight line at low frequency region, indicating that KBFc-4 possesses the lowest diffusion resistance as well as best capacitive performance among all the samples. From the inset, it is found that KBFc-4 exhibits the least diameter of arc at the high frequency region, which suggests that KBFc-4 has a smaller charge transfer resistance than others. Furthermore, the internal resistance (R_s) of samples can be denoted by the point intersecting of EIS curve with the real axis at high frequency region, including the contact resistance between the active material and current collector, the intrinsic resistance of the active material and the resistance of bulk electrolyte. The inset shows that the R_s of KBFc-1, 2, 3, 4 and 5 are 2.17, 2.04, 1.97, 1.83 and 2.08 Ω , respectively, which demonstrates that the R_s of

KBFe-4 is lower than the other samples. In summary, the results of EIS conclude that KBFe-4 possesses outstanding capacitive performance, which is in line with the CV and GCD measurements.

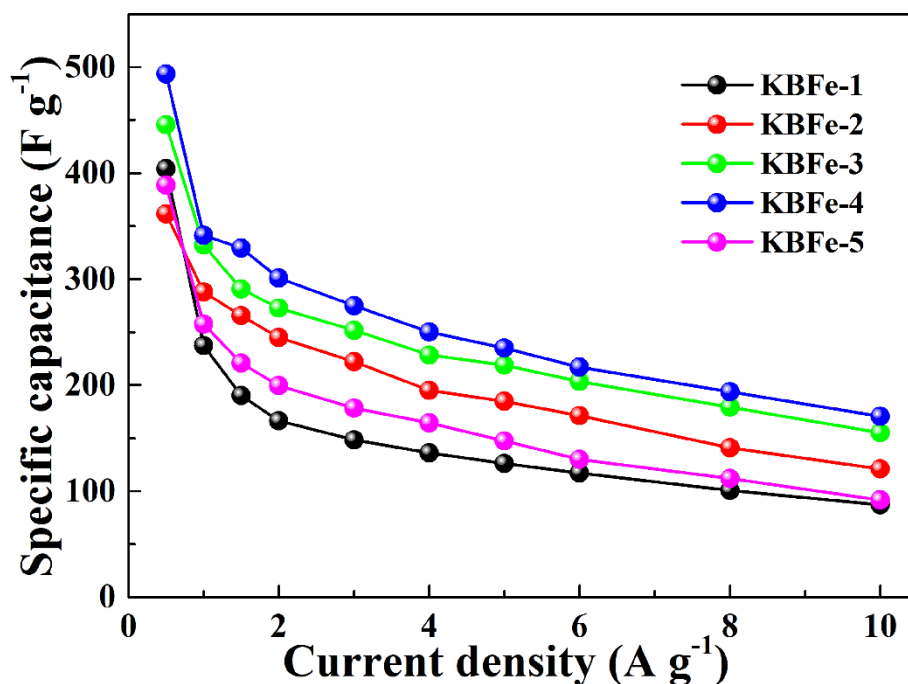


Fig. 6.11 Specific capacitance (SC) versus current density of KBFe composites.

The SC plots of KBFe composites in different current density are shown in Fig. 6.11, indicating that the SC of all samples decreased with the increase of current density. The SC downtrend of KBFe-4 is larger than that of the others, especially when current density increased from 0.5 A g⁻¹ to 1 A g⁻¹ (decreased from 494 F g⁻¹ to 342 F g⁻¹). This is because the S_{BET} of KBFe-4 is smaller than that of the others, and thus the contact area of KBFe-4 and electrolyte is smaller than the others. However, the SC of KBFe-4 could reach to 171 F g⁻¹ at the current density of 10 A g⁻¹, and this value is not only larger than that of the others, but also larger than that of reported previously [52, 53], which suggests that the KBFe-4 has the most excellent fast charge/discharge performance among all the KBFe composites.

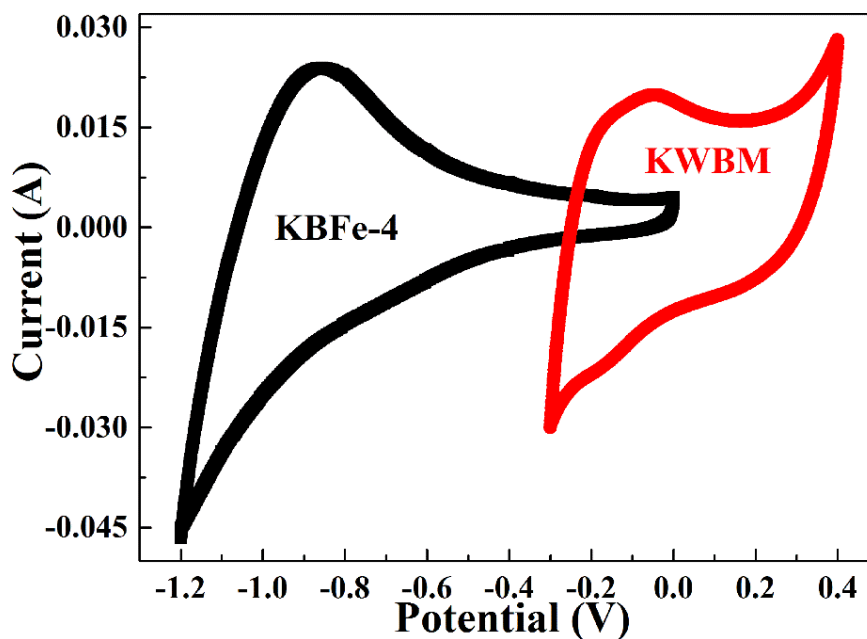


Fig. 6.12 CV curves of KWBM and KBFc-4 in three-electrode asymmetric system at a scan rate of 0.01 V s^{-1}

To further evaluate the capacitive performance of KBFc-4, an asymmetric two-electrode system (KWBM//KBFc-4) was assembled by using the KWBM that was prepared in our previous report as a positive electrode and KBFc-4 as a negative electrode. For confirming the potential window of KWBM//KBFc-4, the CV measurements of KWBM and KBFc-4 were firstly implemented in three-electrode system (Fig. 7a). The KWBM and KBFc-4 electrodes have different potential windows in three-electrode system (their potential windows are -0.3 to 0.4 V and -1.2 to 0 V , respectively). It is expected that the potential window of KWBM//KBFc-4 can be extended up to 1.6 V .

The CV curves of KWBM//KBFc-4 in different potential windows were performed to determine the best potential window (Fig. 6.13a). Obviously, all CV curves were close to a rectangular shape at the potential window up to 1.6 V , revealing that the two-electrode system presents an ideal capacitive behavior. Furthermore, a redox peak appears in CV curve when potential window is $0\text{--}1.6 \text{ V}$, illustrating that the pseudocapacitance and EDLC capacitance simultaneously exist. Fig. 6.13b shows the GCD curves of KWBM//KBFc-4 calculated from GCD at curves density of 1 A g^{-1}

under different voltage windows. The SC of KWBM//KBF_e-4 under different potential windows can be obtained by Eq. 1, where the m is the total mass of active material on two electrodes. The calculated SC increased from 28 to 81.9 F g⁻¹ with the potential window increased from 0.8 to 1.6 V. Hence, the above results suggest that the best potential window of KWBM//KBF_e-4 is 0~1.6 V.

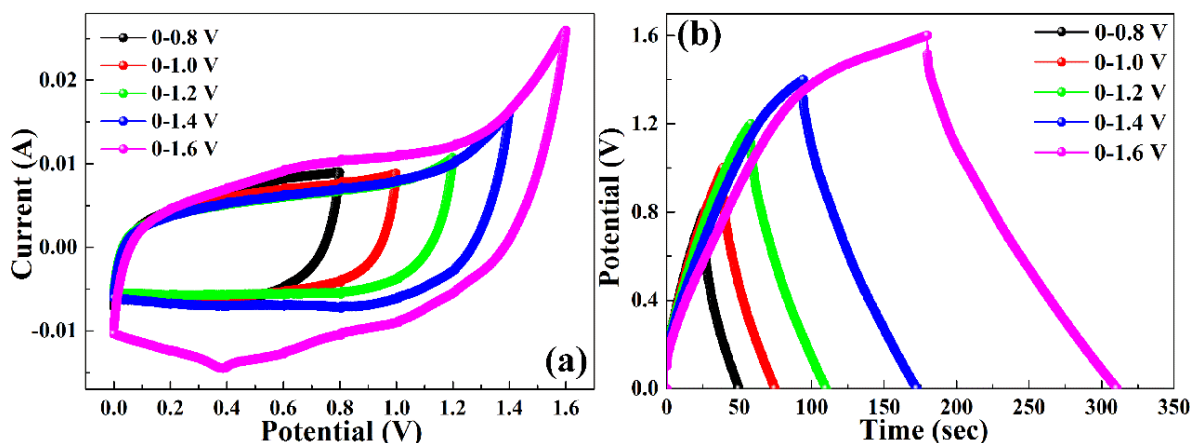


Fig. 6.13 CV curves (a, scan rate of 0.01 V s⁻¹) and GCD curves (b, current density of 1 A g⁻¹) of two-electrode asymmetric system (using KWBM as the positive electrode and KBF_e as the negative electrode) at different potential windows;

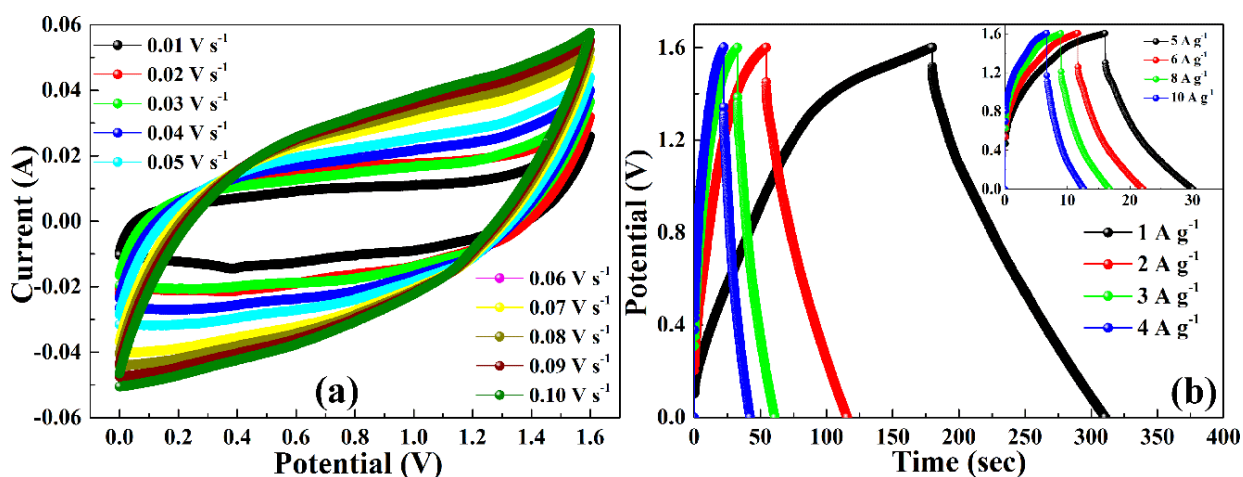


Fig. 6.14 CV (a) and GCD (b) curves of two-electrode asymmetric system (using KWBM as the positive electrode and KBF_e-4 as the negative electrode) at different scan rates and current densities in a potential window of 1.6 V, respectively.

As shown in Fig. 6.14a, the CV curves of KWBM//KBF_e-4 at different scan rates (0.01~0.1 V s⁻¹) were measured between 0~1.6 V. Following the increase of scan rate, the CV curves progressively deviated from the rectangular shape, which suggests that the KWBM//KBF_e-4 gradually deviated from the ideal capacitive behavior as the scan rate increased. GCD measurements were conducted at different current densities to further evaluate the capacitive performance of the KWBM//KBF_e-4 at the voltage window of 0~1.6 V (Fig. 6.14b). These GCD curves were close to triangular shape, indicative of an ideal capacitive behavior. The SC of the KWBM//KBF_e-4 was also obtained from GCD curves based on Eq. 1. The SC was 81.9 F g⁻¹ at a current density of 1 A g⁻¹, and still maintained at 35.6 F g⁻¹ when the current density increased to 10 A g⁻¹, further suggesting that the KWBM//KBF_e-4 has excellent capacitive performance.

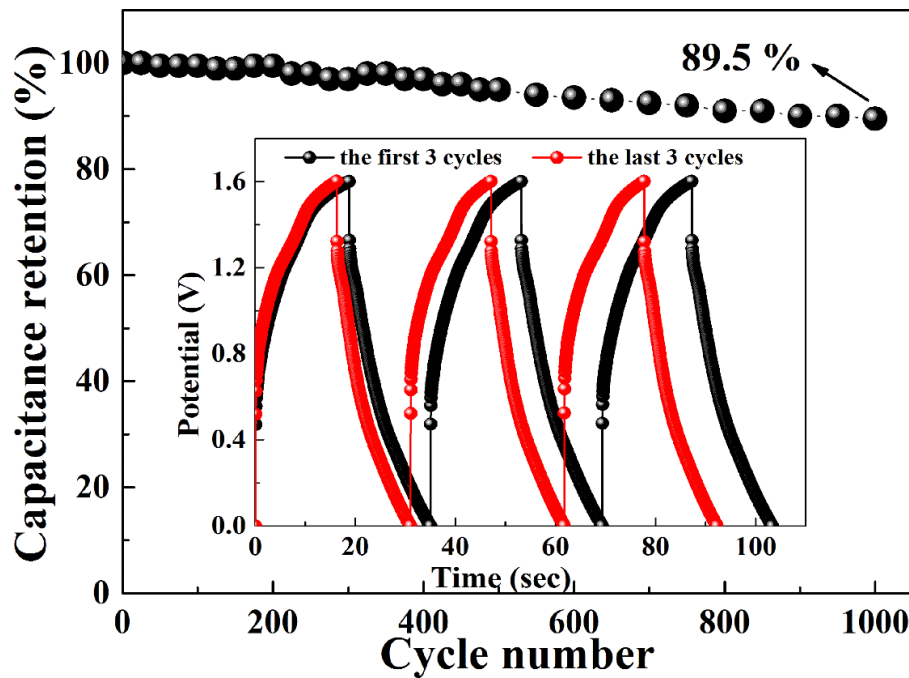


Fig. 6.15 Cycle stability of asymmetric system.

The long-term cycling stability is an indispensable property of supercapacitors. The repeating GCD measures was used to evaluate the cycle stability of KWBM//KBF_e-4 at the current density of 5 A g⁻¹ in 0~1.6 V (Fig. 6.15). The KWBM//KBF_e-4 exhibits an outstanding cycle stability with 89.5% SC retention after 1000 cycles, which is

comparable to those of other Fe₃O₄-based asymmetric two-electrode system, such as Fe₃O₄/Fe-CNTs//AC (82.1% retention after 1000 cycles) [54], Fe₃O₄//AC (82% retention after 500 cycles) [28], and polyaniline-DBSA/Fe₃O₄//polyaniline-DBSA/Fe₃O₄ (65% retention after 1000 cycles) [57].

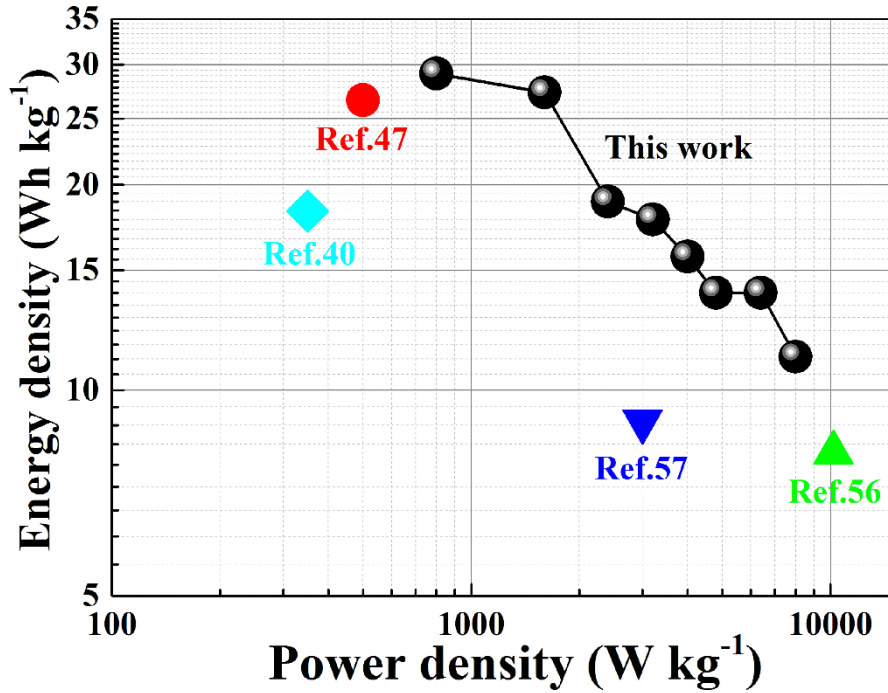


Fig. 6.16 Ragone plot of KWBM//KBFfe-4 asymmetric system

The energy and power density of the KWBM//KBFfe-4 were calculated from the GCD curves according to Eq. 2 and 3, while the results were shown in Fig. 6.15. Basically, the energy density of KWBM//KBFfe-4 gradually decreased with the increase of power density. The maximum energy density is 29.1 Wh kg⁻¹ at a power density of 800 W kg⁻¹. These values are superior to the previous reports, such as Fe₃O₄@Fe₂O₃//Fe₃O₄@MnO₂ (26.6 Wh kg⁻¹, 500 W kg⁻¹) [47], MnO₂//Fe₃O₄ (8.1 Wh kg⁻¹, 10200 kW kg⁻¹) [56], Fe₃O₄/graphene//Fe₃O₄/graphene (9 Wh kg⁻¹, 3000 W kg⁻¹) [57], Fe₃O₄ composite//porous carbon (18.3 Wh kg⁻¹, 351 W kg⁻¹) [40]. These finding suggest the KWBM//KBFfe-4 holds a great promise in the practical application.

6.4 Conclusions

In summary, KBF_e composites were synthesized via a coprecipitation method, where the KWB derived from sugarcane bagasse acted as the scaffolds for Fe₃O₄ deposition and growth. The electrochemical performance of KBF_e was closely related to the mass ratio of Fe₃O₄/KWB. KBF_e-4 showed the best electrochemical performance when the mass ratio of Fe₃O₄/KWB was 1 in three-electrode system. In addition, the assembled asymmetric two-electrode system based on KBF_e-4 and KWBM exhibits high energy density (29.1 Wh kg⁻¹), high power density (800 W kg⁻¹) and an excellent cycling stability of 89.5% SC retention after 1000 cycles. The KBF_e composites synthesized with a facile and low-cost method showed an excellent electrochemical performance, marking them promising candidate in energy storage devices.

References

- [1] R.J. White, V. Budarin, R. Luque, J.H. Clark, D.J. Macquarrie, Tuneable porous carbonaceous materials from renewable resources, *Chem. Soc. Rev.* 38 (2009) 3401–3418.
- [2] A. Hepbasli, A key review on exergetic analysis and assessment of renewable energy resources for a sustainable future, *Renew. Sustain. Energy Rev.* 12 (2008) 593–661.
- [3] A. Walcarius, Mesoporous materials and electrochemistry, *Chem. Soc. Rev.* 42 (2013) 4098-4140.
- [4] N. Choudhary, C. Li, J. Moore, N. Nagaiah, L. Zhai, Y. Jung, J. Thomas, Asymmetric Supercapacitor Electrodes and Devices, *Adv. Mater.* (2017) 1605336.
- [5] G.A. Snook, P. Kao, A.S. Best, Conducting-polymer-based supercapacitor devices and electrodes, *J. Power Sources.* 196 (2011) 1–12.
- [6] P. Simon, Y. Gogotsi, Materials for electrochemical capacitors, *Nat. Mater.* 7 (2008) 845–854.
- [7] F. Vilela, K. Zhang, M. Antonietti, Conjugated porous polymers for energy applications, *Energy Environ. Sci.* 5 (2012) 7819-7832.
- [8] C. Yang, P. Liu, T. Wang, Well-defined core– shell carbon black/polypyrrole nanocomposites for electrochemical energy storage, *ACS Appl. Mater. Interfaces.* (2011) 1109–1114.
- [9] J. Mu, B. Chen, Z. Guo, M. Zhang, Z. Zhang, P. Zhang, C. Shao, Y. Liu, Highly dispersed Fe₃O₄ nanosheets on one-dimensional carbon nanofibers: Synthesis, formation mechanism, and electrochemical performance as supercapacitor electrode materials, *Nanoscale.* 3 (2011) 5034-5040.
- [10] M. Yang, S.B. Hong, B.G. Choi, Hierarchical core/shell structure of MnO₂@polyaniline composites grown on carbon fiber paper for application in pseudocapacitors., *Phys. Chem. Chem. Phys.* 17 (2015) 29874–29879.
- [11] K. Lu, J. Zhang, Y. Wang, J. Ma, B. Song, H. Ma, Interfacial Deposition of Three-Dimensional Nickel Hydroxide Nanosheet-Graphene Aerogel on Ni Wire for

- Flexible Fiber Asymmetric Supercapacitors, *ACS Sustain. Chem. Eng.* (2016) [acssuschemeng.6b02144](https://doi.org/10.1021/acssuschemeng.6b02144).
- [12] A. Ghosh, Y.H. Lee, Carbon-Based Electrochemical Capacitors, *ChemSusChem*. 5 (2012) 480–499.
- [13] M. Enterr á, M.F.R. Pereira, J.I. Martins, J.L. Figueiredo, Hydrothermal functionalization of ordered mesoporous carbons: The effect of boron on supercapacitor performance, *Carbon*. 95 (2015) 72–83.
- [14] D. Gueon, J.H. Moon, Nitrogen-Doped Carbon Nanotube Spherical Particles for Supercapacitor Applications: Emulsion-Assisted Compact Packing and Capacitance Enhancement, *ACS Appl. Mater. Interfaces*. 7 (2015) 20083–20089.
- [15] J. Yang, S. Gunasekaran, Electrochemically reduced graphene oxide sheets for use in high performance supercapacitors, *Carbon N. Y.* 51 (2012) 36–44.
- [16] L.L. Zhang, R. Zhou, X.S. Zhao, Carbon-based materials as supercapacitor electrodes, *J. Mater. Chem.* 38 (2009) 2520–2531.
- [17] C. Wang, Y. Huang, H. Pan, J. Jiang, X. Yang, Z. Xu, H. Tian, S. Han, D. Wu, Nitrogen-Doped Porous Carbon/Graphene Aerogel with Much Enhanced Capacitive Behaviors, *Electrochim. Acta*. 215 (2016) 100–107.
- [18] X. Ma, F. Zhang, J. Zhu, L. Yu, X. Liu, Preparation of highly developed mesoporous activated carbon fiber from liquefied wood using wood charcoal as additive and its adsorption of methylene blue from solution, *Bioresour. Technol.* 164 (2014) 1–6.
- [19] Y. Fan, X. Yang, B. Zhu, P.F. Liu, H.T. Lu, Micro-mesoporous carbon spheres derived from carrageenan as electrode material for supercapacitors, *J. Power Sources*. 268 (2014) 584–590.1
- [20] W. Zhang, N. Lin, D. Liu, J. Xu, J. Sha, J. Yin, X. Tan, H. Yang, H. Lu, H. Lin, Direct carbonization of rice husk to prepare porous carbon for supercapacitor applications, *Energy*. 128 (2017) 618–625.
- [21] L. Yin, Y. Chen, D. Li, X. Zhao, B. Hou, B. Cao, 3-Dimensional hierarchical porous activated carbon derived from coconut fibers with high-rate performance for symmetric supercapacitors, *Mater. Des.* 111 (2016) 44–50.

- [22] P. Kleszyk, P. Ratajczak, P. Skowron, J. Jagiello, Q. Abbas, E. Frąckowiak, F. Béguin, Carbons with narrow pore size distribution prepared by simultaneous carbonization and self-activation of tobacco stems and their application to supercapacitors, *Carbon*. 81 (2015) 148–157.
- [23] N.H. Basri, M. Deraman, S. Kanwal, I.A. Talib, J.G. Manjunatha, A.A. Aziz, R. Farma, Supercapacitors using binderless composite monolith electrodes from carbon nanotubes and pre-carbonized biomass residues, *Biomass and Bioenergy*. 59 (2013) 370–379.
- [24] C.-H. Wang, W.-C. Wen, H.-C. Hsu, B.-Y. Yao, High-capacitance KOH-activated nitrogen-containing porous carbon material from waste coffee grounds in supercapacitor, *Adv. Powder Technol.* (2016) 1–9.
- [25] J. Chen, J. Qiu, B. Wang, H. Feng, Y. Yu, E. Sakai, Manganese dioxide/biocarbon composites with superior performance in supercapacitors, *J. Electroanal. Chem.* 791 (2017) 159–166.
- [26] Q. Wang, L. Jiao, H. Du, Y. Wang, H. Yuan, Fe₃O₄ nanoparticles grown on graphene as advanced electrode materials for supercapacitors, *J. Power Sources*. 245 (2014) 101–106.
- [27] T. Cottineau, M. Toupin, T. Delahaye, T. Brousse, D. Belanger, Nanostructured transition metal oxides for aqueous hybrid electrochemical supercapacitors, *Appl. Phys. A: Mater. Sci. Process.* 82 (2006) 599–606.
- [28] D. Xuan, W. Chengyang, C. Mingming, J. Yang, W. Jin, Electrochemical performances of nanoparticle Fe₃O₄/activated carbon supercapacitor using KOH electrolyte solution, *J. Phys. Chem. C* 113 (2009) 2643–2646.
- [29] J. Pu, L. Shen, S. Zhu, J. Wang, W. Zhang, Z. Wang, Fe₃O₄@C core–shell microspheres: synthesis, characterization, and application as supercapacitor electrodes, *J. Solid State Electrochem.* 18 (2014) 1067–1076.
- [30] Y.H. Kim, S.J. Park, Roles of nanosized Fe₃O₄ on supercapacitive properties of carbon nanotubes, *Curr. Appl. Phys.* 11 (2011) 462–466.
- [31] W. Ullah, A.W. Anwar, A. Majeed, A. Sharif, R. Sharif, P. Khalid, G. Mustafa, A. Khan, Cost-effective and facile development of Fe₃O₄–reduced graphene oxide

- electrodes for supercapacitors, *Mater. Technol.* 30 (2015) 144–149.
- [32] P. He, K. Yang, W. Wang, F. Dong, L. Du, H. Liu, Nanosized Fe₃O₄-modified activated carbon for supercapacitor electrodes, *Russ. J. Electrochem.* 49 (2013) 354–358.
- [33] J. Ruan, Y. Huo, B. Hu, Three-dimensional Ni(OH)₂/Cu₂O/CuO porous cluster grown on nickel foam for high performance supercapacitor, *Electrochim. Acta* 215 (2016) 108–113.
- [34] D. Sarkar, G.G. Khan, A.K. Singh, K. Mandal, High-performance pseudocapacitor electrodes based on α -Fe₂O₃/MnO₂ core–shell nanowire heterostructure arrays, *J. Phys. Chem. C* 117 (2013) 15523–15531.
- [35] H. Feng, H. Hu, H. Dong, Y. Xiao, Y. Cai, B. Lei, Y. Liu, M. Zheng, Hierarchical structured carbon derived from bagasse wastes: A simple and efficient synthesis route and its improved electrochemical properties for high-performance supercapacitors, *J. Power Sources* 302 (2016) 164–173.
- [36] P. Yang, Y. Ding, Z. Lin, Z. Chen, Y. Li, P. Qiang, M. Ebrahimi, W. Mai, C.P. Wong, Z.L. Wang, Low-cost high-performance solid-state asymmetric supercapacitors based on MnO₂ nanowires and Fe₂O₃ nanotubes, *Nano Lett.* 14 (2014) 731–736.
- [37] W. Shi, J. Zhu, D.H. Sim, Y.Y. Tay, Z. Lu, X. Zhang, Y. Sharma, M. Srinivasan, H. Zhang, H.H. Hnga, Q. Yan, Achieving high specific charge capacitances in Fe₃O₄/reduced graphene oxide nanocomposites, *J. Mater. Chem.* 21 (2011) 3422–3427.
- [38] Y. Ding, J.R. Morber, R.L. Snyder, Z.L. Wang, Nanowire Structural Evolution from Fe₃O₄ to ϵ -Fe₂O₃, *Adv. Funct. Mater.* 17 (2007) 1172–1178.
- [39] M. Sarno, E. Ponticorvo, C. Cirillo, High surface area monodispersed Fe₃O₄ nanoparticles alone and on physical exfoliated graphite for improved supercapacitors, *J. Phys. Chem. Solids* 99 (2016) 138–147.
- [40] H. Fan, R. Niu, J. Duan, W. Liu, W. Shen, Fe₃O₄@Carbon Nanosheets for All-Solid-State Supercapacitor Electrodes, *ACS Appl. Mater. Interfaces* 8 (2016) 19475–19483.
- [41] K.S.W. Sing, Reporting physisorption data for gas/solid systems with special

- reference to the determination of surface area and porosity *Pure Appl. Chem.* 57 (1985) 603–619.
- [42] R. Farma, M. Deraman, A. Awitdrus, I.A. Talib, E. Taer, N.H. Basri, J.G. Manjunatha, M.M. Ishak, B.N.M. Dollah, S.A. Hashmi, Preparation of highly porous binderless activated carbon electrodes from fibres of oil palm empty fruit bunches for application in supercapacitors, *Bioresour. Technol.* 132 (2013) 254–261.
- [43] B. Liu, X. Zhou, H. Chen, Y. Liu, H. Li, Promising porous carbons derived from lotus seedpods with outstanding supercapacitance performance, *Electrochim. Acta* 208 (2016) 55–63.
- [44] W. Liu, K. Tian, Y. He, H. Jiang, H. Yu, High-yield harvest of nanofibers/mesoporous carbon composite by pyrolysis of waste biomass and its application for high durability electrochemical energy storage, *Environ. Sci. Technol.* 48 (2014) 13951–13959.
- [45] X.B. Zhang, H.W. Tong, S.M. Liu, G.P. Yong, Y.F. Guan, An improved Stöber method towards uniform and monodisperse $\text{Fe}_3\text{O}_4@C$ nanospheres, *J. Mater. Chem. A* 1 (2013) 7488–7493.
- [46] M. Zong, Y. Huang, Y. Zhao, X. Sun, C.H. Qu, D.D. Luo, J.B. Zheng, Facile preparation, high microwave absorption and microwave absorbing mechanism of RGO– Fe_3O_4 composites, *RSC Adv.* 3 (2013) 23638–23648.
- [47] X. Tang, R. Jia, T. Zhai, H. Xia, Hierarchical $\text{Fe}_3\text{O}_4@ \text{Fe}_2\text{O}_3$ core–shell nanorod arrays as high-performance anodes for asymmetric supercapacitors, *ACS Appl. Mater. Interfaces* 7 (2015) 27518–27525.
- [48] M.C. Biesinger, B.P. Payne, A.P. Grosvenor, L.W.M. Lau, A.R. Gerson, R.S.C. Smart, Resolving surface chemical states in XPS analysis of first row transition metals, oxides and hydroxides: Cr, Mn, Fe, Co and Ni, *Appl. Surf. Sci.* 257 (2011) 2717–2730.
- [49] L. He, Y. Zhang, J.H. Xin, Highly conjugated graphitic 3D carbon frameworks for supercapacitors with long cycling stability, *Carbon* 109 (2016) 650–657.
- [50] Y. Qiao, H. Wang, X. Zhang, P. Jia, T. Shen, X. Hao, Y. Tang, X. Wang, W. Gao,

- L. Kong, *Mater. Lett.* 184 (2016) 252–256.
- [51] A.K. Mishra, S. Ramaprabhu, Ultrahigh volumetric capacitance biomorphic porous carbon material derived from mold, *J. Phys. Chem. C* 115 (2011) 14006–14013.
- [52] Wang Lu, Hongmei Ji, Shasha Wang, Lijuan Kong, Xuefan Jiang, Gang Yang, Preparation of Fe₃O₄ with high specific surface area and improved capacitance as a supercapacitor, *Nanoscale* 5 (2013) 3793–3799.
- [53] Jie Chen, Kelong Huang, Suqin Liu, Hydrothermal preparation of octadecahedron Fe₃O₄ thin film for use in an electrochemical supercapacitor, *Electrochim. Acta* 55 (2009) 1–5.
- [54] J. Sun, P. Zan, X. Yang, L. Ye, L. Zhao, Room-temperature synthesis of Fe₃O₄/Fe-carbon nanocomposites with Fe-carbon double conductive network as supercapacitor, *Electrochim. Acta* 215 (2016) 483–491.
- [55] S. Radhakrishnan, C.R.K. Rao, M. Vijayan, Performance of conducting polyaniline-DBSA and polyaniline-DBSA/Fe₃O₄ composites as electrode materials for aqueous redox supercapacitors, *J. Appl. Polym. Sci.* 122 (2011) 1510–1518.
- [56] T. Cottineau, M. Toupin, T. Delahaye, T. Brousse, D. Bélanger, L. Chantrerie, Nanostructured transition metal oxides for aqueous hybrid electrochemical supercapacitors, *Appl. Phys. A Mater. Sci. Process.* 82 (2006) 599–606.
- [57] K. Karthikeyan, D. Kalpana, S. Amaresh, Y.S. Lee, Microwave synthesis of graphene/magnetite composite electrode material for symmetric supercapacitor with superior rate performance, *RSC Adv.* 2 (2012) 12322–12328.

Chapter 7 Conclusions

Supercapacitors, as one of the most promising energy storage devices, due to their good energy density, superior power density, fast charge/discharge rate, and long cycle life, which make it exhibit promising applications in portable devices, renewable energy and transportation. Based on the different charge storage mechanisms, supercapacitors can generally be divided into two types: the electrical double-layer capacitors (EDLC) and the pseudocapacitors. Carbon materials, such as active carbon, graphene and carbon nanotube are usually used in EDLC electrode, but their low energy density, limited their further application, as well as most of methods to prepare of the above carbon materials often requires complicated preparation conditions or special facilities, leading to the high cost. In the present work, first, low cost and uncomplicated method of allium-giganteum-like biocarbon (KWB) were derived from sugarcane bagasse, and then different kinds of carbon-based composite materials including manganese dioxide (MnO_2)/KWB, polyaniline (PANI)/KWB and iron oxide (Fe_3O_4)/KWB were obtained. All of the above materials were used as electrode material of supercapacitors, and morphology, chemical composition and electrochemical performance were investigated. Besides, due to the unique structure of KWB, all the composites show the superior performance in supercapacitors.

In Chapter 1, the research backgrounds, research significance, research purpose and the construction of this thesis are particularly described.

In Chapter 2, the properties of experimental materials used in this thesis are presented. The experimental methods and characterizations are also particularly described in this chapter.

In chapter 3, KWB were derived from sugarcane bagasse via one-step carbonization and activation method. The results show that, both the mass ratio of potassium hydroxide (KOH) to sugarcane bagasse and the temperature of carbonization could impact on the morphology and chemical composition of KWB, thereby further affect the electrochemical performance of KWB. Under the optimum conditions, the SEM of

KWB shows the excellent 3-D hierarchical porous network structure with allium-giganteum-like, which also has the best specific surface area. Its promise the excellent electrochemical performance when used as electrode materials for supercapacitors. What's more, KWB also could be carbon-base to prepare other composites in the further research.

In chapter 4, MnO_2/KWB (KWBM) composites have been prepared by a simple method. The MnO_2 nanosheets anchored on the surface of biocarbon and obtained the KWBM, and KWB was used as both scaffolds and reducing agents for MnO_2 growth. The analysis results demonstrated that chemical composition and microstructure of KWBM were closely related to the mass ratio of KMnO_4/KWB , and which further impacted electrochemical performance of KWBM profoundly. Especially, the KWBM-4 exhibited a higher specific capacitance of 402 F g^{-1} at a current density of 1 A g^{-1} in three-electrode system. The asymmetric two-electrode system with outstanding energy density was assembled by employing the KWBM-4 as the positive electrode and the KWB as the negative electrode. The two-electrode system displays a high energy density of 25.9 Wh kg^{-1} at a power density of 750 W kg^{-1} within a potential range of 0-1.5 V. Furthermore, the system exhibited high cycle stability with only 5.8 % loss of its initial capacitance after 2000 cycles.

In chapter 5, a coral-like polyaniline/KWB (PANI/KWB) composites was prepared via in-site polymerization method. The PANI/KWB composites were obtained using KWB as the scaffolds for PANI growth and [CMMIm]Cl ionic liquid as dopant. The different mass ratio of aniline monomer (An) and KWB be researched. The results indicated that chemical composition and microstructure of PANI/KWB were closely related to the mass ratio of aniline monomer (An) and KWB, and which further impacted electrochemical performance of PANI/KWB profoundly. Especially, the PANI/KWB-4 exhibited a highest specific capacitance of 447 F g^{-1} at a current density of 0.5 A g^{-1} . Furthermore, the asymmetric two-electrode system based on PANI/KWB-4 as positive electrode and KWB as negative electrode is successfully assembled with a voltage window of 0~1.6 V, exhibiting high energy density (27.3 Wh kg^{-1}) and power density (800 W kg^{-1}), and excellent cycling stability (87% capacitance retention after

2000 cycles).

In chapter 6, Fe₃O₄/KWB nanocomposites (KBF_e) have been prepared via a chemical coprecipitation method under different mass ratio of Fe₃O₄ to KWB. As a result, the chemical composition and microstructure of the KBF_e were intimately related to the mass ratio of Fe₃O₄ and KWB, which impacted the electrochemical performance of the KBF_e profoundly. Especially, the KBF_e-4 displayed the highest specific capacitance of 342 F g⁻¹ at a current density of 1 A g⁻¹. Furthermore, the asymmetric two-electrode system based on KWBM composite as positive electrode and KBF_e-4 as negative electrode was successfully assembled with a voltage window of 0~1.6 V, and exhibited high energy density (29.1 Wh kg⁻¹) and power density (800 W kg⁻¹), along with excellent cycling stability (89.5% capacitance retention after 1000 cycles).

Publication

I. 審査付投稿論文

- [1] **Jiao Chen**, Jianhui Qiu, Bin Wang, Huixia Feng, Yanling Yu, Eiichi Sakai. Manganese dioxide/biocarbon composites with superior performance in supercapacitors. **Journal of Electroanalytical Chemistry**, 791 (2017) 159-166.
- [2] **Jiao Chen**, Jianhui Qiu, Bin Wang, Huixia Feng, Yanling Yu, Eiichi Sakai. Polyaniline/sugarcane bagasse derived biocarbon composites with superior performance in supercapacitors. **Journal of Electroanalytical Chemistry**, 801 (2017) 360-367.
- [3] **Jiao Chen**, Jianhui Qiu, Bin Wang, Bin Wang, Huixia Feng, Kazushi Ito, Eiichi Sakai. Fe₃O₄/biocarbon composites with superior performance in supercapacitors. **Journal of Electroanalytical Chemistry**, 804 (2017) 232–239.
- [4] Huixia Feng, Guo Wang, **Jiao Chen**, Lin Tan, Nali Chen, Jianhui Qiu, Baiyi Chen. Magnetic and electrical properties of polyaniline/CoFe₂O₄ nanocomposites. **Chemical Industry and Engineering Progress**, 34 (2015) 3374-3378.

注：博士論文テーマ関連： 3 編 ((1) ~ (3)), その他： 1 編 (4)

II. 国際会議発表論文

- [1] **Jiao Chen**, Jianhui Qiu, Eiichi Sakai. Hierarchically porous carbon from sugarcane bagasse for high-performance supercapacitors electrode materials. **3rd China International Congress on Composite Materials (CCCM-3)**, Hangzhou, Zhejiang, China, October 20-23, (2017).

注：博士論文テーマ関連： 1 件

III. 国内学会発表

- [1] **陳 姣**、邱 建輝、伊藤 一志、境 英一、冯 輝霞、小宮山 崇夫. 窒素ドーピング炭素電極の創製とスーパーキャパシタへの適用. 2017 年 9 月日本複合材料学会第 39 回複合材料シンポジウム、宮城市.

- [2] 陳 姣、邱 建輝、境 英一、伊藤 一志、王 濱、馮 輝霞、小宮山 崇夫. スーパーキャパシタ適用のためのサトウキビバガスの水酸化カリウム活性化による炭素電極の創製. 2016 年 9 月日本機械学会東北支部第 52 期秋季講演会、秋田市.
- [3] 陳 姣、邱 建輝、境 英一. イオン液体を用いた in situ 重合によるポリピロール / 黒鉛複合材料の作製および性能評価. 2015 年 9 月日本機械学会東北支部第 51 期秋季講演会、いわき市.
- [4] 王 濱、邱 建輝、境 英一、伊藤 一志、陳 姣、馮 輝霞、尾藤 輝夫. カーボンナノファイヤ/二酸化マンガン複合材料の創製およびスーパーキャシタの適用. 2016 年 9 月日本機械学会 東北支部 第 52 期秋季講演会、秋田市.

注: 博士論文テーマ関連: 2 編 ((1) ~ (2)) その他: 2 編 ((3) ~ (4))

Acknowledgements

I would like to thank the following individuals for the support and the help they have provided:

First, Professor Jianhui Qiu, my research advisor for all the support, trust and encouragement throughout the course of my graduate studies. He has been and always be my inspiration scientist and human decency.

And then, my deepest appreciation goes to the professors in Department of Machine Intelligence and Systems Engineering, Faculty of Systems Science and Technology at Akita Prefectural University, Prof. Mamoru Mizuno, Prof. Nobuhiro Kanazawa and Professor in Department of Bioscience and Textile Technology. Faculty of Engineering Science, Akita University, Prof. Mitsutoshi Jikei for the comments and suggestions, whose advices have inestimable value for my research.

Third, Prof. Eiichi Sakai and Prof. Kazushi Ito, I am grateful for his kind help and assistance in my work.

Finally, Professor Huixia Feng, I am grateful for her continuing support and generous access to all electrochemical instruments in her lab.

I also appreciate the technical support from Prof. Takao Komiyama, Prof. Teruo Bitoh, Prof. Ruilu Liang.

In addition, I wish to express my sincere thanks to my friends in Professor Jianhui Qiu group members, Prof. Yanlin Yu, Dr. Bin Wang, Dr. Limin Zang, Dr. Liqiang Gu, Dr. Baiyi Chen, Mr. Longxiang Zhu, Mr. Haodao Mo, Dr. Wendi Liu, Mr. Hongjian Huang, and Ms. Manxi Sun for their valuable discussion on my project.

At last, I would like to express my gratitude to my husband, my mother, my daughter and other relevant for their moral support and warm encouragements.